

ADVANCED CATALYSIS AND NANOSTRUCTURE DESIGN FOR SOLAR ENERGY CONVERSION

GUEST EDITORS: SHAOHUA SHEN, KE SUN, HAIMIN ZHANG, AND YONGQI LIANG





Advanced Catalysis and Nanostructure Design for Solar Energy Conversion

Advances in Condensed Matter Physics

Advanced Catalysis and Nanostructure Design for Solar Energy Conversion

Guest Editors: Shaohua Shen, Ke Sun, Haimin Zhang,
and Yongqi Liang



Copyright © 2014 Hindawi Publishing Corporation. All rights reserved.

This is a special issue published in “Advances in Condensed Matter Physics.” All articles are open access articles distributed under the Creative Commons Attribution License, which permits unrestricted use, distribution, and reproduction in any medium, provided the original work is properly cited.

Editorial Board

Alexandre S. Alexandrov, UK

Dario Alfe, UK

Bohdan Andraka, USA

Daniel Arovas, USA

Veer P. S. Awana, India

Arun Bansil, USA

Ward Beyermann, USA

Golam M. Bhuiyan, Bangladesh

Luis L. Bonilla, Spain

Mark Bowick, USA

Gang Cao, USA

Ashok Chatterjee, India

Ram N. P. Choudhary, India

Kim Chow, Canada

Oleg Derzhko, Ukraine

Gayanath Fernando, USA

Jörg Fink, Germany

Yuri Galperin, Norway

Russell Giannetta, USA

Gabriele F. Giuliani, USA

James L. Gole, USA

Prasenjit Guptasarma, USA

Da-Ren Hang, Taiwan

M. Zahid Hasan, USA

Yurij Holovatch, Ukraine

Chia-Ren Hu, USA

David Huber, USA

Nigel E. Hussey, UK

Philippe Jacquod, USA

Jan A. Jung, Canada

Feo V. Kusmartsev, UK

Rosa Lukaszew, USA

Dmitrii Maslov, USA

Yashowanta N. Mohapatra, India

Abhijit Mookerjee, India

Victor V. Moshchalkov, Belgium

Charles Myles, USA

Vladimir A. Osipov, Russia

Rolfe Petschek, USA

S. J. Poon, USA

Ruslan Prozorov, USA

Leonid Pryadko, USA

Charles Rosenblatt, USA

Mohindar S. Seehra, USA

Sergei Sergeenkov, Brazil

Ivan Smalyukh, USA

Daniel L. Stein, USA

Michael C. Tringides, USA

Sergio E. Ulloa, USA

Attila Virosztek, Hungary

Markus R. Wagner, Germany

Gary Wysin, USA

Gongnan Xie, China

Fajun Zhang, Germany

Contents

Advanced Catalysis and Nanostructure Design for Solar Energy Conversion, Shaohua Shen, Ke Sun, Haimin Zhang, and Yongqi Liang
Volume 2014, Article ID 902729, 3 pages

Effect of Heating Method on Hydrogen Production by Biomass Gasification in Supercritical Water, Qiuhui Yan, Hong Zhang, Bingjie Sun, and Liejin Guo
Volume 2014, Article ID 519389, 5 pages

Hydrogen Production by Supercritical Water Gasification of Biomass with Homogeneous and Heterogeneous Catalyst, Hui Jin, Youjun Lu, Liejin Guo, Ximin Zhang, and Aixia Pei
Volume 2014, Article ID 160565, 9 pages

Revisiting the Zinc-Blende/Wurtzite Heterocrystalline Structure in CdS, Zhaohui Zhou, Mingtao Li, Po Wu, and Liejin Guo
Volume 2014, Article ID 361328, 7 pages

Preparation and Characterization of Novel Fe₂O₃-Flaky Coated Carbon Fiber by Electrospinning and Hydrothermal Methods, Qing-Yun Chen, Lang Liu, and Yun-Hai Wang
Volume 2014, Article ID 938072, 5 pages

Diffusion-Controlled Growth of Oxygen Bubble Evolved from Nanorod-Array TiO₂ Photoelectrode, Xiaowei Hu, Yechun Wang, Liejin Guo, and Zhenshan Cao
Volume 2014, Article ID 970891, 5 pages

Effects of Absorber Emissivity on Thermal Performance of a Solar Cavity Receiver, Jiabin Fang, Nan Tu, and Jinjia Wei
Volume 2014, Article ID 564639, 10 pages

Fabrication of TiO₂ Nanofilm Photoelectrodes on Ti Foil by Ti Ion Implantation and Subsequent Annealing, Yichao Liu, Feng Ren, Guangxu Cai, Mengqing Hong, Wenqing Li, Xiangheng Xiao, Wei Wu, and Changzhong Jiang
Volume 2014, Article ID 254603, 7 pages

Equivalent Circuit Analysis of Photovoltaic-Thermoelectric Hybrid Device with Different TE Module Structure, Haijun Chen, Ning Wang, and Hongcai He
Volume 2014, Article ID 824038, 6 pages

Improved Composite Gel Electrolyte by Layered Vermiculite for Quasi-Solid-State Dye-Sensitized Solar Cells, Hongcai He, Shuangshuang Ren, Deting Kong, and Ning Wang
Volume 2014, Article ID 521493, 5 pages

Photocatalytic Reduction of CO₂ to Methane on Pt/TiO₂ Nanosheet Porous Film, Li Qiu-ye, Zong Lan-lan, Li Chen, Cao Yu-hui, Wang Xiao-dong, and Yang Jian-jun
Volume 2014, Article ID 316589, 6 pages

Preparation and Photocatalytic Activity of Ag Modified Ti-Doped-Bi₂O₃ Photocatalyst, Lilan Zhang, Junfeng Niu, Duo Li, Ding Gao, and Jianghong Shi
Volume 2014, Article ID 749354, 6 pages

Visible-Light-Driven Photocatalytic Degradation of Aniline over NaBiO₃, Guo Liu, Zhen Wang, Wenjie Zheng, Shaogui Yang, and Cheng Sun
Volume 2014, Article ID 961609, 5 pages

Editorial

Advanced Catalysis and Nanostructure Design for Solar Energy Conversion

Shaohua Shen,¹ Ke Sun,² Haimin Zhang,³ and Yongqi Liang⁴

¹ International Research Center for Renewable Energy, State Key Laboratory of Multiphase Flow in Power Engineering, Xi'an Jiaotong University, Xi'an, Shaanxi 710049, China

² Joint Center for Artificial Photosynthesis, California Institute of Technology, Pasadena, CA 91125, USA

³ Centre for Clean Environment and Energy, Environmental Futures Centre, Griffith University, Gold Coast, QLD 4215, Australia

⁴ Department of Chemistry, Umeå University, 901 87 Umeå, Sweden

Correspondence should be addressed to Shaohua Shen; shshen_xjtu@mail.xjtu.edu.cn

Received 29 June 2014; Accepted 29 June 2014; Published 7 July 2014

Copyright © 2014 Shaohua Shen et al. This is an open access article distributed under the Creative Commons Attribution License, which permits unrestricted use, distribution, and reproduction in any medium, provided the original work is properly cited.

Solar energy conversion has been intensively studied in past decades and has been shown to be greatly effective for solving the serious environmental pollution and energy shortage problems. Photoelectrocatalysis and photovoltaics have been considered as the two main approaches for solar energy conversion and utilization, which are generally involved with nanostructured materials and/or catalytic processes, greatly affecting the efficiencies for solar energy conversion. Then, it is necessary to understand the relationship between the physical and chemical properties of nanomaterials and their performances for solar energy conversion. It is also important to explore the fundamentals in catalytic processes for solar energy conversion and make breakthrough in design and synthesis of nanomaterials or nanostructures, characterization of material properties, and performance of novel devices and systems. The aim of this special issue is to present some recent progress in the field of advanced catalysis and nanostructure design for solar energy conversion. A brief summary of all accepted papers is provided below.

The article entitled “*Effect of heating method on hydrogen production by biomass gasification in supercritical water*” investigated the gasification of glucose as a test sample of biomass in supercritical water with different heating methods driven by renewable solar energy. The relations between temperature raising speed of reactant fluid, variation of volume fraction, combustion enthalpy, and chemical energy of H₂ of the product gases and reactant solution concentration

were presented, respectively. The results showed that the energy quality of product gases with preheating process was higher than that with no preheating unit for hydrogen production. Hydrogen production quantity and gasification rate of glucose decreased obviously with the increase of concentration of material in no preheating system.

The article entitled “*Hydrogen production by supercritical water gasification of biomass with homogeneous and heterogeneous catalyst*” selected Ca(OH)₂, Na₂CO₃, K₂CO₃, NaOH, KOH, LiOH, and ZnCl₂ as typical homogeneous catalysts and three kinds of Raney-Ni, dolomite, and olivine as typical heterogeneous catalysts. The catalyst effects were investigated in the process of biomass gasification in supercritical water with the temperature of 400°C, pressure of MPa, and residence time of 20 min. The experimental results showed that Raney-Ni had the best hydrogen selectivity and hydrogen yield and Raney-Ni and NaOH had a synergistic effect in the biomass gasification in supercritical water.

The article entitled “*Revisiting the zinc-blende/wurtzite heterocrystalline structure in CdS*” revisited the band offset at CdS zinc-blende (ZB)/wurtzite (WZ) heterocrystalline interface using the first principles calculations with the local density approximation (LDA), generalized gradient approximation (GGA), and Heyd-Scuseria-Ernzerhof (HSE06) hybrid functional. It was revealed that, unlike most IV, III-V, and II-VI semiconductors, the band alignment at CdS ZB/WZ heterocrystalline interface was of type-I with straddling

lineup of band edges, which was irrespective of the exchange-correlation energy functional, the thickness of ZB and WZ segments, and the ZB/WZ interface location. The partial charge densities of VBM and CBM states were separated around two adjacent interfaces in one unit cell of heterocrystalline superlattice. This type of carrier localization was mainly attributed to the spontaneous polarization occurring in the WZ segment rather than the band offset at the interface.

In the article entitled "*Preparation and characterization of novel Fe₂O₃-flaky coated carbon fiber by electrospinning and hydrothermal methods,*" a novel hierarchical nanostructure of Fe₂O₃-flaky coated carbon fibers was produced by the electrospinning process followed by a hydrothermal technique. First, electrospinning of a colloidal solution that consisted of ferric nitrate and polyacrylonitrile (PAN) was performed to produce PAN nanofibers. Then electrospun nanofiber was stabilized and calcinated in nitrogen at 800°C for 2 h to produce carbon nanofibers (CNFs) which were exploited to produce Fe₂O₃-flaky structure using hydrothermal technique. Fe₂O₃-flaky coated carbon fibers displayed high photocatalytic activity toward degradation of methyl orange (MO) under visible light irradiation.

The article entitled "*Diffusion-controlled growth of oxygen bubble evolved from nanorod-array TiO₂ photoelectrode*" investigated the structure's effects on solid-liquid interface interaction and reaction product transportation on the gas-evolving photoelectrode for photoelectrochemical water splitting. By experimental studies of wettability on the photoelectrode nanorod-array surface and oxygen bubble growth from anode, the interaction affecting the gas-solid-liquid contact behaviors and product transportation mechanism was analyzed, which was controlled by diffusion due to the concentration gradient of dissolved gases in the aqueous electrolyte and the microconvection caused by the bubble interface movement. In the end, based on the bubble growth characteristics of $R_B(t) \sim t^{0.5}$ in the experiment, a model describing the product transport mechanism was presented.

In the article entitled "*Effects of absorber emissivity on thermal performance of a solar cavity receiver,*" the thermal performances of the receiver with different absorber emissivity were numerically simulated. The results showed that the thermal efficiency increases and the total heat loss decreases with increasing emissivity of absorber tubes. However, the thermal efficiency increases by only 1.6% when the emissivity of tubes varies from 0.2 to 0.8. Therefore, the change of absorber emissivity had slight effect on the thermal performance of the receiver. The reason for variation tendency of performance curves was also carefully analyzed. It was found that the temperature reduction of the cavity walls causes the decrease of the radiative heat loss and the convective heat loss.

In the article entitled "*Fabrication of TiO₂ nanofilm photoelectrodes on Ti foil by Ti ion implantation and subsequent annealing,*" the TiO₂ photoelectrodes fabricated on the substrate of Ti foils by Ti ions implantation and subsequent annealing at different temperatures were applied for water splitting. The size of TiO₂ nanoparticles increased with annealing temperatures, and the GIXRD patterns and Raman spectra demonstrated that the phase of TiO₂ turned to rutile

at high temperature. The photoelectrochemical (PEC) and X-ray photoelectron spectroscopy (XPS) spectra of the valence band demonstrated that the samples annealed at 400 and 500°C showed the n-type property. The sample annealed at 600°C showed the weak p-type TiO₂ property. For the sample annealed at 700°C, the negative photocurrent was main, which mainly performed the p-type property of TiO₂. The IPCE values indicated that the absorption edges were red shifted with the increase of annealing temperatures.

In the article entitled "*Equivalent circuit analysis of photovoltaic-thermoelectric hybrid device with different TE module structure,*" the experimental data of dye-sensitized solar cells (DSSCs) and thermoelectric generators (TEG) were simulated by equivalent circuit method, and some parameters of DSSCs were obtained. Then, the equivalent circuit model with the obtained parameters was used to optimize the structure design of photovoltaic- (PV-) thermoelectric (TE) hybrid devices. The output power first increased to a maximum and then decreased by increasing the TE prism size, and a smaller spacing between p-type prism and n-type prism of a TE p-n junction caused a higher output power of TEG and hybrid device. When the spacing between TE prisms was 15 μm and the optimal base side length of TE prism was 40 μm, the maximum theoretical efficiency reached 24.6% according to the equivalent circuit analysis. This work would give some enlightenment for the development of high-performance PV-TE hybrid devices.

In the article entitled "*Improved composite gel electrolyte by layered vermiculite for quasi-solid-state dye-sensitized solar cells,*" a composite quasisolid electrolyte was prepared by adding a layered vermiculite (VMT) into the iodide/triiodide electrolyte including 4-tert-butylpyridine, which obviously improved the photovoltaic properties of quasisolid dye-sensitized solar cells (DSSCs). When adding 6 wt% VMT, the maximum photovoltaic conversion efficiency of 3.89% was obtained, which reached more than two times greater than that without VMT. This enhancement effect was primarily explained by studying the Nyquist spectra, dark currents, and photovoltaic conversion efficiency.

In the article entitled "*Photocatalytic reduction of CO₂ to methane on Pt/TiO₂ nanosheet porous film,*" anatase TiO₂ nanosheet porous films were prepared by calcination of the orthorhombic titanate acid films at 400°C. They showed an excellent photocatalytic activity for CO₂ photoreduction to methane, which should be related to their special porous structure and large Brunauer-Emmett-Teller (BET) surface area. In order to further improve the photocatalytic activity, Pt nanoparticles were loaded uniformly with the average size of 3-4 nm on TiO₂ porous films by the photoreduction method. It was found that the loading of Pt expanded the light absorption ability of the porous film and improved the transformation efficiency of CO₂ to methane. The conversion yield of CO₂ to methane on Pt/TiO₂ film reached 20.51 ppm/h·cm². The Pt/TiO₂ nanosheet porous film was characterized by means of X-ray diffraction (XRD), scanning electron microscopy (SEM), transmission electron microscope (TEM), and ultraviolet-visible light diffuse reflectance spectra (UV-vis DRS). Moreover, the transient

photocurrent-time curves showed that the Pt/TiO₂ nanosheet porous film exhibited higher photocurrent, indicating that the higher separation efficiency of the photogenerated charge carriers was achieved.

In the article entitled “*Preparation and photocatalytic activity of Ag modified Ti-doped-Bi₂O₃ photocatalyst*,” Ti-doped-Bi₂O₃ (TDB) and Ag ion modified Ti-doped-Bi₂O₃ (Ag@TDB) photocatalysts were prepared by framework replacement synthesis method with different Ag loadings (0.05, 0.3, 0.75, and 1.0 mol/L AgNO₃). The structural properties of the prepared catalysts were studied by scanning electron microscope (SEM), X-ray diffraction (XRD), BET surface area, and UV/Vis diffuse reflectance spectra (DRS). The XRD spectra of the Ti-doped-Bi₂O₃ calcined at 650°C showed the diffraction peaks of a mixture of Bi₁₂TiO₂₀ and Bi₄Ti₃O₁₂, with bits of mixed crystallite consisting of TiO₂ and Bi₂O₃. A high blue shift in the range 650–550 nm was detected in the DRS band. This blue shift increased with the decreasing Ag content. The photocatalytic activities of the catalysts were evaluated for the degradation of crystal violet (CV) under UV light irradiation. The results indicated that the degradation rate of CV by using 1.0 mol/L AgNO₃ doped bismuth titanate composite photocatalyst (1.0 Ag@TDB) was 1.9 times higher than that by using the bare Ti-doped-Bi₂O₃ photocatalyst. The higher activity of Ag@TDB was due to the enhancement of electron-hole pair separation by the electron trapping of silver particles.

The article entitled “*Visible-light-driven photocatalytic degradation of aniline over NaBiO₃*” investigated the photocatalytic activity for degradation of aniline over NaBiO₃. It was found that pH and NaBiO₃ dosage had played important role in the photocatalytic degradation. To scrutinize the mechanistic details of the aniline photodegradation, several critical analytical methods including spectroscopy and GC/MS were utilized to detect the temporal course of the reaction. Intermediates and several small molecular products were separated and identified, such as C₂H₅O₃N, C₁₀H₁₃O₂N, and C₁₂H₁₀N₂. Then two possible photodegradation pathways of aniline over NaBiO₃ were proposed: ring opening and mineralization.

Acknowledgments

We would like to express our thanks to all authors who made this special issue possible. We hope that the readers of this issue will find interesting information on advanced catalysis and nanostructure design for solar energy conversion.

Shaohua Shen
Ke Sun
Haimin Zhang
Yongqi Liang

Research Article

Effect of Heating Method on Hydrogen Production by Biomass Gasification in Supercritical Water

Qihui Yan,¹ Hong Zhang,¹ Bingjie Sun,¹ and Liejin Guo²

¹ School of Environmental and Municipal Engineering, Xi'an University of Architecture and Technology, Xi'an 710049, China

² State Key Laboratory of Multiphase Flow in Power Engineering, Xi'an Jiaotong University, Xi'an 710049, China

Correspondence should be addressed to Liejin Guo; lj-guo@mail.xjtu.edu.cn

Received 13 March 2014; Accepted 27 May 2014; Published 17 June 2014

Academic Editor: Yongqi Liang

Copyright © 2014 Qihui Yan et al. This is an open access article distributed under the Creative Commons Attribution License, which permits unrestricted use, distribution, and reproduction in any medium, provided the original work is properly cited.

The glucose as a test sample of biomass is gasified in supercritical water with different heating methods driven by renewable solar energy. The performance comparisons of hydrogen production of glucose gasification are investigated. The relations between temperature raising speed of reactant fluid, variation of volume fraction, combustion enthalpy, and chemical exergy of H₂ of the product gases with reactant solution concentration are presented, respectively. The results show that the energy quality of product gases with preheating process is higher than that with no preheating unit for hydrogen production. Hydrogen production quantity and gasification rate of glucose decrease obviously with the increase of concentration of material in no preheating system.

1. Introduction

With the rapid increase of world energy consumption and serious environmental pollutions caused by the utilization of fossil fuels, sustainable energy systems based on hydrogen as energy carrier coupled with renewable energy resources, such as solar and biomass, are considered as an effective way to resolve issues including greenhouse gas emissions, national energy security, air pollution, and energy efficiency [1]. Solar energy is the world's most abundant and promising energy resource. Compared with conventional energy, solar energy is widely distributed, high security, and so forth.

In addition, solar energy will not be controlled or monopolized by any privileged few. These advantages make the solar energy much better than conventional fossil energy. It is a worldwide issue to make good use of it [2].

The critical point of water is at 647.3 K and 22.1 MPa. The theory of supercritical water gasification is based on a series of unique properties of water near the critical or supercritical thermodynamic state. Because the dielectric constant and the number of hydrogen bonds are lower, and hydrogen bonds' strength is weaker than those of ambient water, supercritical water (SCW) behaves like many organic solvents so that

organic compounds and gases have complete miscibility with SCW. Therefore, SCW can provide homogeneous environment for chemical reaction, which reduces the mass transfer limitations of reaction [3].

We used glucose as a model biomass in this paper because the glucose's composition is single and its aqueous solution is homogeneous; it is easier to achieve high-pressure transport of the material of high concentration. In the process of biomass gasification in supercritical water, the material was mixed with water and transported into the reactor. This paper analyzed the performance of glucose gasification in supercritical water by two different heating methods.

2. Gasification Systems and Heating Methods

Figure 1 shows the process of hydrogen production system without preheating process (Method 1). When the system is running, close the valve of feeding tank and open the valve on the left side of the water tank. To complete a cycle, the water at normal temperature and pressure go through the valve in water tank, and then they are delivered to the high temperature molten salt to boost the temperature and

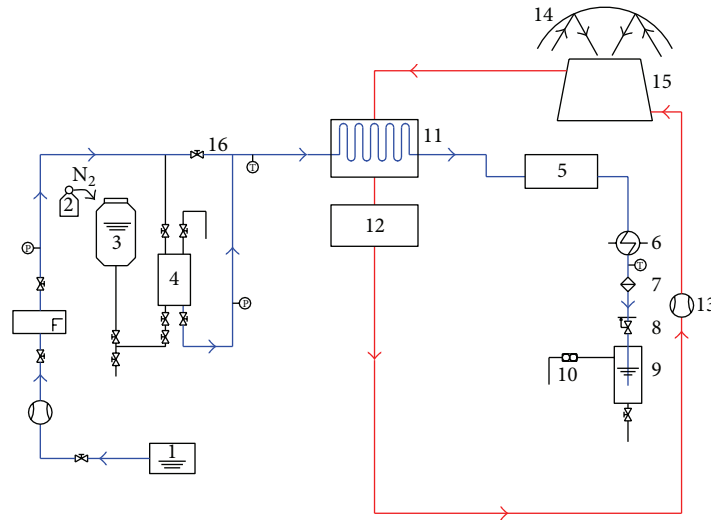


FIGURE 1: Hydrogen production without preheating process (Method 1). (1) water tank, (2) nitrogen tank, (3) storage tank, (4) feeder, (5) regenerator, (6) cooler, (7) filter, (8) back pressure regulator, (9) gas-liquid separator, (10) wet gas flow meter, (11) high temperature molten salt heat tank, (12) low temperature molten salt heat tank, (13) pump for liquid salts, (14) optical block, (15) solar receiver, and (16) valve.

pressure by the high-pressure plunger, after which they go through the regenerator, the cooler, the back pressure valve, and the gas-liquid separator sequentially. After a period of time of operation, reheat each device in the system, then close the valve on the left side of the water tank, open the feeding tank valve, and press the biomass reaction materials (cold fluid, room temperature) into the solar receiver by the piston type charging tank to realize heating gasification reaction.

Figure 2 shows the process of hydrogen production system with preheating process (Method 2).

Among the two figures, the blue line, red line, pink line, and green line represent the molten salt, the preheated water, and the mixture, respectively. The main difference between the two methods is that the fluid in reactor is directly heated by high temperature molten salt heat tank in Method 1, while the fluid in reactor is heated by high temperature molten salt heat tank and hot water from the regenerator in Method 2 simultaneously. In Method 2, water is pumped into the reactor directly and pressurized in the reactor, and the reactor is heated to bring up the system to the setting temperature and pressure. When the temperature and pressure reach the desired values, the feeder is connected to the reactor and preheated pipe is opened simultaneously (no preheated pipe in Method 1). At the exit of the reactor, product flow is rapidly cooled by a cooler. A regulator of back pressure is used to reduce the exit pressure. After leaving the back pressure regulator, the products after reaction pass through a glass gas-liquid separator and are collected and analyzed.

Analysis of the gas product is accomplished by the use of a Hewlett-Packard model 6890 gas chromatograph with thermal conductivity detectors. The carrier is helium, and carrier gas flow rate is 10 mL/min. A Carbon-2000 capillary column is used, operating at 60°C for 2 mins, followed by a 30°C/min ramp to 150°C, hold for 2 mins, then a 20°C/min ramp to 190°C, and a 5 min hold at 190°C.

3. Results

3.1. The Heating Mode of Reactor. It is an endothermic reaction that converts biomass into hydrogen in supercritical water. The reactor should be supplied heat to maintain the normal reaction. According to the heating position, it can be divided into internal heating and external heating. The external heating is usually provided by electric, nuclear, thermal, or other heat sources. The internal heating can be provided by electric, parallel chemical reaction or other methods. The external heating is relatively easy to be implemented. But the temperature of the reactor wall is higher than the temperature of the fluid in the reactor, so as to get the same fluid temperature; it is more strict on the heat-resistant of the reactor, especially in the case of large temperature difference of heat transfer. In addition, for small experimental device, even if the reactor wall is continuously heated, the temperature of the fluid in reactor decreases and is hard to rise because the experiment is endothermic, which makes it difficult to meet the requirements of heat in the reaction. Experiments show that, when the flow of high temperature water is larger, the temperature of fluid at reactor entrance changed a little after the reactants are pressed into the reactor. Otherwise, the temperature of fluid at reactor entrance decreases. These experimental results can be deduced obviously in this paper (Figures 3~4). Figures 3 and 4 show the variation of the temperature of fluid at reactor entrance with time on the condition that the glucose is pressed into the reactor when the preheated high temperature water is 1.0 kg/h and 2.5 kg/h and the flow rate of glucose is 0.5 kg/h [4]. It is shown that, when the heating rate is higher, more H₂ and less macromolecular hydrocarbon are generated [5]. That is to say, the effect of gasification is better. The internal heating provided by electric is between them.

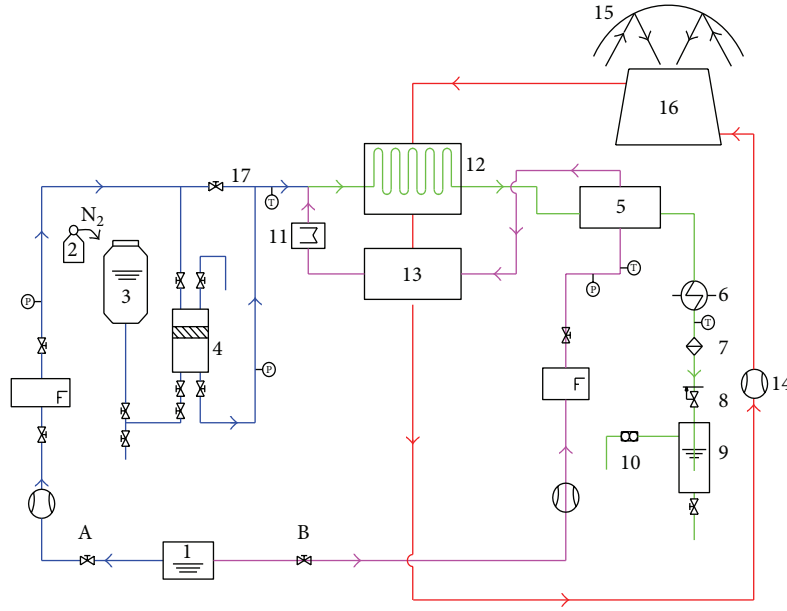


FIGURE 2: Hydrogen production system with preheating process (Method 2). (1) water tank, (2) nitrogen tank, (3) storage tank, (4) feeder, (5) regenerator, (6) cooler, (7) filter, (8) back pressure regulator, (9) gas-liquid separator, (10) wet gas flow meter, (11) electric heater, (12) high temperature molten salt heat tank, (13) low temperature molten salt heat tank, (14) pump for liquid salts, (15) optical block, (16) solar receiver, and (17) valve.

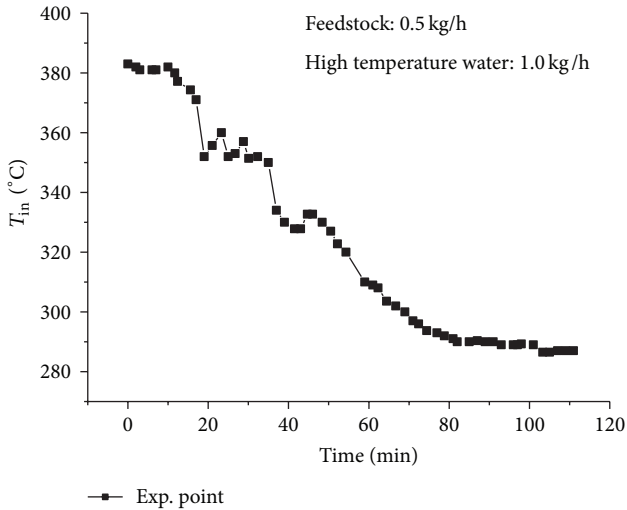


FIGURE 3: The variation of fluid temperature at the reactor inlet with time (small flow high temperature water).

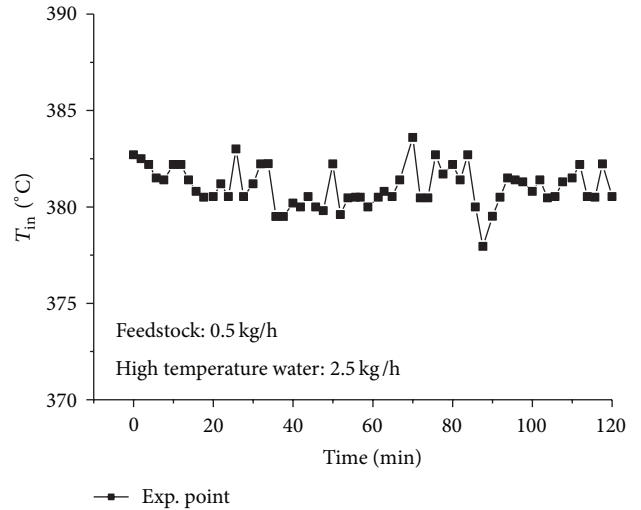
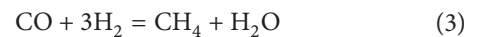
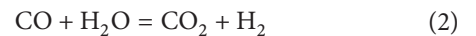
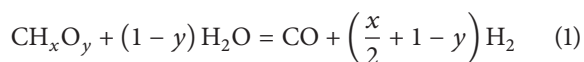


FIGURE 4: The variation of fluid temperature at the reactor inlet with time (large flow high temperature water).

3.2. *Comparison of Gasification Product Components.* For biomass in supercritical water, hydrolysis, pyrolysis, steam reforming, water transformation, and methanation reaction process can occur, generating a large number of intermediates which will introduce other chemical reactions and thus make the overall reaction mechanism more complicated. Biomass gasification in SCW could be summarized into three major reactions:



Tables 1 and 2 show the product gas volume fraction of different concentration of glucose solution gasification in SCW by Method 1 and Method 2 [6]. With the increase of the concentration, the volume fraction of H_2 in Method 1 decreased from 33.90% to 18.94%, almost by half, and it decreased rapidly from 28.50% to 19.62 while the concentration changed from 3.3% to 5%. It decreased because

TABLE 1: The product gas volume fraction of different mass concentration of glucose solution gasification in SCW by Method 1 (600°C; 25 MPa).

Glucose concentration	Product gas volume fraction/%					
	H ₂	CO	CH ₄	CO ₂	C ₂ H ₄	C ₂ H ₆
1.7%	33.90	24.30	2.50	37.90	0.50	0.50
3.3%	28.50	30.60	5.60	34.30	0.50	0.50
5%	19.62	14.23	30.47	35.69	0.50	0.60
10%	18.94	6.02	18.24	56.82	0.70	0.70

TABLE 2: The product gas volume fraction of different mass concentration of glucose solution gasification in SCW by Method 2 (600°C; 25 MPa).

Glucose concentration	Product gas volume fraction/%					
	H ₂	CO	CH ₄	CO ₂	C ₂ H ₄	C ₂ H ₆
1.7%	35.97	26.44	2.20	34.19	0.60	0.60
3.3%	35.66	25.63	2.24	35.25	0.61	0.61
5%	35.67	26.28	2.00	34.88	0.60	0.57
10%	34.21	26.84	2.11	35.53	0.53	0.53

the concentration of the material increase will make the amount of water involved in the reaction (1) become less, which is not conducive for reaction (1) and thus decrease the yield of hydrogen. The volume fraction of H₂ changed a little in Method 2 just from 35.97% to 34.21%, and the volume fraction of H₂ has been almost equal when the concentration increased from 1.7% to 3.5%; volume fraction of CO₂ increased from 37.9% to 56.82% produced by nonpreheating process, which increased about 1.5 times, and the volume fraction of CO and CH₄ increased first and then decreased. The volume fraction of product by preheating process is increased, and the other 4 kinds of gas components are stable. The volume fraction of H₂ by Method 2 is higher than that by Method 1 at all conditions of glucose concentration. This is because Method 2 has the preheating process, which makes the material heating rate become faster. Given that the hydrogen production quantity was in direct proportion to the heating rate [7], the production in Method 2 is higher than that in Method 1.

3.3. Comparison of the Combustion Enthalpy and Chemical Exergy of H₂. Combustion enthalpy and chemical exergy of hydrogen represent the degree of biomass energy conversion to hydrogen energy, namely, utilization to the degree of conversion. It can be seen from Figures 5 and 6 that the hydrogen combustion enthalpy and chemical exergy have obvious differences by different heating way. The hydrogen combustion enthalpy and chemical exergy vary rapidly with the increasing of the concentration. Combustion enthalpy changes in the proportion of span from 47.79% to 14.59%, and the proportion of chemical exergy changes span from 43.89% to 13.03% by Method 1, while the hydrogen combustion enthalpy and chemical exergy fraction produced by Method 2 are very stable, basically reaching 48% and 44%, and material concentration has little effects on hydrogen combustion enthalpy and chemical exergy. Therefore, the energy quality of product gases by Method 2 is higher than

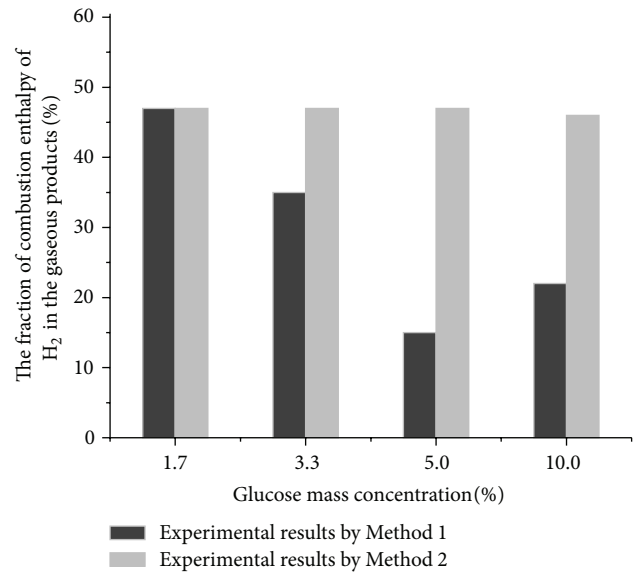


FIGURE 5: The variation of combustion enthalpy fraction of H₂ with the glucose concentration in the gaseous products.

that by Method 1 for objective gas H₂, and the gasification and energy utilization are high and stable.

4. Conclusion

When the preheated high temperature water flow rate is large, the fluid temperature at the reactor inlet changes a little after the reactant is pressed into the reactor. Otherwise, the inlet temperature decreases rapidly. Hydrogen production and energy quality of product gases with preheating process are higher than that with no preheating unit for hydrogen production. The hydrogen combustion enthalpy and chemical exergy vary rapidly with the increase of the reactant

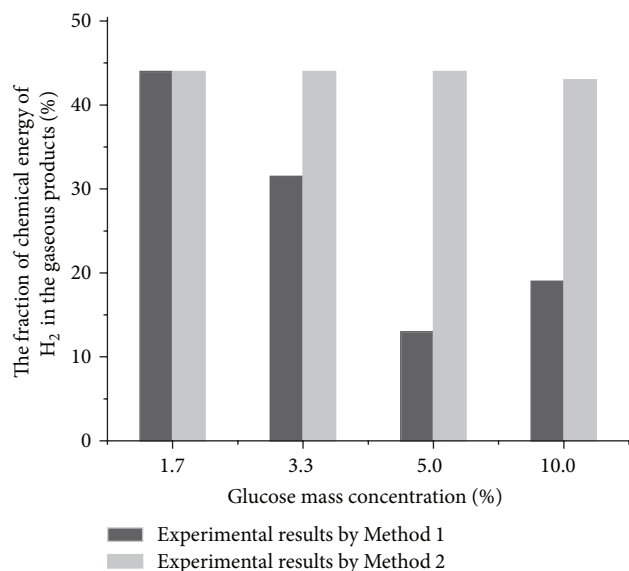


FIGURE 6: The variation of chemical exergy fraction of H_2 with the glucose concentration in the gaseous products.

concentration by Method 1, while the hydrogen combustion enthalpy and chemical exergy vary a little and the reactant concentration has little effects on them by Method 1.

Conflict of Interests

The authors declare that there is no conflict of interests regarding the publication of this paper.

Acknowledgments

This work was financially supported by the National Natural Science Foundation of China (Contract no. 51323011) and the open fund of State Key Laboratory of Multiphase Flow in Power Engineering and Department of Education Project of Shaanxi Province through Contract no. 12JK0788.

References

- [1] R. F. Susanti, J. Kim, and K.-P. Yoo, "Supercritical water gasification for hydrogen production: current status and prospective of high-temperature operation," in *Supercritical Fluid Technology for Energy and Environmental Applications*, pp. 111–137, 2014.
- [2] Y. Lu, L. Guo, X. Zhang, and C. Ji, "Hydrogen production by supercritical water gasification of biomass: Explore the way to maximum hydrogen yield and high carbon gasification efficiency," *International Journal of Hydrogen Energy*, vol. 37, no. 4, pp. 3177–3185, 2012.
- [3] J. Sánchez-Oneto, J. R. Portela, and E. J. Martínez de la Ossa, "Supercritical water oxidation for wastewater destruction with energy recovery," in *Supercritical Fluid Technology for Energy and Environmental Applications*, pp. 181–190, 2014.
- [4] Q. Yan, *Hydrogen Production from Co-Gasification of Biomass and Coal in Supercritical Water*, Xi'an Jiaotong University, Xi'an, Shaanxi China, 2007.
- [5] G. T. Hong and M. H. Spitzer, "Supercritical water partial oxidation," in *Proceedings of the U.S.DOE Hydrogen Program Review, NREL/CP-610-32405*, pp. 1–18, 2002.
- [6] B. Wang, *Optimization of Hydrogen Production from Biomass Gasification in Supercritical Water by Concentrated Solar*, Xi'an University of Architecture and Technology, Xi'an, China, 2012.
- [7] G. T. Hong and M. H. Spitzer, "Supercritical water partial oxidation," in *Proceedings of the U.S.DOE Hydrogen Program Review, NREL/CP-610-32405*, pp. 1–18, 2002.

Research Article

Hydrogen Production by Supercritical Water Gasification of Biomass with Homogeneous and Heterogeneous Catalyst

Hui Jin, Youjun Lu, Liejin Guo, Ximin Zhang, and Aixia Pei

State Key Laboratory of Multiphase Flow in Power Engineering, Xi'an Jiaotong University, Xi'an 710049, China

Correspondence should be addressed to Liejin Guo; lj-guo@mail.xjtu.edu.cn

Received 13 March 2014; Accepted 11 May 2014; Published 16 June 2014

Academic Editor: Shaohua Shen

Copyright © 2014 Hui Jin et al. This is an open access article distributed under the Creative Commons Attribution License, which permits unrestricted use, distribution, and reproduction in any medium, provided the original work is properly cited.

Biomass gasification in supercritical water is a clean and efficient way to convert biomass to hydrogen-rich gaseous products. Appropriate catalyst can lower the reaction temperature to guarantee the technological and economic feasibility. This paper selects $\text{Ca}(\text{OH})_2$, Na_2CO_3 , K_2CO_3 , NaOH , KOH , LiOH , and ZnCl_2 as typical homogeneous catalysts and three kinds of Raney-Ni, dolomite, and olivine as typical heterogeneous catalysts. The catalyst effects are investigated in the process of biomass gasification in supercritical water with the temperature of 400°C , pressure of $22 \sim 24$ MPa, and residence time of 20 min. The experimental results show that Raney-Ni has the best hydrogen selectivity and hydrogen yield. The mixture of NaOH with Raney-Ni was investigated in order to research the synergistic effect of different catalysts. The experimental results show that Raney-Ni and NaOH have a synergistic effect in the biomass gasification in supercritical water.

1. Introduction

Biomass has the potential to provide the increasing energy demand of the world due to the large world-wide resource potential and the optimistic long-term contribution [1]. The clean and efficient utilization of biomass is the object of growing attention due to the environmental and economic reasons [2].

Supercritical water gasification has recently received significant attention as a potential alternative to energy conversion method [3–6]. It has an obvious advantage in converting biomass directly without high energy-consuming drying process to obtain high energy efficiency [7]. Due to the unique physical properties of water above its critical conditions (i.e., 374.15°C and 22.1 MPa), most of hydrogen bonds break [8–10] and offer a controlling mechanism depending on operating parameter and have an excellent transport properties based on their high diffusion ability, low viscosity, and new reaction alternatives for hydrolysis or oxidation [11, 12]. Organic compounds have complete miscibility in supercritical water, and chemical reactions have high efficiency due to the absence of interfacial transport limitations [4, 12]. Air-polluting species containing N and S are not produced because supercritical water gasification

conducts in relatively low temperature [13]. CO_2 can easily be enriched and separated owing to the difference in solubility between CO_2 and other gaseous products [14]. The energy of fluid after reaction can be easily recovered by steam turbine [6].

Catalyst can decrease the reaction temperature and accelerate the reaction to guarantee the technological and economic feasibility of supercritical water gasification and conduct the reaction toward the desired products [15], so catalytic gasification of biomass in supercritical water has received much attention, and the catalyst investigated can roughly be divided into homogenous and heterogenous catalysts [16, 17].

As for homogenous catalyst, it is easy to be mixed with feedstock and is easy to operate for the gasification system. Researchers mainly focus on the alkaline metal catalyst such as KOH [18, 19], NaOH [20–22], K_2CO_3 [23–27], $\text{Ca}(\text{OH})_2$ [28, 29], and KHCO_3 [30]. It is generally accepted that the water-gas shift reaction is accelerated by alkaline metal. Formic acid is assumed to be the intermediate product in the reaction process, and H_2 and CO_2 are produced through the pathway of formic acid decomposition. Alkali can also absorb CO_2 so that water-gas shift reaction can conduct toward the

hydrogen production direction. However, the solubility of inorganic salt in supercritical water is significantly lower than the ambient condition and the eutectic melting of inorganic salt is observed, which may cause trouble in the continuous operation of the gasification system [28].

As for the heterogeneous catalyst, researchers have done extensive job in the screening of the active metal and supporting material to find a catalyst with high activity, hydrothermal stability, and resistance to carbon deposition [31]. Ni-based catalyst is frequently studied due to its relatively low price and high activity. However, hydrothermal instability and carbon deposition are still two big problems for the Ni-based catalyst development [32–34]. Activated carbon gained attention as a potential catalyst for hydrothermal gasification because activated carbon has high activity and does not introduce any pollution to the reaction system. But activated carbon is apt to have deactivation problems [8, 35, 36]. Expensive metal also gained attention due to the extremely high catalytic effects; however, the high price restricts its large-scale industrial application [37–39].

It can be observed that neither homogeneous catalyst nor heterogeneous catalyst is provided with all the advantages. Several typical homogeneous and heterogeneous catalysts are investigated in this paper to study the biomass gasification characteristics of biomass in order that optimal catalyst selection method can be obtained. Minowa and Ogi [40] studied the catalytic effect of mixture of Ni and Na_2CO_3 in a autoclave at the temperature of 350°C and pressure range of 18–20 MPa in the process of thermochemical conversion of cellulose and the synergistic effect was found. This paper will investigate the synergistic effect of homogeneous catalyst and heterogeneous catalyst in supercritical water gasification condition.

2. Experimental Section

2.1. Material. Peanut shell is selected as typical real biomass which is produced in the city of Huanggang, Hubei Province. It is ground until the size of biomass particle is smaller than $180\ \mu\text{m}$. The ultimate analysis and proximate analysis of real biomass can be seen in Table 1. A small quantity of Carboxy methylated cellulose (CMC) is added into the slurry to make a uniform solution. Different types of Raney-Ni are prepared by Dalian general chemical Co., LTD, and the metal element analysis of Raney nickel catalyst (RTH-3110, RTH-4110, RTH-5110) can be seen in Table 2. LiOH, KOH, NaOH, $\text{Ca}(\text{OH})_2$, Na_2CO_3 , and K_2CO_3 are analytic reagent. Olivine and dolomite are provided by the Yingkou Hepingsanhua Mineral Co., Ltd. They are ground until the particle size is smaller, $106\ \mu\text{m}$ and $55\ \mu\text{m}$, respectively.

2.2. Experimental Apparatus and Procedure. Gasification of biomass is carried out in a 140 mL, 316 L stainless steel, high-pressure autoclave. Detailed description of the experimental apparatus was published before [41]. Firstly, 11 g solution of 9.09 wt% glucose and 0.2 g catalyst is added to the reactor for these experiments. The reactor was heated from ambient temperature to the reaction temperature with a heating rate

of about 17 K/min. After gasification reaction, the reactor is cooled down below 473 K in 1 min and then below 373 K in 2.5 min.

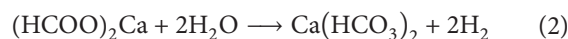
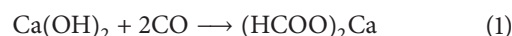
2.3. Analytical Method. The sampled gases were analyzed by a Hewlett-Packard model 6890 gas chromatograph (GC) with a thermal conductivity detector. A Carbon-2000 capillary column was used ($\Phi\ 0.53\ \text{mm} \times 25\ \text{m}$), operating at 333 K for 7 min. N_2 was adopted as the carrier gas with the flow rate of 10 mL/min. A standard gas mixture with 6 kinds of species (H_2 , CO , CO_2 , CH_4 , C_2H_4 , and C_2H_6) is employed for calibration and bought from and compounded by Nanjing Special Gas Co., Ltd. in China.

3. Homogeneous and Heterogeneous Catalyst

3.1. Homogeneous Catalysts. The experimental balance and enhancement of the addition of homogeneous catalyst upon the biomass gasification are seen in Tables 3 and 4, respectively. The yield of hydrogen is 2.86 mmol/g with no catalyst added. The presence of the catalyst increased the yield of hydrogen. KOH has the best catalytic effect and the amplification of hydrogen yield is 144.76%. $\text{Ca}(\text{OH})_2$ takes the second place. The amplification is 132.87%. NaCO_3 has the worst catalytic effect and the amplification is only 9.79%. Meanwhile, the fraction of hydrogen increases at the same time. When $\text{Ca}(\text{OH})_2$ is added, the fraction of hydrogen is 48.54%. The order of catalytic effect on hydrogen yield of biomass gasification is as follows: $\text{KOH} > \text{Ca}(\text{OH})_2 > \text{K}_2\text{CO}_3 > \text{LiOH} > \text{NaOH} > \text{Na}_2\text{CO}_3$. The order of catalytic effect on hydrogen fraction of biomass gasification is as follows: $\text{LiOH} > \text{Ca}(\text{OH})_2 > \text{KOH} > \text{K}_2\text{CO}_3 > \text{NaOH} > \text{Na}_2\text{CO}_3$.

As for the comparison of hydrogen yield between the alkali carbonate and alkali hydroxide, the influence of alkali metal cation (Na^+ , K^+) is far more than that of anion (CO_3^{2-} , OH^-). Comparison between LiOH, NaOH, and KOH shows that the stronger the alkalinity is, the weaker the catalytic effect is for hydrogen production.

It can be seen that when basic catalysts are added, the yield of CO decreases sharply, that is probably due to catalytic effect of basic catalyst upon the water-gas shift reaction. The amount of CO_2 decreases compared with the reaction situation without catalyst because CO_2 is absorbed by the basic catalysts (especially LiOH, NaOH, KOH, and $\text{Ca}(\text{OH})_2$) as carbonates. For example, $\text{Ca}(\text{OH})_2$ is used in HyPr-RING by Lin et al. [28] to absorb CO_2 and to integrate water-gas shift reaction and CO_2 absorption reaction in one reactor. The reactions are as follows:



It can be seen that although the presence of basic catalyst increases the yield of hydrogen and methane, carbon gasification efficiency increases. Basic catalyst has catalytic

TABLE 1: Elemental and proximate analysis of peanut shell.

Biomass	Elemental analysis (wt%)					Proximate analysis (wt%)			
	C	H	N	S	O	M	A	V	FC
Peanut shell	43.80	4.92	1.52	0.17	34.10	7.99	7.50	65.85	18.66

TABLE 2: Metal element analysis of Raney nickel catalyst.

Type	Active metal	Promoter	Al	Particle size/ μm
RTH-3110	~90 wt% Ni	1 wt% Mo	4–10 wt%	50
RTH-4110	~85 wt% Ni	2 wt% Fe, 2.5 wt% Cr	8–12 wt%	50
RTH-5110	~75 wt% Ni	15 wt% Fe	4–10 wt%	32

effect on water-gas shift reaction, and its catalytic effects are reported in earlier publication [18].

On the other hand, basic effect has an important effect in the process of biomass hydrolysis. Sınağ et al. studied the function of K_2CO_3 in the process of glucose gasification in supercritical water. It is found that K_2CO_3 is in favor for the decomposition of glucose to formic acid and restrained furfurals formation. And formic acid is regarded as an intermediate of gas formation. Furfurals can be converted to be phenols and produce tar and coke. Therefore, the presence of K_2CO_3 increases the yield of gas and restrained tar and coke production [26, 42].

Encinar et al. [43] reported that metal chloride such as LiCl, NaCl, KCl, and ZnCl_2 has a catalytic effect in the process of bagasse gasification. ZnCl_2 has an obvious promotion in the process of hydrogen production especially. When ZnCl_2 is used as catalyst, a great amount of char particles are produced, and viscous black tarry substance is produced as well, which is a typical phenomenon of incomplete gasification. Although the carbon gasification efficiency remains constant, the hydrogen selectivity increases sharply and the yield of hydrogen increases by 82.5% because ZnCl_2 has the function of swelling and dissolution and can permeate into the inner place of feedstock so as to form a small opening to increase the contact area of the catalyst and biomass matrix.

3.2. Heterogeneous Catalysts. The experimental balance and enhancement of the addition of heterogeneous catalyst upon the biomass gasification are seen in Tables 5 and 6, respectively. Three kinds of Raney-Ni (RTH-3110, RTH-4110, and RTH-5110) are selected as typical Raney-Ni. They obtained carbon gasification efficiency of 66.73%, 59.66%, and 53.07%, respectively, among which RTH-3110 holds the highest carbon gasification efficiency. The three kinds of Raney-Ni have the hydrogen yield of 9.57, 8.34, and 10.78 mmol/g gas yield compared with 2.86 mmol/g without catalyst.

Raney-Ni is mainly [44, 45] a fine-ground solid composed mostly of nickel derived from a nickel-aluminum alloy, and there are trace elements spread in nickel-aluminum. The lattice defects in the metallic surface and the trace elements increase catalytic effects. The metal analyses for the three catalysts are shown in Table 2. It can be seen from Table 5 that different trace elements have distinct catalytic effects. RTH-5110 doping with Fe has the highest hydrogen yield,

because Fe is in the eighth main group in the periodic table of the elements, and the Ru, Rh, Pd, and Ni have been proved to be an effective catalyst for biomass gasification in supercritical water. Elements in the eighth main group have strong chemical absorption for reactant, so that elements in this main group show catalytic ability in relatively low temperature. Compared with RTH-4110, RTH-3110 has better catalytic effect in hydrogen production. It can be seen that addition of Mo favors hydrogen production from biomass more obviously than Cr. It can provide useful information for home-made catalysts development.

As for the gasification of coal in a pipe flow continuous experimental device operated by Li et al. [23], gasification efficiency, carbon gasification efficiency, and hydrogen gasification efficiency with K_2CO_3 are higher than those with Raney-Ni, because Raney-Ni powder is not well distributed as particles, and K_2CO_3 dissolves in water to form a uniform solution.

It can be seen from Table 6 that olivine and dolomite have a catalytic effect on biomass gasification. They increase hydrogen yield by 46.2% and 37.8%, respectively, compared with the reaction condition without catalyst. Although their catalytic effects are not as high as KOH and $\text{Ca}(\text{OH})_2$, they are still higher than that of Na_2CO_3 and NaOH. The fraction of hydrogen increases with the addition of dolomite and olivine. Complex of CaO-MgO is generated by calcinations and it is a mixed oxide acid-base type catalyst with polar active sites. These active sites can absorb hydrocarbon and break the C–C and C–H bond to obtain gas and liquid product in small molecular in the hydrogen production reaction of biomass gasification in supercritical water. Dolomite also has a catalytic effect on the decomposition of tar and coke with large molecular. Because tar contains a great amount of condensed ring with electronegative π -electron system so they can be absorbed in the π -shaped electron cloud and lose stability and make C–C bond and C–H bond broken easily, so as to lower the activation energy of pyrolysis. Olivine also has good catalytic effect in biomass gasification and is commonly used in traditional biomass gasification process. What is more, olivine has good wear-resisting property and is especially useful in fluidized bed reactor for biomass gasification, which can get rid of the problem of the fragments of the catalyst by friction when catalyst is used as bed material [16, 40, 46–49].

TABLE 3: Mass balance for homogeneous catalyst investigation.

Catalyst	W_R/g	W_G/g	W_L/g	W_S/g	$(W_G + W_L + W_S - W_R)/g$	Mass balance ^a coefficient $Q_m/\%$
Noncatalytic	11.3	0.49	9.94	0.54	0.33	97.09
LiOH	12.3	0.24	10.98	0.71	0.37	96.99
Na ₂ CO ₃	12.3	0.40	10.92	0.71	0.27	97.82
NaOH	12.3	0.34	10.15	0.87	0.94	92.36
K ₂ CO ₃	12.3	0.39	10.06	0.99	0.86	93.04
KOH	12.3	0.36	10.48	0.77	0.69	94.39
Ca(OH) ₂	12.3	0.31	9.32	1.39	1.29	89.52
ZnCl ₂	12.3	0.53	9.91	0.84	1.02	91.74

^aIn the reaction situation with catalyst, all catalyst mass is included in the mass of solid product.

TABLE 4: Experimental results for different homogeneous catalysts.

Catalyst	Gas yield (mmol/g feedstock)				CGE (%)	Gas composition (%)			
	H ₂	CO	CH ₄	CO ₂		H ₂	CO	CH ₄	CO ₂
Noncatalytic	2.86	2.19	1.71	6.48	23.16	21.60	16.54	12.92	48.94
LiOH	5.23	1.30	1.34	2.72	11.96	49.39	12.28	12.65	25.68
Na ₂ CO ₃	3.14	1.43	1.42	5.42	18.46	27.52	12.53	12.45	47.50
NaOH	3.51	0.78	1.63	4.82	16.13	32.68	7.26	15.18	44.88
K ₂ CO ₃	5.64	1.08	2.55	5.09	19.44	39.28	7.52	17.76	35.45
KOH	7.00	0.92	2.98	4.22	18.12	46.30	6.08	19.71	27.91
Ca(OH) ₂	6.66	1.88	1.81	3.37	15.75	48.54	13.70	13.19	24.56
ZnCl ₂	5.22	1.06	2.13	7.72	24.33	32.36	6.57	13.21	47.86

Catalyst, 1 g; feedstock, 1 g peanut shell + 0.3 g CMC; water density, 0.071 g/cm³; reaction time, 20 min; pressure, 22~24.0 MPa.

4. Synergistic Effect of Homogeneous and Heterogeneous Catalyst

4.1. Influence of the Amount of NaOH. In the process of hydrogen production by biomass gasification in supercritical water when Raney-Ni (RTH-5110 type) is used as catalyst in 400°C, the liquid obtained is transparent without the smell of tar. When the mixture of Raney-Ni and NaOH is used as catalyst, the liquid product amount and composition have a great relationship with the amount of NaOH. When the amount of NaOH is low, the residual liquid is transparent and no char is produced. As the amount of NaOH increases, the color of residual liquid becomes yellowish-brown and then brown and the smell of tar becomes stronger. It can be seen that the appropriate amount of NaOH favors biomass gasification and excessive amount of NaOH has restraining effect.

Mass balance of reactions for peanut shell gasification in supercritical water when 1 g RTH-5110 type Raney-Ni (in water slurry state) and 0.0~0.75 g NaOH are used as catalyst in 400°C. The yield of gas increases first and then decreases, and the solid product has increasing trend. The mass balance is within the range of 94.51%~99.60%.

In the temperature of 400°C, initial pressure of 4 MPa, the pressure of 24~28 MPa, residence time of 20 min, with the concentration of 10 wt%, and the mixture of 1 g RTH-5110 type Raney-Ni (in water slurry state) and 0.0~0.75 g NaOH are used as catalyst. The gasification characteristics

of peanut shell in supercritical water can be seen in Figure 1 and the mass balance can be seen in Table 7. It can be seen that as the amount of NaOH increases, gasification efficiency, carbon gasification efficiency, and hydrogen yield all increase first and then decrease and peak when the amount of NaOH equals 0.25 g. The gasification efficiency, carbon gasification efficiency, and hydrogen fraction are 110.95%, 86.57%, and 172.02%, respectively. Compared with the reaction condition without NaOH, the amplification is 8.48%, 15.87%, and 52.37%, respectively. As the amount of NaOH increases to 0.75 g, the gasification efficiency, carbon gasification efficiency, and hydrogen fraction are 69.11%, 50.64%, and 143.32%. Compared with the reaction condition without NaOH, the decline is 33.36%, 20.06%, and 23.67%, respectively.

NaOH is a catalyst with strong alkaline, and it can enhance hydrogen production by biomass gasification. Meanwhile, when NaOH and Raney-Ni are mixed, good catalytic effect is obtained. However, the amount of NaOH has an optimum value and it is speculated that excessive amount of NaOH has restraining effect on the effect of Raney-Ni.

It can be seen from Figure 2 that catalytic effect of different amount of NaOH is investigated at the reaction temperature of 400°C, initial pressure of 4 MPa, reaction pressure of 24~28 MPa, residence time of 20 min, concentration of feedstock 10 wt%, and 1 g RTH-5110 Raney-Ni (in water slurry state). It can be observed that as the amount of NaOH

TABLE 5: Mass balance for heterogeneous catalyst investigation.

Catalyst	W_R/g	W_G/g	W_L/g	W_S/g	$(W_G + W_L + W_S - W_R)/g$	Mass balance coefficient $Q_m/\%$
Noncatalytic	11.3	0.49	9.94	0.54	0.33	97.09
R-Ni, RH3110	12.3	0.24	10.98	0.71	0.37	96.99
R-Ni, RH4110	12.3	0.40	10.92	0.71	0.27	97.82
R-Ni, RH5110	12.3	0.34	10.15	0.87	0.94	92.36
Olivine	12.3	0.39	10.06	0.99	0.86	93.04
Dolomite	12.3	0.36	10.48	0.77	0.69	94.39

TABLE 6: Experimental results for different heterogeneous catalysts.

Catalyst	Gas yield (mmol/g feedstock)				CGE (%)	Gas composition (%)			
	H ₂	CO	CH ₄	CO ₂		H ₂	CO	CH ₄	CO ₂
Noncatalytic	2.86	2.19	1.71	6.48	23.16	21.60	16.54	12.92	48.94
R-Ni, RH3110	9.57	1.63	12.11	16.18	66.73	23.92	4.07	30.26	40.43
R-Ni, RH4110	8.34	1.04	10.61	15.10	59.66	23.55	2.94	29.95	42.64
R-Ni, RH5110	10.78	1.38	9.41	13.00	53.07	31.18	3.99	27.22	37.60
Olivine	4.18	0.88	1.94	7.61	23.25	28.61	6.02	13.28	52.09
Dolomite	3.94	1.33	1.96	3.62	15.42	36.31	12.26	18.06	33.36

Catalyst, 1 g; feedstock, 1 g peanut shell + 0.3 g CMC; water density, 0.071 g/cm³; reaction time, 20 min; pressure, 22~24.0 MPa.

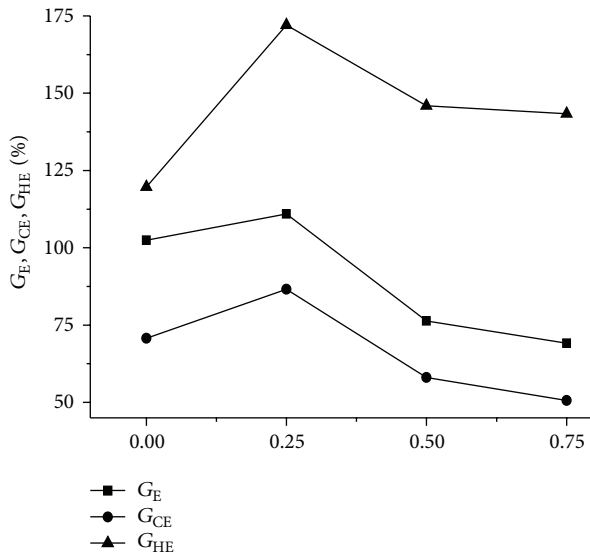


FIGURE 1: The effect of amount of NaOH upon the hydrogen yield and potential hydrogen yield (water : CMC : feedstock : Raney-Ni = 10 g : 0.3 g : 1 g : 1 g, temperature: 400°C, and residence time: 20 min).

increases, the hydrogen fraction increases first and then decreases. The fractions of methane and carbon dioxide have decreasing trend, and the fraction of CO increases slightly and then remains constant. The hydrogen fraction is 59.23% when the amount of NaOH is 0.5 g, and the amplification of hydrogen fraction is 28.35% when the amount of NaOH is 0.75 g. The fraction of carbon dioxide is 37.23% with no NaOH added, while the fraction of carbon dioxide is 23.99% when the amount of NaOH is 0.75 g. The fraction of methane

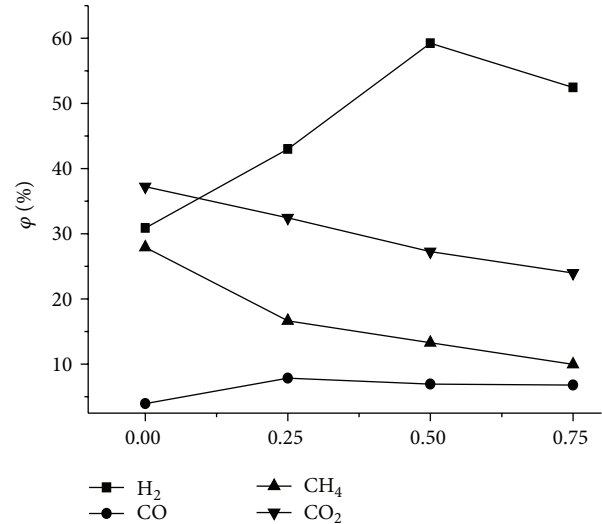


FIGURE 2: The influence of NaOH on the gas fraction (%) (water : CMC : biomass : Raney-Ni = 10 g : 0.3 g : 0.1 g : 1 g, temperature: 400°C, and residence time: 20 min).

decreases from 27.93% to 9.97% when the amount of NaOH increases from 0 to 0.75 g. It can be seen that the addition of NaOH can restrain the formation of methane. As a typical basic catalyst, NaOH can absorb carbon dioxide and promote the water-gas shift reaction toward the direction of hydrogen formation.

Figure 3 shows the hydrogen yield and hydrogen yield potential by supercritical water gasification of peanut shell versus the amount of NaOH. As the amount of NaOH increases, hydrogen yield and hydrogen yield potential [50]

TABLE 7: Mass balance for the mixture of NaOH and Raney-Ni as catalyst.

Mass of NaOH/g	W_R/g	W_G/g	W_L/g	W_S/g	$(W_G + W_L + W_S - W_R)/g$	Mass balance coefficient $Q_m/\%$
0.00	12.30	1.02	10.25	0.84	0.19	98.44
0.25	12.55	1.11	10.46	0.93	0.05	99.60
0.50	12.80	0.76	10.51	1.04	0.49	96.15
0.75	13.05	0.69	10.43	1.21	0.72	94.51

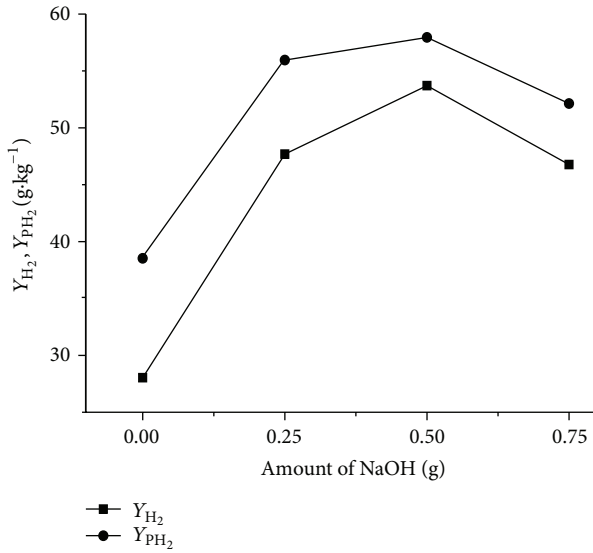


FIGURE 3: The hydrogen yield and hydrogen yield potential by supercritical water gasification of peanut shell versus the amount of NaOH (water: CMC: biomass: Raney-Ni = 10 g: 0.3 g: 1 g: 1 g, temperature: 400°C, and residence time: 20 min).

by supercritical water gasification of peanut shell increase first and then decrease. When the amount of NaOH is 0.5 g, they obtained the maximum value. When NaOH is not present, the hydrogen yield and hydrogen yield potential are 28.02 $g \cdot kg^{-1}$ and 38.53 $g \cdot kg^{-1}$, respectively. As the amount of NaOH increases to 0.25 g, the hydrogen yield and hydrogen yield potential are 47.69 $g \cdot kg^{-1}$ and 55.95 $g \cdot kg^{-1}$, respectively, and the increments are 25.68 $g \cdot kg^{-1}$ and 19.41 $g \cdot kg^{-1}$, respectively. However, when the amount of NaOH increases further, the hydrogen yield and hydrogen yield potential decrease. When the amount of NaOH equals 0.75 g, the hydrogen yield and hydrogen yield potential are 46.77 $g \cdot kg^{-1}$ and 52.14 $g \cdot kg^{-1}$, respectively. It is presumed that excess amount of NaOH prevents the contact of the active center and the biomass particle and results in the lower gasification efficiency, carbon gasification efficiency, and hydrogen yield.

4.2. Synergistic Effect of Catalyst. The synergistic effect of Raney-Ni and NaOH can be seen in Figure 4. The yield of hydrogen by peanut shell supercritical water gasification is 7.44 $g \cdot kg^{-1}$ without catalyst. The yield of hydrogen is

11.43 $g \cdot kg^{-1}$ with NaOH as catalyst and 11.43 $g \cdot kg^{-1}$ with RTH-5110 Raney-Ni as catalyst. The yield of hydrogen is as high as 53.71 $g \cdot kg^{-1}$ when both NaOH and Raney-Ni are used as catalyst. It can be deduced that the mixing effect of Raney-Ni and NaOH is as follows:

$$(53.71 - 7.44) - ((11.43 - 7.44) + (28.03 - 7.44)) = 21.69 \text{ g} \cdot \text{kg}^{-1}. \quad (4)$$

The reason for the synergistic effect of Raney-Ni and NaOH is analyzed. The process of biomass gasification in supercritical water is a typical multiphase chemical reaction. NaOH can dissolve in supercritical water to form a uniform slurry, and it can react with biomass particle and leads to the formation of formats, which subsequently degrades to hydrogen and carbon dioxide [18]. Char formation was considerably suppressed. NaOH could also accelerate the gasification of phenols [20] and reinforce the hydrogenation of phenol to form benzene and further to cyclohexane for hydrogen production [22]. Raney-Ni is a kind of particle catalyst that can react with liquid and gas intermediate. It favors breaking the C-C bond and C-H bonds to obtain gas and liquid product in small molecular to enhance the carbon conversion at relatively low temperature [40]. Raney-Ni can also future adjust the gas fraction by water-gas shift reaction and methanation reaction. So the Raney-Ni and NaOH have a synergistic effect in the biomass gasification in supercritical water.

5. Conclusion

Peanut shell is selected as typical biomass to investigate the catalytic gasification result of biomass in supercritical water at the temperature of 400°C, pressure of 22~24 MPa, and residence time of 20 min. The order of catalytic effect on hydrogen yield of biomass gasification is as follows: KOH > Ca(OH)₂ > K₂CO₃ > LiOH > NaOH > Na₂CO₃. The order of catalytic effect on hydrogen yield of biomass gasification is as follows: LiOH > Ca(OH)₂ > KOH > K₂CO₃ > NaOH > Na₂CO₃. As for Raney-Ni, RTH-3110 has the highest carbon gasification efficiency and RTH-5110 has the highest hydrogen yield. The mixture of Raney-Ni and NaOH shows great synergistic effect in the process of biomass gasification in supercritical water.

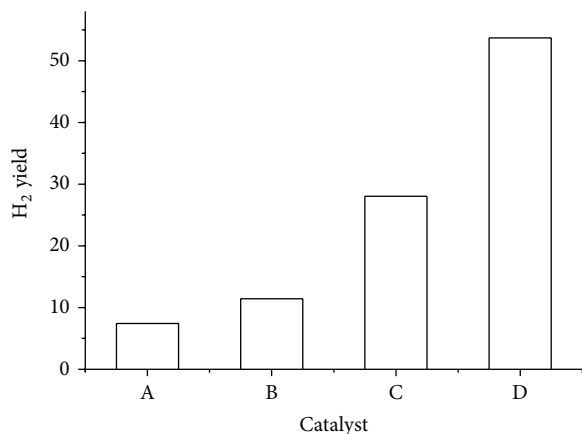


FIGURE 4: The mixed effect of Raney-Ni and NaOH/g·kg⁻¹. Reaction temperature: 400°C, reaction pressure: 24~28 MPa, initial pressure: 4 MPa, residence time: 20 min, and concentration of feedstock: 10% (A: none; B: 0.5 g NaOH; C: 1.0 g Raney-Ni; D: 0.5 g NaOH + 1.0 g Raney-Ni).

Nomenclature

- G_{CE} : Carbon gasification efficiency, the mass of carbon element in gaseous product/the mass of carbon in dry matter in the water-coal-slurry
- G_E : Gasification efficiency, the mass of gaseous product/the mass of dry matter in the water-coal-slurry
- G_{HE} : Hydrogen gasification efficiency, the mass of hydrogen gas/the mass of hydrogen in dry matter in the water-coal-slurry
- W_G : Sum mass of gas product
- W_L : Sum mass of liquid product
- W_R : Sum mass of reactant
- W_S : Sum mass of solid product
- Y_{H_2} : Yield of hydrogen, the mass of certain gas product divided by the mass of dry matter in feedstock
- Y_{PH_2} : Hydrogen yield potential, defined as the sum of measured hydrogen and the hydrogen which could theoretically be formed by completely shifting carbon monoxide and completely reforming hydrocarbon species.

Conflict of Interests

The authors declare that there is no conflict of interests regarding the publication of this paper.

Acknowledgments

This work was financially supported by the National Natural Science Foundation of China (Contract nos. 51306145 and 51323011) and the National Basic Research Program of China (Contract no. 2012CB215303).

References

- [1] H. Jin, Y. Lu, L. Guo, C. Cao, and X. Zhang, "Hydrogen production by partial oxidative gasification of biomass and its model compounds in supercritical water," *International Journal of Hydrogen Energy*, vol. 35, no. 7, pp. 3001–3010, 2010.
- [2] L. Fiori, M. Valbusa, and D. Castello, "Supercritical water gasification of biomass for H₂ production: process design," *Bioresource Technology*, vol. 121, pp. 139–147, 2012.
- [3] E. Kipçak and M. Akgün, "Oxidative gasification of olive mill wastewater as a biomass source in supercritical water: effects on gasification yield and biofuel composition," *Journal of Supercritical Fluids*, vol. 69, pp. 57–63, 2012.
- [4] N. Akiya and P. E. Savage, "Roles of water for chemical reactions in high-temperature water," *Chemical Reviews*, vol. 102, no. 8, pp. 2725–2750, 2002.
- [5] S. Wang, Y. Guo, L. Wang, Y. Wang, D. Xu, and H. Ma, "Supercritical water oxidation of coal: investigation of operating parameters' effects, reaction kinetics and mechanism," *Fuel Processing Technology*, vol. 92, no. 3, pp. 291–297, 2011.
- [6] L. Guo and H. Jin, "Boiling coal in water: hydrogen production and power generation system with zero net CO₂ emission based on coal and supercritical water gasification," *International Journal of Hydrogen Energy*, vol. 38, no. 29, pp. 12953–12967, 2013.
- [7] Y. Yoshida, K. Dowaki, Y. Matsumura et al., "Comprehensive comparison of efficiency and CO₂ emissions between biomass energy conversion technologies—position of supercritical water gasification in biomass technologies," *Biomass & Bioenergy*, vol. 25, no. 3, pp. 257–272, 2003.
- [8] M. J. Antal Jr., S. G. Allen, D. Schulman, X. Xu, and R. J. Divilio, "Biomass gasification in supercritical water," *Industrial & Engineering Chemistry Research*, vol. 39, no. 11, pp. 4040–4053, 2000.
- [9] Y. E. Gorbaty and A. G. Kalinichev, "Hydrogen bonding in supercritical water. 1. Experimental results," *Journal of Physical Chemistry*, vol. 99, no. 15, pp. 5336–5340, 1995.
- [10] T. Adschiri, Y. Hakuta, and K. Arai, "Hydrothermal synthesis of metal oxide fine particles at supercritical conditions," *Industrial & Engineering Chemistry Research*, vol. 39, no. 12, pp. 4901–4907, 2000.
- [11] P. E. Savage, "Organic chemical reactions in supercritical water," *Chemical Reviews*, vol. 99, no. 2–3, pp. 603–621, 1999.
- [12] M. D. Bermejo and M. J. Cocero, "Supercritical water oxidation: a technical review," *AIChE Journal*, vol. 52, no. 11, pp. 3933–3951, 2006.
- [13] M. D. Bermejo, M. J. Cocero, and F. Fernández-Polanco, "A process for generating power from the oxidation of coal in supercritical water," *Fuel*, vol. 83, no. 2, pp. 195–204, 2004.
- [14] Y. Lu, L. Guo, X. Zhang, and Q. Yan, "Thermodynamic modeling and analysis of biomass gasification for hydrogen production in supercritical water," *Chemical Engineering Journal*, vol. 131, no. 1–3, pp. 233–244, 2007.
- [15] P. Azadi and R. Farnood, "Review of heterogeneous catalysts for sub- and supercritical water gasification of biomass and wastes," *International Journal of Hydrogen Energy*, vol. 36, no. 16, pp. 9529–9541, 2011.
- [16] H. de Lasa, E. Salaices, J. Mazumder, and R. Lucky, "Catalytic steam gasification of biomass: catalysts, thermodynamics and kinetics," *Chemical Reviews*, vol. 111, no. 9, pp. 5404–5433, 2011.
- [17] Y. Guo, S. Z. Wang, D. H. Xu, Y. M. Gong, H. H. Ma, and X. Y. Tang, "Review of catalytic supercritical water gasification for

- hydrogen production from biomass," *Renewable & Sustainable Energy Reviews*, vol. 14, no. 1, pp. 334–343, 2010.
- [18] A. Kruse, D. Meier, P. Rimbrecht, and M. Schacht, "Gasification of pyrocatechol in supercritical water in the presence of potassium hydroxide," *Industrial & Engineering Chemistry Research*, vol. 39, no. 12, pp. 4842–4848, 2000.
- [19] M. B. García Jarana, J. Sánchez-Oneto, J. R. Portela, E. Nebot Sanz, and E. J. Martínez de la Ossa, "Supercritical water gasification of industrial organic wastes," *Journal of Supercritical Fluids*, vol. 46, no. 3, pp. 329–334, 2008.
- [20] Z. R. Xu, W. Zhu, M. Gong, and H. W. Zhang, "Direct gasification of dewatered sewage sludge in supercritical water—part 1: effects of alkali salts," *International Journal of Hydrogen Energy*, vol. 38, no. 10, pp. 3963–3972, 2013.
- [21] C. Cao, L. Guo, H. Jin, S. Guo, Y. Lu, and X. Zhang, "The influence of alkali precipitation on supercritical water gasification of glucose and the alkali recovery in fluidized-bed reactor," *International Journal of Hydrogen Energy*, vol. 38, no. 30, pp. 13293–13299, 2013.
- [22] Y. Guo, S. Z. Wang, Y. Z. Wang, J. Zhang, D. H. Xu, and Y. M. Gong, "Gasification of two and three-components mixture in supercritical water: influence of NaOH and initial reactants of acetic acid and phenol," *International Journal of Hydrogen Energy*, vol. 37, no. 3, pp. 2278–2286, 2012.
- [23] Y. Li, L. Guo, X. Zhang, H. Jin, and Y. Lu, "Hydrogen production from coal gasification in supercritical water with a continuous flowing system," *International Journal of Hydrogen Energy*, vol. 35, no. 7, pp. 3036–3045, 2010.
- [24] S. Guo, L. Guo, C. Cao, J. Yin, Y. Lu, and X. Zhang, "Hydrogen production from glycerol by supercritical water gasification in a continuous flow tubular reactor," *International Journal of Hydrogen Energy*, vol. 37, no. 7, pp. 5559–5568, 2012.
- [25] H. Schmieder, J. Abeln, N. Boukis et al., "Hydrothermal gasification of biomass and organic wastes," *Journal of Supercritical Fluids*, vol. 17, no. 2, pp. 145–153, 2000.
- [26] A. Sinağ, A. Kruse, and V. Schwarzkopf, "Key compounds of the hydrolysis of glucose in supercritical water in the presence of K_2CO_3 ," *Industrial & Engineering Chemistry Research*, vol. 42, no. 15, pp. 3516–3521, 2003.
- [27] K. S. Lin, H. P. Wang, and M. C. Li, "Oxidation of 2,4-dichlorophenol in supercritical water," *Chemosphere*, vol. 36, no. 9, pp. 2075–2083, 1998.
- [28] S. Y. Lin, M. Harada, Y. Suzuki, and H. Hatano, "Continuous experiment regarding hydrogen production by Coal/CaO reaction with steam (II) solid formation," *Fuel*, vol. 85, no. 7–8, pp. 1143–1150, 2006.
- [29] H. Ramsurn, S. Kumar, and R. B. Gupta, "Enhancement of biochar gasification in alkali hydrothermal medium by passivation of inorganic components using $Ca(OH)_2$," *Energy & Fuels*, vol. 25, no. 5, pp. 2389–2398, 2011.
- [30] P. D'Jesús, N. Boukis, B. Kraushaar-Czarnetzki, and E. Dinjus, "Gasification of corn and clover grass in supercritical water," *Fuel*, vol. 85, no. 7–8, pp. 1032–1038, 2006.
- [31] C. F. Wu and P. T. Williams, "Hydrogen production by steam gasification of polypropylene with various nickel catalysts," *Applied Catalysis B: Environmental*, vol. 87, no. 3–4, pp. 152–161, 2009.
- [32] L. H. Zhang, C. B. Xu, and P. Champagne, "Activity and stability of a novel Ru modified Ni catalyst for hydrogen generation by supercritical water gasification of glucose," *Fuel*, vol. 96, pp. 541–545, 2012.
- [33] P. Azadi, E. Afif, H. Foroughi, T. S. Dai, F. Azadi, and R. Farnood, "Catalytic reforming of activated sludge model compounds in supercritical water using nickel and ruthenium catalysts," *Applied Catalysis B: Environmental*, vol. 134–135, pp. 265–273, 2013.
- [34] P. Azadi, S. Khan, F. Strobel, F. Azadi, and R. Farnood, "Hydrogen production from cellulose, lignin, bark and model carbohydrates in supercritical water using nickel and ruthenium catalysts," *Applied Catalysis B: Environmental*, vol. 117–118, pp. 330–338, 2012.
- [35] Y. Matsumura, X. Xu, and M. J. Antal, "Gasification characteristics of an activated carbon in supercritical water," *Carbon*, vol. 35, no. 6, pp. 819–824, 1997.
- [36] X. D. Xu, Y. Matsumura, J. Stenberg, and M. J. Antal, "Carbon-catalyzed gasification of organic feedstocks in supercritical water," *Industrial & Engineering Chemistry Research*, vol. 35, no. 8, pp. 2522–2530, 1996.
- [37] D. C. Elliott, "Catalytic hydrothermal gasification of biomass," *Biofuels, Bioproducts & Biorefining*, vol. 2, no. 3, pp. 254–265, 2008.
- [38] M. Osada, O. Sato, K. Arai, and M. Shirai, "Stability of supported ruthenium catalysts for lignin gasification in supercritical water," *Energy & Fuels*, vol. 20, no. 6, pp. 2337–2343, 2006.
- [39] A. J. Byrd, K. K. Pant, and R. B. Gupta, "Hydrogen production from glucose using Ru/Al_2O_3 catalyst in supercritical water," *Industrial & Engineering Chemistry Research*, vol. 46, no. 11, pp. 3574–3579, 2007.
- [40] T. Minowa and T. Ogi, "Hydrogen production from cellulose using a reduced nickel catalyst," *Catalysis Today*, vol. 45, no. 1–4, pp. 411–416, 1998.
- [41] X. Hao, L. Guo, X. Zhang, and Y. Guan, "Hydrogen production from catalytic gasification of cellulose in supercritical water," *Chemical Engineering Journal*, vol. 110, no. 1–3, pp. 57–65, 2005.
- [42] A. Sinağ, A. Kruse, and J. Rathert, "Influence of the heating rate and the type of catalyst on the formation of key intermediates and on the generation of gases during hydrolysis of glucose in supercritical water in a batch reactor," *Industrial & Engineering Chemistry Research*, vol. 43, no. 2, pp. 502–508, 2004.
- [43] J. M. Encinar, F. J. Beltrán, A. Ramiro, and J. F. González, "Pyrolysis/gasification of agricultural residues by carbon dioxide in the presence of different additives: influence of variables," *Fuel Processing Technology*, vol. 55, no. 3, pp. 219–233, 1998.
- [44] A. Pei, L. Guo, and H. Jin, "Experimental research on catalysts and their catalytic mechanism for hydrogen production by gasification of peanut shell in supercritical water," *Frontiers of Energy and Power Engineering in China*, vol. 1, no. 4, pp. 451–456, 2007.
- [45] A. Pei, L. Zhang, B. Jiang et al., "Hydrogen production by biomass gasification in supercritical or subcritical water with Raney-Ni and other catalysts," *Frontiers of Energy and Power Engineering in China*, vol. 3, no. 4, pp. 456–464, 2009.
- [46] S. Morrin, P. Lettieri, C. Chapman, and L. Mazzei, "Two stage fluid bed-plasma gasification process for solid waste valorisation: technical review and preliminary thermodynamic modelling of sulphur emissions," *Waste Management*, vol. 32, no. 4, pp. 676–684, 2012.
- [47] Y. Li and Z. Wu, "Effects of catalytic cracking conditions on biomass tar cracking," *Journal of Tsinghua University*, vol. 49, no. 2, pp. 253–256, 2009.
- [48] P. A. Simell, J. K. Leppälähti, and J. B.-S. Bredenberg, "Catalytic purification of tarry fuel gas with carbonate rocks and ferrous materials," *Fuel*, vol. 71, no. 2, pp. 211–218, 1992.

- [49] V. Vassilatos, G. Taralas, K. Sjostrom, and E. Bjornbom, "Catalytic cracking of tar in biomass pyrolysis gas in the presence of calcined dolomite," *Canadian Journal of Chemical Engineering*, vol. 70, no. 5, pp. 1008–1013, 1992.
- [50] S. Turn, C. Kinoshita, Z. Zhang, D. Ishimura, and J. Zhou, "An experimental investigation of hydrogen production from biomass gasification," *International Journal of Hydrogen Energy*, vol. 23, no. 8, pp. 641–648, 1998.

Research Article

Revisiting the Zinc-Blende/Wurtzite Heterocrystalline Structure in CdS

Zhaohui Zhou, Mingtao Li, Po Wu, and Liejin Guo

International Research Center for Renewable Energy (IRCRES), State Key Laboratory of Multiphase Flow in Power Engineering (MFPE), Xi'an Jiaotong University (XJTU), 28 West Xianning Road, Xi'an 710049, China

Correspondence should be addressed to Zhaohui Zhou; zzhlx@mail.xjtu.edu.cn and Liejin Guo; lj-guo@mail.xjtu.edu.cn

Received 19 March 2014; Accepted 23 May 2014; Published 10 June 2014

Academic Editor: Shaohua Shen

Copyright © 2014 Zhaohui Zhou et al. This is an open access article distributed under the Creative Commons Attribution License, which permits unrestricted use, distribution, and reproduction in any medium, provided the original work is properly cited.

The band offset at CdS zinc-blende (ZB)/wurtzite (WZ) heterocrystalline interface was revisited using the first principles calculations with the local density approximation (LDA), generalized gradient approximation (GGA), and Heyd-Scuseria-Ernzerhof (HSE06) hybrid functional. It was revealed that, unlike most IV, III-V, and II-VI semiconductors, the band alignment at CdS ZB/WZ heterocrystalline interface was of type-I with straddling lineup of band edges, which was irrespective of the exchange-correlation energy functional, the thickness of ZB and WZ segments, and the ZB/WZ interface location. The partial charge densities of VBM and CBM states were separated around two adjacent interfaces in one unit cell of heterocrystalline superlattice. This type of carrier localization was mainly attributed to the spontaneous polarization occurring in the WZ segment rather than the band offset at the interface.

1. Introduction

The zinc-blende (ZB)/wurtzite (WZ) heterocrystalline structure can form a new type of superlattice [1]. This type of superlattice had the potential to produce the “anomalous photovoltaic effect” [2, 3] and thus may be applied in the solar energy conversion and utilization. As a prototypical example, ZB/WZ heterocrystalline structure in SiC has been extensively studied [4–7]. It has been established that the spontaneous polarization, valence band offset, and quantum confinement effect were three key effects in the heterocrystalline superlattice which should be considered [8]. The band alignment of type-II at ZB/WZ interface was determined by density functional theory (DFT) calculations on ZB and WZ bulk IV, III-V and II-VI semiconductors [9], and confirmed by the Photoluminescence measurements and tight-binding calculations on InP and GaAs [10–12]. It has also been reported that this type of band alignment can be tuned by the diameter of ZB/WZ superlattice nanowires [13].

CdS is an important energy material in photovoltaic cells, photoelectrochemical, or photocatalytic water splitting [14–19]. Li et al. found that phase junctions on TiO₂ and Ga₂O₃

can significantly improve the efficiency for hydrogen production [20, 21]. Thus, it is meaningful to introduce the concept of phase junction into the design of CdS photocatalyst. Murayama and Nakayama calculated the valence band offset at CdS ZB/WZ heterocrystalline interface using a plane wave pseudopotential method without considering the ZB/WZ interface effect [9]. Wei and Zhang calculated the valence band offset with the interface dipole using a linearized augmented plane wave method [22]. Both studies gave a band alignment of type-II with staggered lineup of band edges at CdS ZB/WZ interface. However, we noticed that the spontaneous polarization occurring in the WZ structure was not taken into consideration in determining the valence band offset. Such an effect was important to determine the band offsets at the interface and carrier distribution in the superlattice.

In this paper, the band offset at CdS ZB/WZ heterocrystalline interface was determined with the first-principles calculations. Three exchange-correlation energy functionals, different number of ZB or WZ atomic layers in one unit cell and different interface locations were considered to verify the reliability of calculated results. The carrier distribution

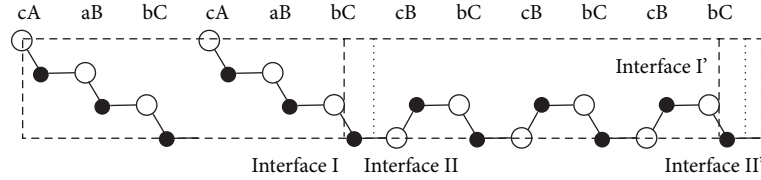


FIGURE 1: Schematic diagram of one unit cell in CdS ZB/WZ heterocrystalline superlattice with 6 zinc-blende (ZB) and 6 wurtzite (WZ) atomic layers. Empty circle represents S atom and solid circle represents Cd atom. Vertical dashed and dotted lines indicate the locations of abrupt interfaces I and II, respectively.

in ZB/WZ heterocrystalline superlattice was explained by the effect of spontaneous polarization.

2. Computational Methods

The unit cell in CdS ZB/WZ heterocrystalline superlattice was made up of a number of ZB and WZ atomic layers along ZB (111) and WZ (0001) directions, as shown in Figure 1. The calculations were carried out by using the Vienna *ab initio* Simulation Package (VASP) [23, 24]. The plane wave and projector augmented wave potentials (PAW) method [25] were employed in the framework of DFT. Local density approximation (LDA-PZ-CA) [26, 27], generalized gradient approximation (GGA-PBE) [28], and HSE06 hybrid functionals [29, 30] were used to examine the effect of the exchange-correlation energy on the band alignment at the interface. For HSE06 hybrid functional, 30% of Hartree-Fock exchange was used to produce a band gap agreeing well with the experimental value. The kinetic energy cutoff was chosen as 380 eV. The Monkhorst-Pack k-point meshes [31] were $9 \times 9 \times 9$ for bulk ZB phase CdS, $9 \times 9 \times 5$ for bulk WZ phase, and $9 \times 9 \times 1$ for the heterocrystalline superlattice. When the hybrid functional was used, these k-point meshes were somewhat reduced to save the computational cost.

The method to determine the band offset [32] was described in the following three steps: first, to calculate the energy difference between the valence band maximum (VBM) and macroaveraged electrostatic potential through bulk calculations; second, to calculate the difference in the macroaveraged electrostatic potential across the ZB/WZ interface through the interface calculations; third, to determine the valence band offset (VBO) by combining the energy differences in bulk calculations and the potential difference across the interface, and furthermore the conduction band offset (CBO) from VBO and the difference in band gap between ZB and WZ phase CdS.

3. Results and Discussions

The calculated structural parameters and band gaps of bulk ZB and WZ CdS were shown in Table 1. The structural parameters from LDA and GGA-PBE calculations slightly deviated from those experimental values. The hybrid functional HSE06 calculations used the crystal structure optimized by GGA calculations and showed a large improvement on the band gap with respect to LDA and GGA calculations. When building the ZB/WZ interface, the structural parameter in the

TABLE 1: Calculated and experimental structural parameters (a , c , and u) and band gap (E_g) of zinc-blende (ZB) and wurtzite (WZ) CdS.

Properties	LDA	GGA-PBE	HSE06	Experiment ^a
$a_{\text{ZB}}/\text{\AA}$	5.770	5.944		5.818
$a_{\text{WZ}}/\text{\AA}$	4.087	4.210		4.136
$c_{\text{WZ}}/\text{\AA}$	6.668	6.856		6.714
$(c/a)_{\text{WZ}}$	1.632	1.628		1.623
u_{WZ}	0.3758	0.3762		0.3730 ^b
E_g (ZB)/eV	0.96	1.04	2.29	2.37 ^c
E_g (WZ)/eV	1.03	1.10	2.36	2.48 ^d

^a[22], ^b[34], ^c[35], and ^d[36].

interface was taken to be the average value of $a_{\text{ZB}}/\sqrt{2}$ and a_{WZ} in the planes perpendicular to ZB (111) and WZ (0001) direction. The lattice mismatch at this interface was estimated within 0.1% and thus the lattice strain was very small.

3.1. Band Offset. The spontaneous polarization occurring in the WZ segment in the heterocrystalline superlattice resulted in a macroaveraged electrostatic potential with the sawtooth-like shape, as shown in Figure 2. The potential difference at the ZB/WZ interface cannot be estimated straightforwardly because of the spontaneous polarization which was not remarkable in the conventional heterojunction. The method proposed by Qteish et al. [4] was employed to exclude the effect of the spontaneous polarization on the determination of band offsets. The potential difference can be regarded as the discontinuity in the electrostatic potential at the ZB/WZ interface which was determined by linearly extrapolating the macroaveraged electrostatic potentials on both sides of the interface. There are two ways to define the abrupt interface, which were reported in the literature. Interface I was defined from the viewpoint of local environment “seen” by the interface [33], and interface II was located according to the analysis of charge distribution [4]. Both types of interfaces were examined in this paper. The macroaveraged valence charge density around the interface significantly deviated from that in the bulk region, reflecting the effect of the interface.

The calculated band offsets at CdS ZB/WZ heterocrystalline interface were summarized in Table 2. A clear band alignment of type-I was manifested from all of our results, regardless of the exchange-correlation energy functional, the

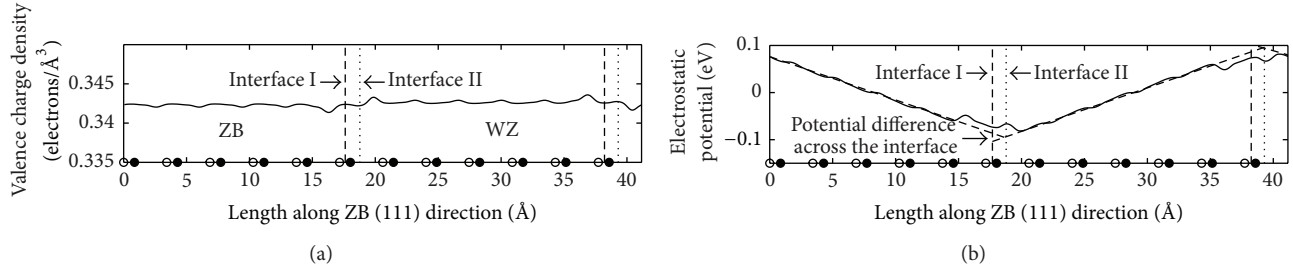


FIGURE 2: (a) Macroaveraged valence charge density and (b) macroaveraged electrostatic potential in CdS ZB/WZ heterocrystalline superlattice. For empty and solid circles and vertical dashed and dotted lines, please see Figure 1.

TABLE 2: Band offset (VBO and CBO) at CdS ZB/WZ heterocrystalline interface (values in parentheses without considering the interface dipole) and band gap (E_g) with different zinc-blende (ZB) and wurtzite (WZ) atomic layers.

Properties	Murayama ^a	Wei ^b	ZB/WZ layers	LDA	GGA-PBE interface		HSE06
					I	II	
VBO/meV	(19)	46 (-1)	6/6	-23 (-31)	-38 (-18)	-17 (-18)	-36 (-18)
			12/12		-43 (-18)	-20 (-18)	
			24/12		-40 (-18)	-17 (-18)	
CBO/meV	(73)	115 (68)	6/6	44 (36)	25 (45)	46 (45)	35 (53)
			12/12		20 (45)	43 (45)	
			24/12		23 (45)	46 (45)	
E_g /eV			6/6	0.964	1.025		2.268
			12/12		0.875		
			24/12		0.727		

^a[9]; ^b[22].

size of unit cell, and the interface location and dipole. GGA-PBE and HSE06 methods produced similar VBOs which were slightly larger than the value from LDA method. The thickness of ZB and WZ segments in one unit cell had a large influence on the band gap, but hardly affected the band offsets. The interface dipole changed with the choice of interface location, decreasing from interface I to II. This resulted in a larger VBO at interface I than at interface II. In order to further verify the reliability of the calculated band offsets, the well-known VBO at SiC ZB/WZ interface was examined here. A VBO of 0.12 eV was obtained at interface I with LDA, comparable with the reported values of about 0.13 eV [4, 8] and 0.14 eV [6, 37]. The previous study by Murayama and Nakayama gave a band alignment of type-II through ZB and WZ bulk calculations, which used the plane wave pseudopotential and LDA method. We deduced that the inconsistency may be due to the exclusion of d electrons in Cd and Zn atoms in their work. Inclusion of d electrons has been demonstrated to be essential to form correct VBM states [38]. Wei and Zhang reported that the band alignment between CdS ZB and WZ phases was of type-I without the interface dipole, but the band alignment turned to type-II if the ZB/WZ interface was considered [22]. We deduced that the inconsistency may be attributed to the spontaneous polarization occurring in the WZ structure which was not considered in their calculation. The effect of spontaneous polarization was obvious in CdS ZB/WZ heterocrystalline superlattice. The band gap decreased with the thickness of

ZB and WZ segments increasing, due to the spontaneous polarization [6] which may be overestimated by the current first-principles calculations [8].

In addition, the effect of atom relaxation in the supercell was considered. We found that the atom relaxation can be neglected in terms of the small interface atom movement, almost identical band offset, and consistent partial charge distribution (for partial charge, see the text below).

3.2. Carrier Localization. According to the previous reports, the type of band alignment at ZB/WZ interface can be identified by the charge density distribution of VBM and CBM states [1, 22, 39]. We would like to point out that it was a misunderstanding. Figure 3 shows the plane-averaged charge densities of VBM and CBM states in CdS ZB/WZ heterocrystalline superlattice with different thickness of ZB and WZ segments. It can be found that the partial charge densities in CdS ZB-6/WZ-6 superlattice well reproduced those presented by Wei and Zhang [22]. It seems that VBM state was localized in the WZ region while CBM state was localized in the ZB region, and thus this type of carrier distribution was attributed to the type-II band alignment at the ZB/WZ interface, just as Wei and Zhang described. However, as the thickness of ZB and WZ segments increases, we found that VBM and CBM states were actually localized around two adjacent interfaces in one unit cell of the superlattice, instead of on both sides of one single interface. The partial charge

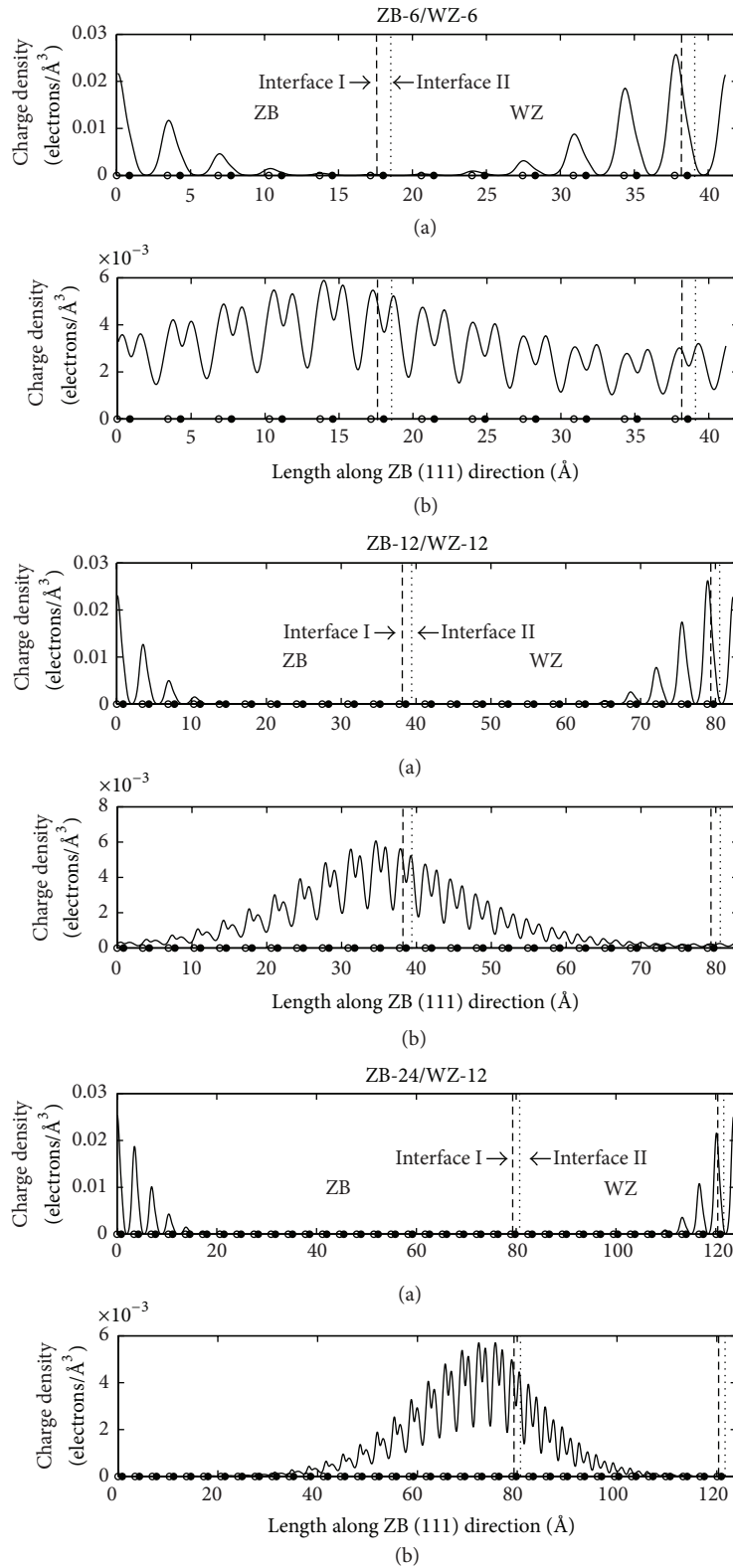


FIGURE 3: Plane-averaged charge densities of (a) VBM and (b) CBM states in three CdS ZB/WZ heterocrystalline superlattices (ZB-6/WZ-6, ZB-12/WZ-12, and ZB-24/WZ-12). For empty and solid circles and vertical dashed and dotted lines, please see Figure 1.

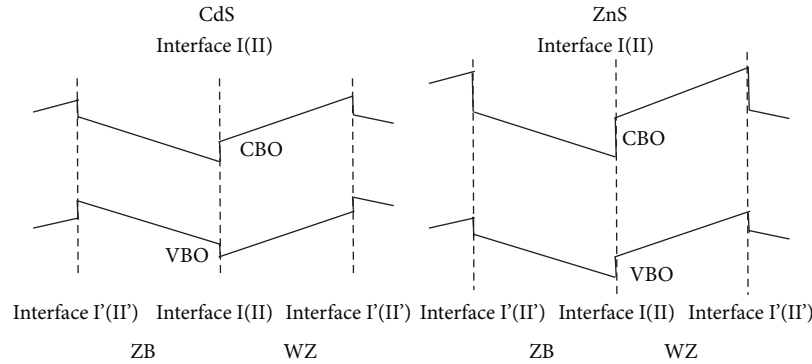


FIGURE 4: The lineups of VBM and CBM in CdS and ZnS ZB/WZ heterocrystalline superlattices.

density of CBM state was more delocalized than that of VBM state because of the smaller effective mass for CBM state.

The character of carrier localization was in good accord with the lineup of VBM and CBM states in CdS ZB/WZ heterocrystalline superlattice, as shown in Figure 4. The lineup of VBM and CBM states was composed of the potential variation resulted from spontaneous polarization, band offset at the interface, and quantum confinement effect. The plane-averaged charge density of VBM state was mainly localized around the interface at the hill of electrostatic potential while that of the CBM state was mainly around the interface at the valley of electrostatic potential. In the CdS ZB/WZ heterocrystalline superlattice, the effect of spontaneous polarization played a decisive role in determining the lineup of VBM or CBM, instead of the band offset.

It has been established that “anomalous photovoltaic effect” took place only in crystals where at least some stacking disorder occurred (i.e., changes in structure from ZB to WZ) [2, 3]. The main feature of this effect was the production of a much larger photovoltage than the band gap. According to “theory of the anomalous photovoltaic effect” [40], the photovoltages produced by two opposing interfaces in one unit cell of heterocrystalline superlattice could not be cancelled completely. This was due to one interface on the hill and the other interface in the valley of the periodic potential, leading to two interfaces with different carrier concentrations and photovoltages. As a result, a net photovoltage can be generated in one unit cell, and after superposing photovoltages of these unit cells, the final large photovoltage was generated. We thought that such a large photovoltage can afford extra power to promote the photocatalytic reaction for hydrogen production. Recently, the nanowires with controlled stacking faults have been fabricated successfully [41]. This provided an opportunity to examine the effect of “anomalous photovoltaic effect” on the photocatalytic reaction.

4. Conclusions

In summary, the band alignment at CdS ZB/WZ heterocrystalline interface was revisited with careful first-principles calculations, and it proved to be of type-I. The inconsistency with previous theoretical studies may be attributed to their incomplete consideration of ZB/WZ heterocrystalline

superlattice. Such a superlattice had the ability to separate photogenerated carriers, and the separation of electrons and holes was mainly due to the spontaneous polarization occurring in the WZ structure, not merely due to the band offset. The spontaneous polarization dominated the distribution of electrostatic potential, and thus resulted in the localization of partial charge densities of VBM and CBM states in the heterocrystalline superlattice. Finally, it can be expected that “anomalous photovoltaic effect” that occurred in the ZB/WZ heterocrystalline superlattice may be applied in the photocatalytic reactions because of the large photovoltage output.

Conflict of Interests

The authors declare that there is no conflict of interests regarding the publication of this paper.

Acknowledgments

This work is supported by the China Postdoctoral Science Foundation (no. 2013M542343), the Fundamental Research Funds for the Central Universities (xjj2013004) and the National Natural Science Foundation of China (No. 51323011).

References

- [1] F. Bechstedt and P. Käckell, “Heterocrystalline structures: new types of superlattices?” *Physical Review Letters*, vol. 75, no. 11, pp. 2180–2183, 1995.
- [2] S. G. Ellis, F. Herman, E. E. Loebner, W. J. Merz, C. W. Struck, and J. G. White, “Photovoltages larger than the band gap in zinc sulfide crystals,” *Physical Review*, vol. 109, no. 5, p. 1860, 1958.
- [3] A. Lempicki, “Anomalous photovoltaic effect in ZnS single crystals,” *Physical Review*, vol. 113, no. 5, pp. 1204–1209, 1959.
- [4] A. Qteish, V. Heine, and R. J. Needs, “Polarization, band lineups, and stability of SiC polytypes,” *Physical Review B*, vol. 45, no. 12, pp. 6534–6542, 1992.
- [5] B. Wenzien, P. Käckell, F. Bechstedt, and G. Cappellini, “Quasi-particle band structure of silicon carbide polytypes,” *Physical Review B*, vol. 52, no. 15, pp. 10897–10905, 1995.

- [6] S.-H. Ke, J. Zi, K.-M. Zhang, and X.-D. Xie, "Electronic structures and band offsets of heterocrystalline superlattices $(3C\text{-AlN})_{3n}/(2H\text{-AlN})_{2n}$ and $(3C\text{-SiC})_{3n}/(2H\text{-SiC})_{2n}$ ($n = 1, 2, 3$)," *Physical Review B: Condensed Matter and Materials Physics*, vol. 54, no. 12, pp. 8789–8793, 1996.
- [7] C. Raffy, J. Furthmüller, and F. Bechstedt, "Properties of interfaces between cubic and hexagonal polytypes of silicon carbide," *Journal of Physics Condensed Matter*, vol. 14, no. 48, pp. 12725–12731, 2002.
- [8] M. S. Miao and W. R. L. Lambrecht, "Magnetic properties of substitutional 3d transition metal impurities in silicon carbide," *Physical Review B*, vol. 68, no. 12, Article ID 155320, 2003.
- [9] M. Murayama and T. Nakayama, "Chemical trend of band offsets at wurtzite/zinc-blende heterocrystalline semiconductor interfaces," *Physical Review B*, vol. 49, no. 7, pp. 4710–4724, 1994.
- [10] J. Bao, D. C. Bell, F. Capasso et al., "Optical properties of rotationally twinned InP nanowire heterostructures," *Nano Letters*, vol. 8, no. 3, pp. 836–841, 2008.
- [11] D. Spirkoska, J. Arbiol, A. Gustafsson et al., "Structural and optical properties of high quality zinc-blende/wurtzite GaAs nanowire heterostructures," *Physical Review B: Condensed Matter and Materials Physics*, vol. 80, no. 24, Article ID 245325, 2009.
- [12] J.-M. Jancu, K. Gauthron, L. Largeau, G. Patriarche, J.-C. Harmand, and P. Voisin, "Type II heterostructures formed by zinc-blende inclusions in InP and GaAs wurtzite nanowires," *Applied Physics Letters*, vol. 97, no. 4, Article ID 041910, 2010.
- [13] T. Akiyama, T. Yamashita, K. Nakamura, and T. Ito, "Band alignment tuning in twin-plane superlattices of semiconductor nanowires," *Nano Letters*, vol. 10, no. 11, pp. 4614–4618, 2010.
- [14] N. Bühler, K. Meier, and J.-F. Reber, "Photochemical hydrogen production with cadmium sulfide suspensions," *Journal of Physical Chemistry*, vol. 88, no. 15, pp. 3261–3268, 1984.
- [15] D. Jing and L. Guo, "A novel method for the preparation of a highly stable and active CdS photocatalyst with a special surface nanostructure," *Journal of Physical Chemistry B*, vol. 110, no. 23, pp. 11139–11145, 2006.
- [16] N. Z. Bao, L. M. Shen, T. Takata, and K. Domen, "Self-templated synthesis of nanoporous CdS nanostructures for highly efficient photocatalytic hydrogen production under visible light," *Chemistry of Materials*, vol. 20, no. 1, pp. 110–117, 2008.
- [17] X. Zong, H. Yan, G. Wu et al., "Enhancement of photocatalytic H_2 evolution on CdS by loading MoS_2 as cocatalyst under visible light irradiation," *Journal of the American Chemical Society*, vol. 130, no. 23, pp. 7176–7177, 2008.
- [18] H. Yan, J. Yang, G. Ma et al., "Visible-light-driven hydrogen production with extremely high quantum efficiency on Pt-PdS/CdS photocatalyst," *Journal of Catalysis*, vol. 266, no. 2, pp. 165–168, 2009.
- [19] J. Yang, H. Yan, X. Wang et al., "Roles of cocatalysts in Pt-PdS/CdS with exceptionally high quantum efficiency for photocatalytic hydrogen production," *Journal of Catalysis*, vol. 290, pp. 151–157, 2012.
- [20] J. Zhang, Q. Xu, Z. Feng, M. Li, and C. Li, "Importance of the relationship between surface phases and photocatalytic activity of TiO_2 ," *Angewandte Chemie*, vol. 47, no. 9, pp. 1766–1769, 2008.
- [21] X. Wang, Q. Xu, M. Li et al., "Photocatalytic overall water splitting promoted by an α - β phase junction on Ga_2O_3 ," *Angewandte Chemie*, vol. 51, no. 52, pp. 13089–13092, 2012.
- [22] S.-H. Wei and S. B. Zhang, "Structure stability and carrier localization in CdX ($X = S, Se, Te$) semiconductors," *Physical Review B: Condensed Matter and Materials Physics*, vol. 62, no. 11, pp. 6944–6947, 2000.
- [23] G. Kresse and J. Furthmüller, "Efficient iterative schemes for ab initio total-energy calculations using a plane-wave basis set," *Physical Review B: Condensed Matter and Materials Physics*, vol. 54, no. 16, pp. 11169–11186, 1996.
- [24] G. Kresse and J. Furthmüller, "Efficiency of ab-initio total energy calculations for metals and semiconductors using a plane-wave basis set," *Computational Materials Science*, vol. 6, no. 1, pp. 15–50, 1996.
- [25] G. Kresse and D. Joubert, "From ultrasoft pseudopotentials to the projector augmented-wave method," *Physical Review B: Condensed Matter and Materials Physics*, vol. 59, no. 3, pp. 1758–1775, 1999.
- [26] D. M. Ceperley and B. J. Alder, "Ground state of the electron gas by a stochastic method," *Physical Review Letters*, vol. 45, no. 7, pp. 566–569, 1980.
- [27] J. P. Perdew and Y. Wang, "Accurate and simple analytic representation of the electron-gas correlation energy," *Physical Review B*, vol. 45, no. 23, pp. 13244–13249, 1992.
- [28] J. P. Perdew, K. Burke, and M. Ernzerhof, "Generalized gradient approximation made simple," *Physical Review Letters*, vol. 77, no. 18, pp. 3865–3868, 1996.
- [29] J. Heyd and G. E. Scuseria, "Efficient hybrid density functional calculations in solids: assessment of the Heyd-Scuseria-Ernzerhof screened Coulomb hybrid functional," *Journal of Chemical Physics*, vol. 121, no. 3, pp. 1187–1192, 2004.
- [30] J. Paier, M. Marsman, K. Hummer, G. Kresse, I. C. Gerber, and J. G. Ángyán, "Screened hybrid density functionals applied to solids," *Journal of Chemical Physics*, vol. 124, no. 15, Article ID 154709, 2006.
- [31] H. J. Monkhorst and J. D. Pack, "Special points for Brillouin-zone integrations," *Physical Review B*, vol. 13, no. 12, pp. 5188–5192, 1976.
- [32] M. Peressi, N. Binggeli, and A. Baldereschi, "Band engineering at interfaces: theory and numerical experiments," *Journal of Physics D: Applied Physics*, vol. 31, no. 11, pp. 1273–1299, 1998.
- [33] J. E. Northrup, J. Ihm, and M. L. Cohen, "Electronic structure of zinc-blende-wurtzite interfaces: $ZnS\text{-}ZnS$ (111-0001) and $ZnSe\text{-}ZnSe$ (111-0001)," *Physical Review B*, vol. 22, no. 4, pp. 2060–2065, 1980.
- [34] K. Nishidate, T. Sato, Y. Matsukura, M. Baba, M. Hasegawa, and T. Sasaki, "Density-functional electronic structure calculations for native defects and Cu impurities in CdS," *Physical Review B: Condensed Matter and Materials Physics*, vol. 74, no. 3, Article ID 035210, 2006.
- [35] Y.-M. Yu, K.-M. Kim, O. B. Byungung, K.-S. Lee, Y. D. Choi, and P. Y. Yu, "Band gap energy and exciton peak of cubic CdS/GaAs epilayers," *Journal of Applied Physics*, vol. 92, no. 2, pp. 1162–1164, 2002.
- [36] O. Madelung, *Semiconductors: Data Handbook*, Springer, New York, NY, USA, 2004.
- [37] S.-H. Ke, K.-M. Zhang, and X.-D. Xie, "Band line-ups and band-gap behaviour of new-type superlattices $(3C\text{-BN})/(2H\text{-BN})$, $(3C\text{-GaN})/(2H\text{-GaN})$ and $(3C\text{-SiC})/(2H\text{-SiC})$," *Journal of Physics Condensed Matter*, vol. 8, no. 49, pp. 10209–10217, 1996.
- [38] S.-H. Wei and A. Zunger, "Role of metal d states in II–VI semiconductors," *Physical Review B*, vol. 37, no. 15, pp. 8958–8981, 1988.
- [39] M. Murayama and T. Nakayama, "Electronic structures of hetero-crystalline semiconductor superlattices," *Journal of the Physical Society of Japan*, vol. 61, no. 7, pp. 2419–2433, 1992.

- [40] G. F. Neumark, "Theory of the anomalous photovoltaic effect of ZnS," *Physical Review*, vol. 125, no. 3, pp. 838–845, 1962.
- [41] P. Caroff, K. A. Dick, J. Johansson, M. E. Messing, K. Deppert, and L. Samuelson, "Controlled polytypic and twin-plane superlattices in III–V nanowires," *Nature Nanotechnology*, vol. 4, no. 1, pp. 50–55, 2009.

Research Article

Preparation and Characterization of Novel Fe₂O₃-Flaky Coated Carbon Fiber by Electrospinning and Hydrothermal Methods

Qing-Yun Chen, Lang Liu, and Yun-Hai Wang

International Research Center for Renewable Energy, State Key Laboratory of Multiphase Flow in Power Engineering, Xi'an Jiaotong University, Xi'an 710049, China

Correspondence should be addressed to Qing-Yun Chen; qychen@mail.xjtu.edu.cn

Received 7 March 2014; Accepted 21 May 2014; Published 4 June 2014

Academic Editor: Ke Sun

Copyright © 2014 Qing-Yun Chen et al. This is an open access article distributed under the Creative Commons Attribution License, which permits unrestricted use, distribution, and reproduction in any medium, provided the original work is properly cited.

A novel hierarchical nanostructure of Fe₂O₃-flaky coated carbon fibers was produced by the electrospinning process followed by a hydrothermal technique. First, electrospinning of a colloidal solution that consisted of ferric nitrate and polyacrylonitrile (PAN) was performed to produce PAN nanofibers. Then electrospun nanofiber was stabilized and calcinated in nitrogen at 800°C for 2 h to produce carbon nanofibers (CNFs) which were exploited to produce Fe₂O₃-flaky structure using hydrothermal technique. The as-obtained products were characterized by scanning electron microscopy (SEM) and X-ray diffraction (XRD). The results revealed that Fe₂O₃ flakes were successfully grown on the CNFs substrates, and the coverage of Fe₂O₃ flakes could be controlled by simply adjusting the hydrothermal pH value and time. Fe₂O₃-flaky coated carbon fibers displayed high photocatalytic activity toward degradation of methyl orange (MO) under visible light irradiation.

1. Introduction

Due to the increasing energy crisis and environment problems, an increasing number of scientific researches have focused on the utilization of solar light to split water [1, 2], reduce carbon dioxide (CO₂) [3, 4], and degrade pollutants [5, 6] by photocatalysis. It has been reported that the nanostructured semiconductor metal oxides, such as TiO₂, ZnO, Bi₂O₃, and Fe₂O₃, are effective photocatalysts under visible-light irradiation [7–10]. Among these semiconductor metal oxide photocatalysts, Fe₂O₃, with a low band gap of 2.2 eV, has been recognized as one of the promising materials for photocatalytic process because of its low cost, simple production, environmental friendliness, and excellent chemical stability [11, 12]. However, enhancing the photocatalytic efficiency of Fe₂O₃ to meet the practical application is still a challenge because photoinduced electron-hole pairs in Fe₂O₃ are difficult to be separated.

Recently, the coupling of the photocatalysts and inert supports is one of the approaches to prepare the composite photocatalysts, which may improve charge separation [13, 14]. Mu et al. reported that ZnO-carbon nanofibers (CNFs) showed high photocatalytic property to degrade rhodamine

B (RB) [15]. Some reports have shown that CNFs could efficiently capture and transport photoinduced electrons through highly conductive long CNFs [16, 17]. Judging from the promising photocatalyst of Fe₂O₃ and the efficient electron transfer property of CNFs, combination of Fe₂O₃ and CNTs seems to be ideal for improving the photocatalytic efficiency.

In this research, we report a successful attempt for the preparation of carbon fiber which supported Fe₂O₃ nanostructures via the combination of simple electrospinning technique and hydrothermal method, and the photocatalytic activity of these nanostructure photocatalysts is investigated by measuring the degradation of methyl orange (MO) as test substances. The novelty of this study mainly stems from the fabricating of Fe₂O₃-flaky coated carbon nanofibers. The influence factors of the morphology and the structure are discussed in detail.

2. Experiments

2.1. Preparation of Carbon Nanofibers. 2 g of polyacrylonitrile (PAN) ($M_w = 150000$) was dissolved in 14 mL of N,N-dimethylformamide (DFM) solution containing 3 wt% of

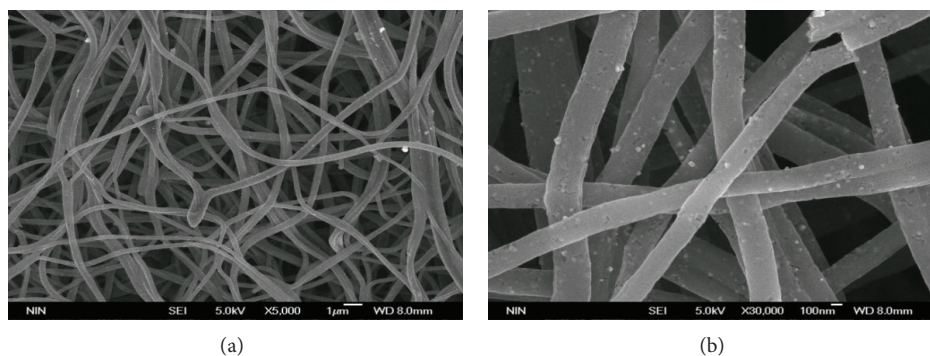


FIGURE 1: SEM images of as-obtained carbonized PAN fiber: (a) low magnification and (b) high magnification.

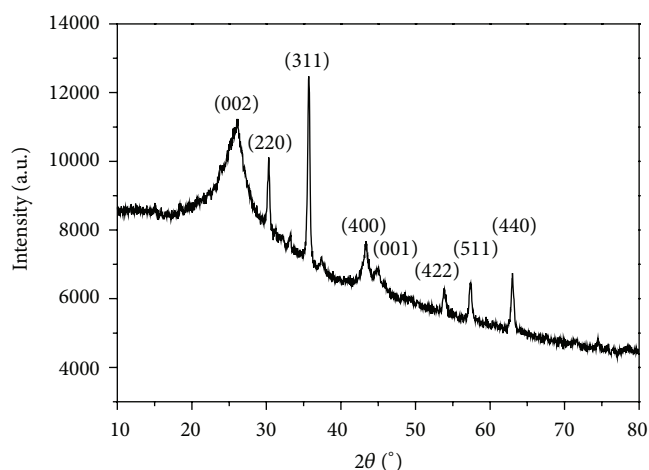


FIGURE 2: XRD patterns of the as-obtained carbonized PAN fiber.

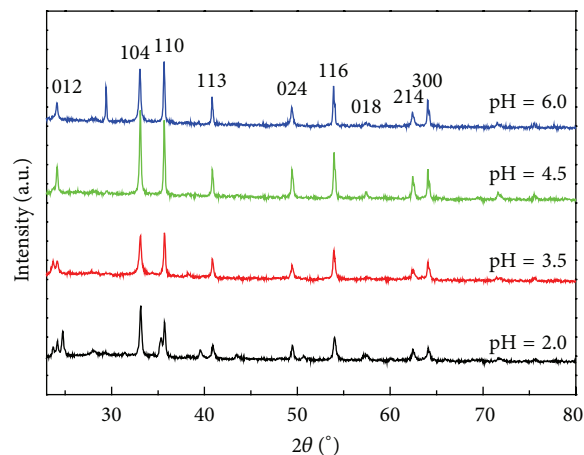


FIGURE 3: XRD patterns of as-obtained Fe_2O_3 -CNFs as the function of pH value.

ferric nitrate. After stirring at room temperature for 6 h, the above precursor solution was transferred into the injection syringe for electrospinning. The positive voltage applied to the needle tip was 25 kV and the distance between the needle tip and aluminum foil as the collector was 14 cm. The as-spun PAN fibers were first stabilized in an air environment at 260°C for 0.5 h and then carbonized in a nitrogen atmosphere at 800°C for 2 h (heating rate of $10^\circ\text{C}\cdot\text{min}^{-1}$).

2.2. Preparation of Fe_2O_3 -CNFs Nanostructures. 0.01 g of the obtained CNFs was put into 50 mL of 0.015 M $\text{K}_3[\text{Fe}(\text{CN})_6]$ solution and dispersed by ultrasound for 30 min. 0.1 M HCl or 0.1 M NaOH solution was dropped into the mixture to adjust the pH value. The obtained mixture was transferred into a 100 mL Teflon-lined stainless steel autoclave, sealed, and maintained at 140°C for different hours and then cooled to room temperature. The as-obtained products were collected, washed several times with distilled water, and then dried at 70°C for 24 h.

2.3. Characterization. The X-ray diffraction (XRD) patterns were recorded by a Panalytical X'pert Pro X-ray diffractometer equipped with CuK α irradiation at a scan rate of 0.02°s^{-1} .

The accelerating voltage and the applied current were 40 kV and 40 mA, respectively. The morphology of the samples was determined by field emission scanning electron microscope (SEM, JEOL JSM-6700F). The UV-Vis absorption spectra were measured by a HITACHI UV4100 spectrometer, with the scanning range from 300 nm to 800 nm.

2.4. Photocatalytic Activity. Photocatalytic reaction was carried out in a side-irradiation Pyrex cell at atmospheric pressure and room temperature. The effective irradiation area for the cell is 12.56 cm^2 . 0.05 g of photocatalyst powder was dispersed by a stirrer in 100 mL aqueous solution containing $10\text{ mg}\cdot\text{l}^{-1}$ MO. The dispersions were sonicated for 60 s and then magnetically stirred in the dark for ca. 15 min to ensure the establishment of adsorption/desorption equilibrium. The photocatalysts were irradiated with visible light through a cutoff filter ($\lambda > 420\text{ nm}$) from a 300 W Xe lamp. At a given irradiation time interval, aliquots of 5 mL of the solution were drawn and centrifuged. Subsequently the concentrations of MO in the filtrates were measured quantitatively through the UV-Vis spectrophotometer.

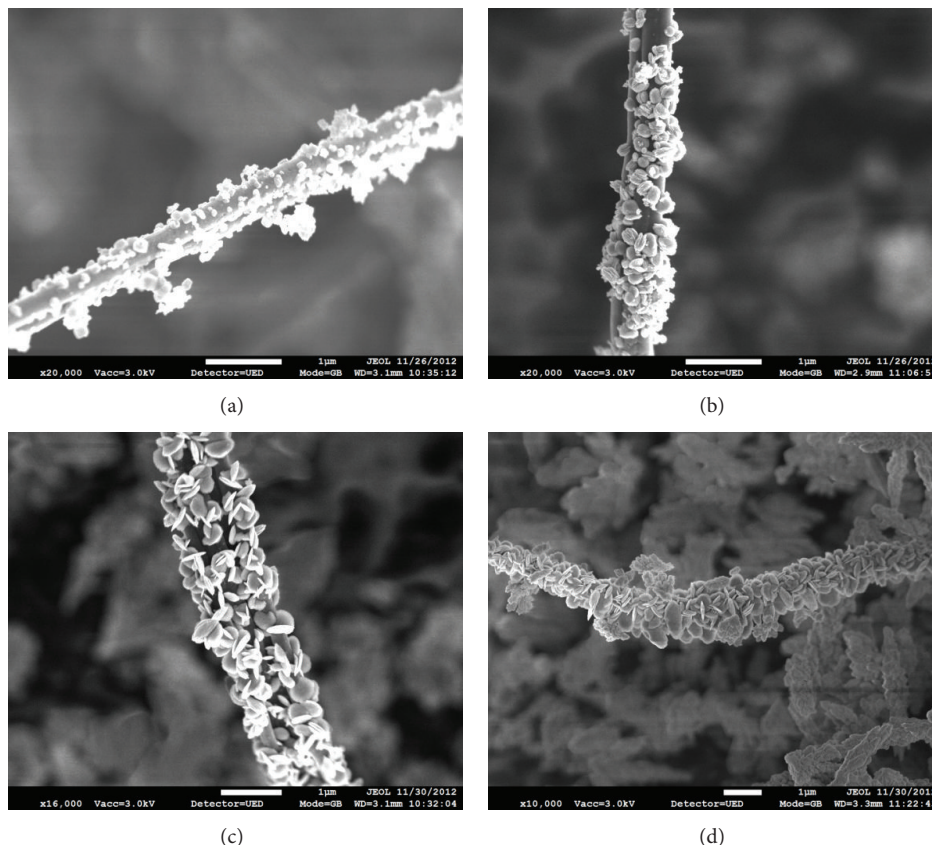


FIGURE 4: SEM images of as-obtained Fe_2O_3 -CNFs as the function of pH value: (a) 2.0, (b) 3.5, (c) 4.5, and (d) 6.0.

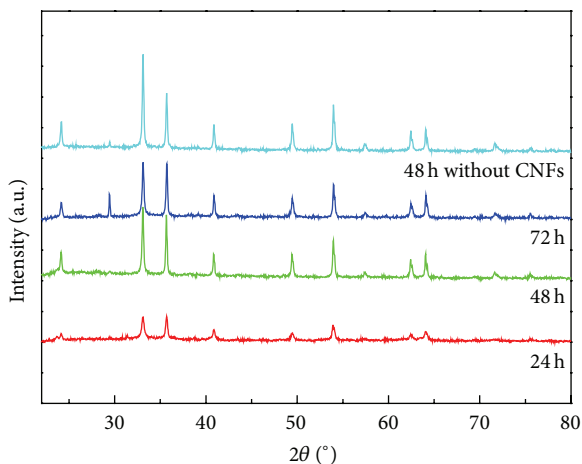


FIGURE 5: XRD patterns of as-obtained Fe_2O_3 -CNFs as the function of hydrothermal time.

3. Results and Discussion

Figure 1 shows the SEM images of the carbonized PAN fiber. From Figure 1(a), it can be seen that CNFs align in random orientation because of the bending instability associated with the spinning jet. Figure 1(b) displays the corresponding SEM image with higher magnification. It is

shown that these randomly oriented CNFs have a uniform surface with small particles and pores because of the outflow of the Fe_2O_3 particle and small molecule compound during the stabilization and carbonization [18]. The diameter of the CNFs ranges from 300 nm to 500 nm.

The XRD pattern of the as-obtained carbonized PAN fiber is shown in Figure 2. The broad peaks centered at around 26.2° and 43.7° are attributed to the (002) and (010) planes of the graphite carbon structure (JCPDS 41-1487) [19]. The fact that 002 diffraction peaks are relatively low in intensity and broad in shape suggests that as-prepared carbon nanofibers possess low graphitization and crystallization. Also, the broadening of the graphite peaks indicates the existence of some disordered structures in the products. Peaks at 30.3° , 35.7° , 43.3° , 53.8° , 57.4° , and 63.0° , which are corresponding to the diffraction peaks of $\gamma\text{-Fe}_2\text{O}_3$ (JCPDS 25-1402), suggest that nanoparticles are single phase with tetragonal structure [20]. Then these CNFs are exploited to produce Fe_2O_3 -CNFs by hydrothermal method.

To investigate the crystal structure of samples obtained from the hydrothermal process, XRD is also performed and the results are shown in Figure 3. The apparent peaks at 24.0° , 33.1° , 35.6° , 40.1° , 49.3° , 53.9° , 57.5° , 62.5° , and 64.0° correspond to the crystal plane of (012), (104), (110), (113), (024), (116), (214), and (300), which confirms the formation of single phase of $\alpha\text{-Fe}_2\text{O}_3$ with hexagonal structure (JCPDS 86-0550) [21]. When the pH value is adjusted from 2.0 to 4.5

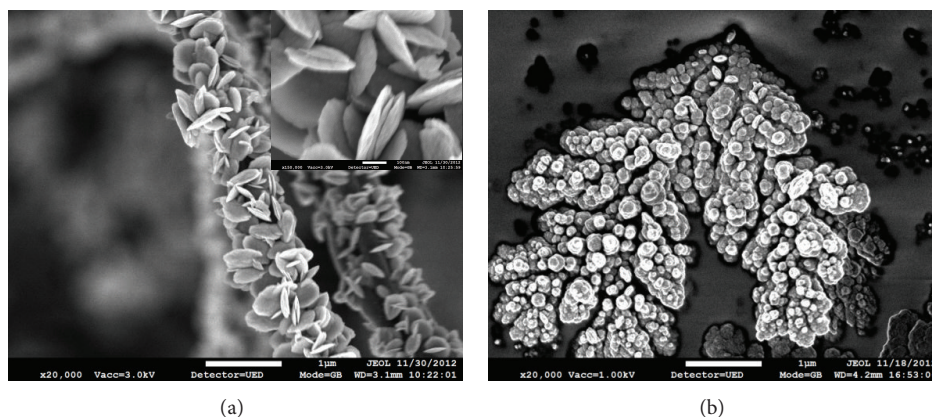


FIGURE 6: SEM images of (a) as-obtained Fe_2O_3 -CNFs (inset is the high magnification of (a)) and (b) Fe_2O_3 without CNFs.

by addition of HCl solution, the peaks belonging to α - Fe_2O_3 phase become sharper and stronger, which indicates that the pH value has a notable effect on the degree of crystallinity. With pH value increasing to 6.0, no significant change for the α - Fe_2O_3 structure is observed. But there appears to be a peak at 30.3 attributed to γ - Fe_2O_3 , indicating another phase is formed.

The morphology of the samples obtained from the hydrothermal process as the function of pH value is shown in Figure 4. Obviously, Fe_2O_3 particles have grown on the surface of CNFs and the pH value also has influenced the morphology of Fe_2O_3 particle. At lower pH value, CNFs are coated by the spherical particles that are unevenly distributed. This supports that there are small peaks belonging to carbon at (002) and (010) planes in Figure 3. When pH value increases to 4.5, flaky-shaped particle appears. It may suggest that the intensity of Fe_2O_3 at (110) plane becomes high as seen in Figure 3. From Figure 4(d), we can see that the flaky structure is broken and the as-obtained samples are not uniform in shape at pH value of 6.0. As discussed above, it seems that Fe_2O_3 -flaky coated CNFs with good crystallinity can be prepared at pH value of 4.5.

The effect of hydrothermal time on the crystalline structures of Fe_2O_3 -CNFs is investigated and the result is shown in Figure 5. As shown in Figure 5, The diffraction peaks of Fe_2O_3 , prepared by hydrothermal-treating 48 h, match well with those of pure α - Fe_2O_3 , and the intensity of peaks is higher and sharper than that of samples prepared by hydrothermal-treating 72 h and 24 h. When hydrothermal time increases to 72 h, other peaks appear in the XRD patterns which imply the production of impurity phase. Then the best reaction time would be 48 h. In order to compare, Fe_2O_3 powder without CNFs is prepared under the same condition which is the same as the Fe_2O_3 -CNFs. From Figure 5, it is found that the same α - Fe_2O_3 is obtained. However, the intensity of (104) and (110) peaks for Fe_2O_3 with or without CNFs is different, which implies that CNFs cause the crystal orientation of Fe_2O_3 . Then the corresponding morphology is shown in Figure 6. Obviously, the morphology of Fe_2O_3 is notably affected by adding CNFs. The Fe_2O_3 obtained

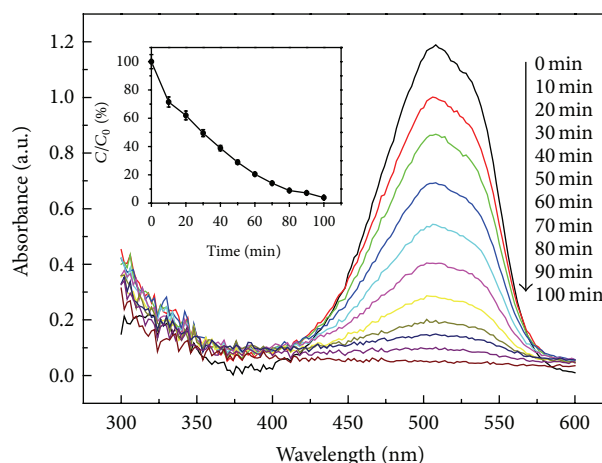


FIGURE 7: Absorption spectra of the solution of MO exposed to irradiation for different time (inset is degradation of MO under visible-light irradiation).

with CNFs has the regular and complete flaky morphology as shown in Figure 6(a). The as-obtained Fe_2O_3 without CNFs is composed of spherical particles and the particles are aggregated as shown in Figure 6(b). This can explain the strong intensity of (110) peaks in XRD patterns. In addition, from Figure 6(a), we can see that the diameter of flakes is about 300 nm. The difference observed in the morphology can be corrected by the XRD pattern.

The photocatalytic activity of as-obtained Fe_2O_3 -CNFs prepared under the optimal parameters of pH 4.5 and hydrothermal time of 48 h is evaluated in terms of degradation of MO under irradiation of visible light and the results are shown in Figure 7. It is seen that the intensity of the characteristic adsorption peak of MO solution decreases dramatically in 70 min. Moreover, with the extension of irradiation time, the peak intensity gradually decreases and completely disappears with 100 min irradiation. It reveals that Fe_2O_3 -CNFs have an excellent catalytic activity.

4. Conclusion

The α -Fe₂O₃-flaky coated carbon fibers were easily produced by the electrospinning process followed by a hydrothermal technique. The α -Fe₂O₃ flakes with single phase were successfully grown on the CNFs substrates, and the coverage of α -Fe₂O₃ flakes could be controlled by simply adjusting the hydrothermal pH value and time. The optimal parameters for hexagonal α -Fe₂O₃ preparation were pH of 4.5 and hydrothermal time of 48 h. The as-obtained α -Fe₂O₃-CNFs displayed high photocatalytic activity toward degradation of MO under visible-light irradiation. This synthetic method may be promisingly applied in fabricating other bi-multi-functional composites.

Conflict of Interests

The authors declare that there is no conflict of interests regarding the publication of this paper.

Acknowledgments

This work was supported by the Natural Science Foundation of China (NSFC) (nos. 21206133 and 21206134), doctoral program of Chinese Universities (20110201120042), and the National Natural Science Foundation of China, no. 50821064.

References

- [1] X. B. Chen, S. H. Shen, L. J. Guo, and S. S. Mao, "Semiconductor-based photocatalytic hydrogen generation," *Chemical Reviews*, vol. 110, no. 11, pp. 6503–6570, 2010.
- [2] H. Tong, S. X. Ouyang, Y. P. Bi, N. Umezawa, M. Oshikiri, and J. H. Ye, "Nano-photocatalytic materials: possibilities and challenges," *Advanced Materials*, vol. 24, no. 2, pp. 229–251, 2012.
- [3] M. D. Hernández-Alonso, F. Fresno, S. Suárez, and J. M. Coronado, "Development of alternative photocatalysts to TiO₂: challenges and opportunities," *Energy and Environmental Science*, vol. 2, no. 12, pp. 1231–1257, 2009.
- [4] J. Mao, K. Li, and T. Y. Peng, "Recent advances in the photocatalytic CO₂ reduction over semiconductors," *Catalysis Science & Technology*, vol. 3, pp. 2481–2498, 2013.
- [5] J. Gong, K. Yao, J. Liu et al., "Striking influence of Fe₂O₃ on the "catalytic carbonization" of chlorinated poly(vinyl chloride) into carbon microspheres with high performance in the photo-degradation of Congo red," *Journal of Materials Chemistry A*, vol. 1, no. 17, pp. 5247–5255, 2013.
- [6] D. Chatterjee and S. Dasgupta, "Visible light induced photocatalytic degradation of organic pollutants," *Journal of Photochemistry and Photobiology C: Photochemistry Reviews*, vol. 6, no. 2-3, pp. 186–205, 2005.
- [7] Q.-Y. Chen, J.-S. Liu, Y. Liu, and Y.-H. Wang, "Hydrogen production on TiO₂ nanorod arrays cathode coupling with bio-anode with additional electricity generation," *Journal of Power Sources*, vol. 238, pp. 345–349, 2013.
- [8] F. L. Zhou, X. J. Li, J. Shu, and J. Wang, "Synthesis and visible light photo-electrochemical behaviors of In₂O₃-sensitized ZnO nanowire array film," *Journal of Photochemistry and Photobiology A: Chemistry*, vol. 219, no. 1, pp. 132–138, 2011.
- [9] Z. F. Bian, J. Zhu, S. H. Wang, Y. Cao, X. F. Qian, and H. X. Li, "Self-assembly of active Bi₂O₃/TiO₂ visible photocatalyst with ordered mesoporous structure and highly crystallized anatase," *Journal of Physical Chemistry C*, vol. 112, no. 16, pp. 6258–6262, 2008.
- [10] G. Liu, Q. Deng, H. Wang et al., "Micro/nanostructured α -Fe₂O₃ spheres: synthesis, characterization, and structurally enhanced visible-light photocatalytic activity," *Journal of Materials Chemistry*, vol. 22, no. 19, pp. 9704–9713, 2012.
- [11] Y. Shi, H. Y. Li, L. Wang, W. Shen, and H. Z. Chen, "Novel α -Fe₂O₃/CdS cornlike nanorods with enhanced photocatalytic performance," *ACS Applied Materials and Interfaces*, vol. 4, no. 9, pp. 4800–4806, 2012.
- [12] L. MacHala, J. Tuček, and R. Zbořil, "Polymorphous transformations of nanometric iron(III) oxide: a review," *Chemistry of Materials*, vol. 23, no. 14, pp. 3255–3272, 2011.
- [13] S. Kedem, D. Rozen, Y. Cohen, and Y. Paz, "Enhanced stability effect in composite polymeric nanofibers containing titanium dioxide and carbon nanotubes," *Journal of Physical Chemistry C*, vol. 113, no. 33, pp. 14893–14899, 2009.
- [14] H. Yu, X. Quan, S. Chen, and H. Zhao, "TiO₂-multiwalled carbon nanotube heterojunction arrays and their charge separation capability," *Journal of Physical Chemistry C*, vol. 111, no. 35, pp. 12987–12991, 2007.
- [15] J. B. Mu, C. L. Shao, Z. C. Guo et al., "High photocatalytic activity of ZnO-carbon nanofiber heteroarchitectures," *ACS Applied Materials and Interfaces*, vol. 3, no. 2, pp. 590–596, 2011.
- [16] J. Liu, J. Li, A. Sedhain, J. Lin, and H. Jiang, "Structure and photoluminescence study of TiO₂ nanoneedle texture along vertically aligned carbon nanofiber arrays," *Journal of Physical Chemistry C*, vol. 112, no. 44, pp. 17127–17132, 2008.
- [17] H. E. Unalan, D. Wei, K. Suzuki et al., "Photoelectrochemical cell using dye sensitized zinc oxide nanowires grown on carbon fibers," *Applied Physics Letters*, vol. 93, no. 13, Article ID 133116, 2008.
- [18] L. W. Ji, O. Toprakci, M. Alcoutlabi et al., " α -Fe₂O₃ nanoparticle-loaded carbon nanofibers as stable and high-capacity anodes for rechargeable lithium-ion batteries," *ACS Applied Materials and Interfaces*, vol. 4, no. 5, pp. 2672–2679, 2012.
- [19] Y. L. Luo, Q. Y. Chen, D. Zhu, and M. Matsuo, "Graphite carbon foam films prepared from porous polyimide with in situ formed catalytic nickel particles," *Journal of Applied Polymer Science*, vol. 116, no. 4, pp. 2110–2118, 2010.
- [20] S.-Z. Guo, Y. Li, J.-S. Jiang, and H.-Q. Xie, "Nanofluids containing γ -Fe₂O₃ nanoparticles and their heat transfer enhancements," *Nanoscale Research Letters*, vol. 5, no. 7, pp. 1222–1227, 2010.
- [21] L. X. Yang, Y. Liang, H. Chen, L. Y. Kong, and W. Jiang, "Facile hydrothermal route to the controlled synthesis of α -Fe₂O₃ 1-D nanostructures," *Bulletin of Materials Science*, vol. 31, no. 7, pp. 919–923, 2008.

Research Article

Diffusion-Controlled Growth of Oxygen Bubble Evolved from Nanorod-Array TiO₂ Photoelectrode

Xiaowei Hu, Yechun Wang, Liejin Guo, and Zhenshan Cao

State Key Laboratory of Multiphase Flow in Power Engineering, International Research Center for Renewable Energy, Xi'an Jiaotong University, Shaanxi 710049, China

Correspondence should be addressed to Xiaowei Hu; hu-xiaowei@mail.xjtu.edu.cn and Liejin Guo; lj-guo@mail.xjtu.edu.cn

Received 28 March 2014; Accepted 8 May 2014; Published 25 May 2014

Academic Editor: Haimin Zhang

Copyright © 2014 Xiaowei Hu et al. This is an open access article distributed under the Creative Commons Attribution License, which permits unrestricted use, distribution, and reproduction in any medium, provided the original work is properly cited.

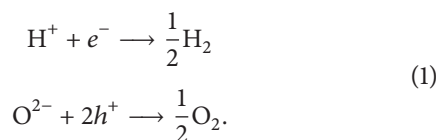
Nanorod-array structure gains its popularity in photoelectrode design for water splitting. However, the structure's effects on solid-liquid interface interaction and reaction product transportation still remain unsolved. Gas bubble generally evolved from photoelectrodes, which provides a starting point for the problem-solving. Based on this, investigations on the gas-evolving photoelectrode are carried out in this paper. By experimental studies of wettability on the photoelectrode nanorod-array surface and oxygen bubble growth from anode, we analyzed the interaction affecting the gas-solid-liquid contact behaviors and product transportation mechanism, which is controlled by diffusion due to the concentration gradient of dissolved gases in the aqueous electrolyte and the microconvection caused by the bubble interface movement. In the end, based on the bubble growth characteristics of $R_B(t) \sim t^{0.5}$ in the experiment, a model describing the product transport mechanism was presented.

1. Introduction

Hydrogen production by photoelectrochemical water splitting is a promising source for carbon-free energy [1–3]. In order to increase the energy conversion efficiency, a lot of research on transfer process enhancement of photo-electron has been carried out with great progress by photoelectrode surface modification with special micro-nano structure [4–7]. But for this kind of heterogeneous photocatalytic or photochemical conversion system, many issues concerning interface of such micro-nano structure semiconductor and liquid still remain unsolved, such as the nature of the active sites, mechanism for heterogeneous photocatalytic reaction of water splitting, and effects of interfacial interaction during reaction product transfer.

Much research has been focused on photon-electron transfer movement and enhancement from solid inside to the solid surface, but the principle how the electrons transferring to the surface interact with the water is underinvestigated. Actually, solid surface with roughness or special structures can highly influence the interaction between water and solid surface which is indicated by the parameter of contact

angle [8] and will highly influence the surface photocatalytic reaction as follows:



On the other hand, hydrogen/oxygen bubble evolution from photoelectrode is a typical interfacial phenomenon controlled by the interfacial interactions and mass-transfer process in the three-phase zone where gas bubble, electrolyte, and electrode surface contact each other, leading to requirement for understanding the bubble evolution process during photocatalysis especially for photoelectrode with micro-nano structure surface. Analogy to water electrolysis, it is believed the bubble evolution process includes the generation of the dissolved gas in molecular form by electrochemical reactions, the accumulation of the dissolved gas molecules around the electrode surface to form the supersaturation layer, bubble nucleation, growth, and detachment on surface active sites. For the bubble growth process, the existence

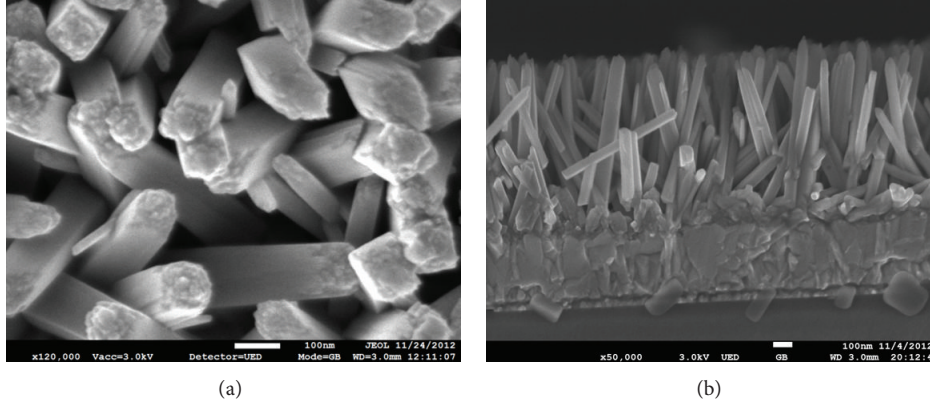


FIGURE 1: Nanorod-array structure TiO_2 film.

of two characteristic regimes for the increase of the bubble radius $R_B(t)$ on time could be expected. In the first stage, which is difficult to observe, a fast inertia-controlled growth takes place. The resulting reduction of the gas available amount leads to the second regime, diffusion-controlled growth according to $R_B(t) \sim t^x$. Generally, the x is considered to be 0.5 as described by Scriven's theory [9]. But if the ratio between photoelectrode size and bubble diameter is small enough to make the gas produced probably directly inject into the bubble, by virtue of the steep concentration gradients at the foot of the bubble, the x is equal to 0.3 [10, 11]. During these two growth regimes, the effects of diffusion caused by the presence of the supersaturation layer and microconvection due to bubble play an important role, which is owed to the concentration gradient of dissolved gases in the aqueous electrolyte called as single-phase free convection, and interface movement between gas and liquid on electrode surface once the bubble is nucleated, respectively [12, 13].

Although much progress has been made on the bubble growth, effects of the solid surface structure are still to be understood. Wei et al. investigated the bubble behavior on micro-pin-fined surface and considered a large capillary force leading to easy bubble detachment [14]. Yang et al. studied the bubble-solid interaction indicating the importance of electrolyte concentration and DLVO surface forces [15]. The interaction between the micro-nano structure surface with electrolyte and gas-liquid interface should be investigated more deeply.

In this paper, to investigate nanostructure effects on bubble behavior evolved from nanoscale structure photoelectrode, a study on nanorod-array structure surface characteristics and single oxygen bubble growth dynamics is carried out.

2. Experimental

TiO_2 film modified by nanorod-array was used as the anode in the investigation, and its SEM shows in Figure 1 with rod height of about 870 nm and rod diameter of nearly 120 nm.

The optical contact angle meter model SL200 was applied to study the wettability of its surface.

The experiments on bubble evolution were conducted in an electrolytic cell, as shown in Figure 2. Na_2SO_4 in deionized water with different concentrations of 0.495, 0.354, 0.261, 0.206, and 0.170 mol/L was used as the electrolyte. Pt was used as a cathode. The bubble evolution process was observed by the microscope camera system. The image intense CCD whose resolution is 1376×1040 and objective lens is $5\times/0.15$ was applied. All the experiments were conducted under the conditions of ambient temperature 25°C and ambient pressure 1 atm.

3. Results and Discussion

3.1. Wettability of Nanorod-Array TiO_2 Film. In order to investigate the interaction, especially wettability between nanorod-array film and water, we carry out the experiment on contact angle firstly. Figure 3 shows measurement results of about $80^\circ \pm 1^\circ$, indicating a general hydrophilic ability.

3.2. Oxygen Bubble Behavior Evolved from Nanorod-Array TiO_2 Film. Figure 4 shows the general characteristics of bubble growth. Compared to bubble growth during boiling and common electrolysis, bubble evolved from nanorod-array surface stays longer and smaller, which is determined by the forces acting on them. In our experiment, the proper effects include gravity, gas-liquid interfacial surface tension, marangoni force, electric force (with the possibility of gas-liquid interface being charged), and interfacial interaction with elastic materials. Among those, the most possible and important effects to prevent the bubble departure and keep bubble staying are marangoni force due to nonhomogeneous gas adsorption at the interface and the capillary force caused by contact behavior with nanorod-array surface structure.

Besides the dynamics aspect, we are much concerned about the mechanism driving the bubble growth. We investigate the relationship of $R_B(t) \sim t^x$, as show in Figure 5. It indicates the $R_B(t)^2$ is linear to the time, which is to say $x = 0.5$ for equation $R_B(t) \sim t^x$.

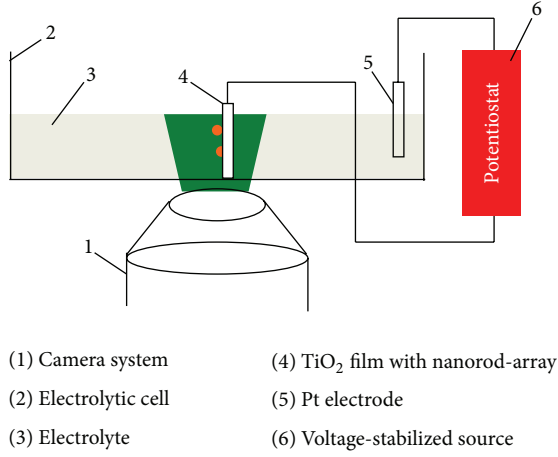
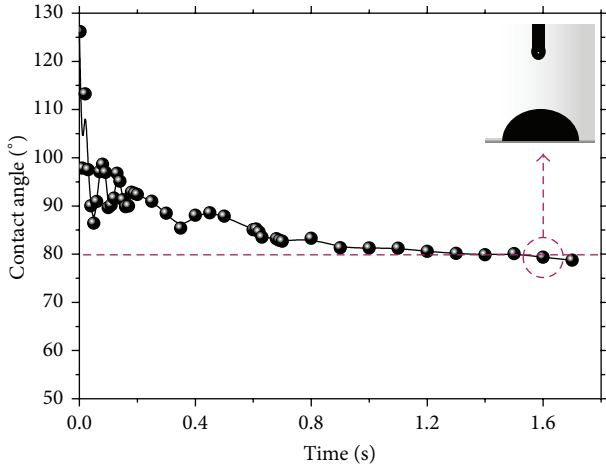
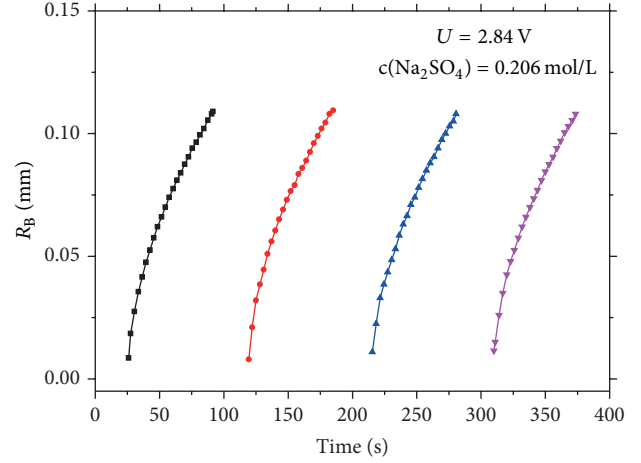
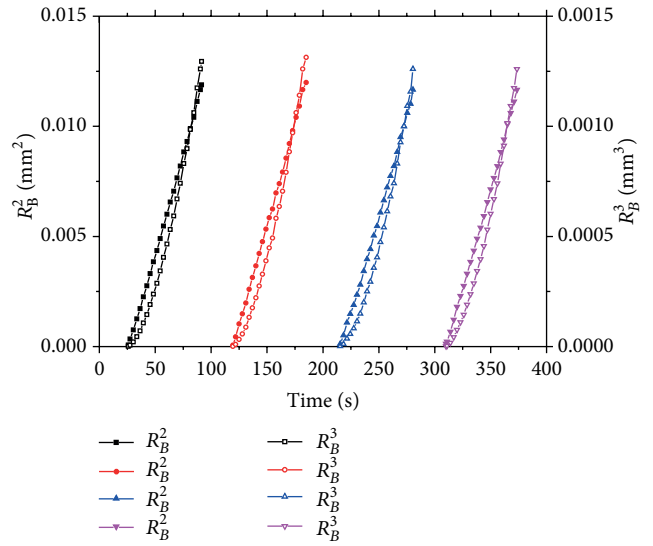


FIGURE 2: Schematic of the experiment setup.


 FIGURE 3: Contact angle measurement results of nanorod-array TiO₂ film and water.

3.3. Oxygen Bubble Growth Model from Nanorod-Array TiO₂ Film. The bubble growth is driven by the concentration difference between the electrolyte bulk and the bubble interface, which is an analogy to the bubble growth during boiling. But the acquisition of the concentration data, key to electrolysis, is much difficult than that of the temperature data for boiling. So the modelling of bubble growth driven by the concentration difference is less developed than that driven by the temperature difference.

From the above analysis, we obtained $R_B(t) \sim t^{0.5}$ relationship, which is first growth mechanism showed in Figure 6. According to Vogt's theory [12, 13], effects on bubble growth in one circle, meaning the process of bubble departure and movement excluded, include two parts, which are the diffusion due to the concentration gradient of dissolved gases in the aqueous electrolyte and the microconvection caused by the bubble interface movement.


 FIGURE 4: Bubble growth characteristics under $U = 2.84 \text{ V}$ and $c(\text{Na}_2\text{SO}_4) = 0.206 \text{ mol/L}$ (colorful lines stand for different growth periods).

 FIGURE 5: The relationship between bubble radius and time under $U = 2.84 \text{ V}$ and $c(\text{Na}_2\text{SO}_4) = 0.206 \text{ mol/L}$ (colorful lines stand for different growth periods).

For the diffusion effect, we can describe it by the following mass transfer around the bubble, assuming a steady state:

$$\frac{d^2c}{dr^2} + \frac{2}{r} \frac{dc}{dr} = 0. \quad (2)$$

And the boundary conditions are as follows:

$$r = R_B, \quad c = c_i; \quad r = \infty, \quad c = c_0. \quad (3)$$

And then, we can solve the equation, obtaining concentration distribution as follows:

$$c = c_0 - \frac{R_B}{r} (c_0 - c_i). \quad (4)$$

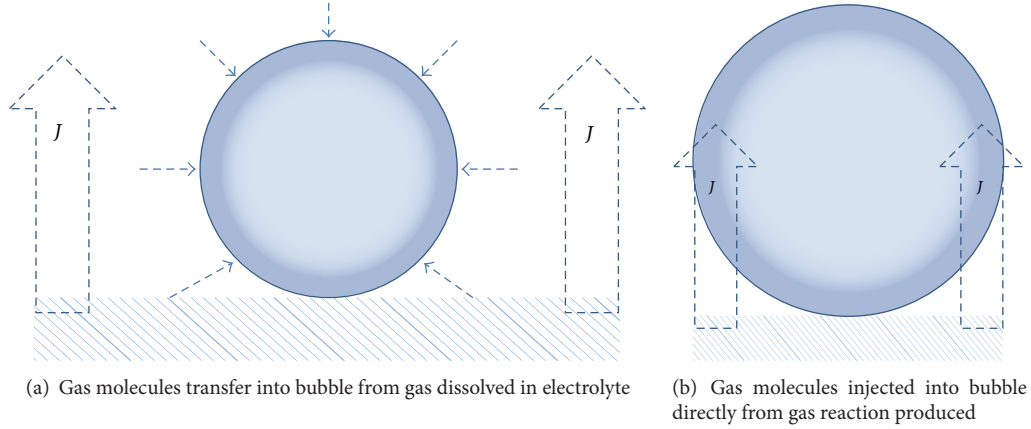


FIGURE 6: Bubble growth mechanisms.

So diffusion flow of the gas transferred across the bubble interface can be described as

$$J_1 = 4\pi R_B^2 D_{O_2} \left. \frac{\partial c}{\partial r} \right|_{r=R_B} = 4\pi R_B D_{O_2} (c_0 - c_i), \quad (5)$$

where D_{O_2} is the diffusion coefficient of oxygen gas.

For the microconvection effect caused by the bubble interface movement, we refer to the surface renewal theory by Danckwerts [16] described as follows:

$$J_2 = 4\pi R_B^2 \sqrt{S D_{O_2}} (c_0 - c_i), \quad (6)$$

where S is ratio of the increasing surface area to the total surface area,

$$S = \frac{d(4\pi R_B^2)/dt}{4\pi R_B^2} = \frac{2}{R_B} \frac{dR_B}{dt}. \quad (7)$$

So the total mass-transfer flow into a bubble is

$$J = J_1 + J_2 = 4\pi R_B^2 D_{O_2} \left(\frac{1}{R_B} + \sqrt{\frac{2}{R_B D_{O_2}} \frac{dR_B}{dt}} \right) (c_0 - c_i). \quad (8)$$

On the other hand, from the aspect of mass conservation, the net mass-transfer flow is equal to the gas molecules variation in the bubble, which is

$$J = \frac{d}{dt} \left(\frac{V_B}{V_{mol}} \right) = \frac{d}{dt} \left(\frac{4\pi R_B^3}{3V_{mol}} \right). \quad (9)$$

And then, we obtain

$$\frac{dR_B}{dt} = V_{mol} D_{O_2} (c_0 - c_i) \left(\frac{1}{R_B} + \sqrt{\frac{2}{R_B D_{O_2}} \frac{dR_B}{dt}} \right). \quad (10)$$

Letting $R_B = Bt^{0.5}$ according to our experimental results and substituting it to (10), we conclude that

$$B = \sqrt{D_{O_2}} \left(A + \sqrt{A^2 + 2A} \right), \quad (11)$$

where $A = V_{mol}(c_0 - c_i)$.

So the bubble radius is

$$R_B = \left(A + \sqrt{A^2 + 2A} \right) \sqrt{D_{O_2}} (t)^{1/2}. \quad (12)$$

Equation (12), as the bubble growth model, can describe the diffusion-controlled bubble growth process including diffusion and microconvection effects.

4. Conclusions

In this paper, we carried out research on nanorod-array structure surface characteristics and single oxygen bubble growth dynamics. By experimental studies of wettability on the photoelectrode nanorod-array surface and oxygen bubble growth from anode, we analyzed the interaction affecting the gas-solid-liquid contact behaviors and product transportation mechanism, which is controlled by diffusion due to the concentration gradient of dissolved gases in the aqueous electrolyte and the microconvection caused by the bubble interface movement and we emphasize the importance of marangoni force due to nonhomogeneous gas adsorption at the interface and the capillary force caused by contact behavior with nanorod-array surface structure on bubble growth period. In the end, based on the bubble growth characteristics of $R_B(t) \sim t^{0.5}$ in the experiment, a model describing the product transport mechanism was presented.

Abbreviations

- R_B : Bubble radius, m
- c_i : Concentration at interface, mol/L
- c_0 : Concentration in bulk liquid, mol/L
- D_{O_2} : Diffusion coefficient of oxygen gas, m²/s
- J : Mass-transfer rate, mol/s
- V_{mol} : Molar volume, m³/mol
- V_B : Bubble volume, m³.

Conflict of Interests

The authors declare no conflict of interests.

Acknowledgments

The authors gratefully acknowledge the financial support of the National Natural Science Foundation of China (no. 51306147, no. 51236007, no. 51323011, and no. 51102194) and China Postdoctoral Science Foundation (no. 2013M532043). One of the authors (Xiaowei Hu) was supported by the “Fundamental Research Funds for the Central Universities.” And the authors sincerely thank Dr. J. Su for helpful discussions.

References

- [1] A. B. Murphy, P. R. F. Barnes, L. K. Randeniya et al., “Efficiency of solar water splitting using semiconductor electrodes,” *International Journal of Hydrogen Energy*, vol. 31, no. 14, pp. 1999–2017, 2006.
- [2] J. Turner, G. Sverdrup, M. K. Mann et al., “Renewable hydrogen production,” *International Journal of Energy Research*, vol. 32, no. 5, pp. 379–407, 2008.
- [3] M. G. Walter, E. L. Warren, J. R. McKone et al., “Solar water splitting cells,” *Chemical Reviews*, vol. 110, no. 11, pp. 6446–6473, 2010.
- [4] G. M. Wang, H. Y. Wang, Y. C. Ling et al., “Hydrogen-treated TiO₂ nanowire arrays for photoelectrochemical water splitting,” *Nano Letters*, vol. 11, no. 7, pp. 3026–3033, 2011.
- [5] F. E. Osterloh, “Inorganic nanostructures for photoelectrochemical and photocatalytic water splitting,” *Chemical Society Reviews*, vol. 42, no. 6, pp. 2294–2320, 2013.
- [6] Z. S. Li, W. J. Luo, M. L. Zhang, J. Y. Feng, and Z. G. Zou, “Photoelectrochemical cells for solar hydrogen production: current state of promising photoelectrodes, methods to improve their properties, and outlook,” *Energy & Environmental Science*, vol. 6, no. 2, pp. 347–370, 2013.
- [7] M. T. Mayer, Y. J. Lin, G. B. Yuan, and D. W. Wang, “Forming heterojunctions at the nanoscale for improved photoelectrochemical water splitting by semiconductor materials: case studies on hematite,” *Accounts of Chemical Research*, vol. 46, no. 7, pp. 1558–1566, 2013.
- [8] M. A. Henderson, “The interaction of water with solid surfaces: fundamental aspects revisited,” *Surface Science Reports*, vol. 46, no. 1–8, pp. 1–308, 2002.
- [9] L. E. Scriven, “On the dynamics of phase growth,” *Chemical Engineering Science*, vol. 10, no. 1–2, pp. 1–13, 1959.
- [10] N. P. Brandon and G. H. Kelsall, “Growth-kinetics of bubbles electrogenerated at microelectrodes,” *Journal of Applied Electrochemistry*, vol. 15, no. 4, pp. 475–484, 1985.
- [11] D. Fernandez, M. Martine, A. Meagher, M. E. Mobius, and J. M. D. Coey, “Stabilizing effect of a magnetic field on a gas bubble produced at a microelectrode,” *Electrochemistry Communications*, vol. 18, no. 1, pp. 28–32, 2012.
- [12] H. Vogt, “The role of single-phase free-convection in mass-transfer at gas evolving electrodes—I. Theoretical,” *Electrochimica Acta*, vol. 38, no. 10, pp. 1421–1426, 1993.
- [13] H. Vogt, “The role of single-phase free-convection in mass-transfer at gas evolving electrodes—II. Experimental-verification,” *Electrochimica Acta*, vol. 38, no. 10, pp. 1427–1431, 1993.
- [14] J. J. Wei, Y. F. Xue, J. F. Zhao, and J. Li, “Bubble behavior and heat transfer of nucleate pool boiling on micro-pin-finned surface in microgravity,” *Chinese Physics Letters*, vol. 28, no. 1, Article ID 016401, 2011.
- [15] C. Yang, T. Dabros, D. Q. Li, J. Czarnecki, and J. H. Masliyah, “Kinetics of microbubble—solid surface interaction and attachment,” *AIChE Journal*, vol. 49, no. 4, pp. 1024–1037, 2003.
- [16] P. Danckwerts, “Significance of liquid-film coefficients in gas absorption,” *Industrial & Engineering Chemistry*, vol. 43, no. 6, pp. 1460–1467, 1951.

Research Article

Effects of Absorber Emissivity on Thermal Performance of a Solar Cavity Receiver

Jiabin Fang, Nan Tu, and Jinjia Wei

State Key Laboratory of Multiphase Flow in Power Engineering, Xi'an Jiaotong University, Xi'an 710049, China

Correspondence should be addressed to Jinjia Wei; jjwei@mail.xjtu.edu.cn

Received 14 March 2014; Accepted 8 April 2014; Published 8 May 2014

Academic Editor: Shaohua Shen

Copyright © 2014 Jiabin Fang et al. This is an open access article distributed under the Creative Commons Attribution License, which permits unrestricted use, distribution, and reproduction in any medium, provided the original work is properly cited.

Solar cavity receiver is a key component to realize the light-heat conversion in tower-type solar power system. It usually has an aperture for concentrated sunlight coming in, and the heat loss is unavoidable because of this aperture. Generally, in order to improve the thermal efficiency, a layer of coating having high absorptivity for sunlight would be covered on the surface of the absorber tubes inside the cavity receiver. As a result, it is necessary to investigate the effects of the emissivity of absorber tubes on the thermal performance of the receiver. In the present work, the thermal performances of the receiver with different absorber emissivity were numerically simulated. The results showed that the thermal efficiency increases and the total heat loss decreases with increasing emissivity of absorber tubes. However, the thermal efficiency increases by only 1.6% when the emissivity of tubes varies from 0.2 to 0.8. Therefore, the change of absorber emissivity has slight effect on the thermal performance of the receiver. The reason for variation tendency of performance curves was also carefully analyzed. It was found that the temperature reduction of the cavity walls causes the decrease of the radiative heat loss and the convective heat loss.

1. Introduction

Tower-type solar power generation is widely adopted in the establishment of large-scale solar thermal power plants. With more and more demonstration systems running successfully, this power generation way has attracted a lot of attention all over the world and has a tendency to be one of mainstream high power generation ways. At the same time, the thermal efficiency of the whole solar power system is more and more seriously considered because of the considerable construction cost. Higher thermal efficiency means more power will be generated in the same time, which will decrease the average cost and improve the competitiveness. Among all the components in solar power system, solar receiver is a key one, which converts solar energy into thermal energy in tower-type system. One possible configuration usually used is the cavity receiver because of its large surface area and low heat loss. Ávila-Marín [1] regarded cavity receiver as the best alternative to tube receivers, which would become advanced technology for the deployment of new solar tower power plants. For a solar cavity receiver, there is an aperture on the front face of the cavity, through which sunlight

concentrated by a heliostat field projects onto the surfaces inside the receiver. Meanwhile, the existence of the aperture causes unavoidable heat loss. So the thermal efficiency and the heat loss are the important indicators for evaluating the thermal performance of a solar cavity receiver, and the study on the thermal performance also wins much attention from researchers. An analytical model of large cubical central receivers was proposed by Clausing [2], based on the assumption that two factors govern the convective heat loss: (i) the ability to transfer mass and energy across the aperture and (ii) the ability to heat air inside the cavity. The latter factor was found to be more important. This model was later refined and verified with experimental results and good agreement was found [3]. Juárez et al. [4] and Prakash et al. [5] gave a brief review on the natural convection in cavities. It revealed that many researchers have studied both experimentally and numerically the cavities with different boundary conditions in order to better understand the mechanism of heat loss. Moreover, the literature survey showed that most investigations on the heat loss of cavity are limited to the boundary conditions with isothermal and/or adiabatic surfaces. Paitoonsurikarn et al. [6] numerically investigated the natural

convective heat loss of four different open cavity receivers and validated the results with the experimental data. They found that the numerical and the experimental results agree well with each other. A new correlation was also presented for the natural convection based on the numerical results. This correlation proposes a new concept of an ensemble cavity length scale for considering the combined effect of cavity geometry and inclination. And the correlation has high accuracy compared with other ones. Taumofolau et al. [7] experimentally and numerically studied the relationship between the natural convective heat loss and the inclination angles of an open cavity receiver. Electrical heating was used as a heat source. It was found that the highest loss appears at 0° and the loss decreases as the inclination angle approaches 90° . They carried out the numerical simulation on the convective heat loss of the receiver with CFD. The numerical result shows good agreement with the experimental data. Le Quere et al. [8] investigated the heat loss from an isothermal cubic cavity for Rayleigh numbers $10^7 \leq Ra \leq 10^9$. The total heat loss was found to be strongly dependent on the cavity inclination and correlations for each inclination were established. Reynolds et al. [9] studied the steady-state computational analysis of trapezoidal cavity receiver. Experimental and computational studies of heat loss characteristics were carried out, and flow visualization technique was used to capture the flow patterns. CFD prediction of heat loss appears to be 40% less compared with experimental results, which should be caused by the uncertainties in the experimental work. Harris and Lenz [10] analyzed the thermal performance of five different geometries of cavity receivers (cylindrical, heteroconical, conical, spherical, and elliptical) and found that the deviation in rim angle of concentrator and the cavity geometry cause great variations on power profiles inside the cavity receiver. Reddy and Kumar [11, 12] presented a numerical study of transfer in a cavity receiver. A 2D simulation model and a 3D simulation model for combined natural convection and surface radiation were successively developed. The influence of operating temperature, emissivity of the surface, orientation, and geometries on the total heat loss of the receiver was investigated. The results showed that the convective heat loss of the modified receiver is significantly influenced by the inclination of the receiver whereas the radiative heat loss is considerably affected by surface properties. They also found that the 3D model can be used for accurate estimation of heat loss. Gonzalez et al. [13] numerically investigated the natural convection and the surface thermal radiation of an open cavity receiver considering large temperature differences and variable fluid properties. The numerical result indicated that, for large temperature differences between the hot wall and the bulk fluid, the radiative heat transfer is more important than the convection. Sharma et al. [14, 15] and Vivek et al. [16] studied conjugate natural convection and surface radiation in rectangular enclosures, inclined differentially heated enclosures, and air-filled tilted enclosures for a wide range of the tilt angle. They found that surface radiation weakens natural convection. However, the reduction in the convection effect is compensated by the contribution of radiation. A 2D numerical analysis of combined heat transfer (transient natural convection, surface thermal radiation, and

conduction) in an air-filled square enclosure was carried out by Martyushev and Sheremet [17]. It was found that the average convective Nusselt number increases with the Rayleigh number Ra and thermal conductivity ratio $k_{1,2}$, and it decreases with the surface emissivity ε and the ratio of solid wall thickness to cavity spacing L , while the average radiative Nusselt number increases with Ra and $k_{1,2}$, and it decreases with l/L . Wu et al. [18] conducted an experimental investigation using electrically heating method to explore the effects of surface boundary condition, tilt angle, and heat flux on heat loss of a fully open cylindrical cavity. It was concluded that temperatures of bottom surface fluctuate in a small region, and side surface temperatures decrease with increasing position departure from bottom surface. The natural convection heat loss is sensitive to the tilt angle in comparison with the radiation and conduction heat losses. In addition, the empirical correlations of the natural convection, radiation, and total heat loss Nusselt numbers versus the Grashof number, tilt angle, and ambient temperature were proposed. Hogan et al. [19] presented a numerical model for an axisymmetric solar cavity receiver. The results showed that the model is better for small-to-midsized apertures than for large ones. Both the total solar energy rate and the convective heat loss significantly affect the thermal performance of the receiver. And the distribution of input solar flux affects the temperature distribution a lot inside the receiver. Li et al. [20] established an easy-to-use global steady-state model for a cavity receiver. Each part of heat loss can be easily calculated by using this model. The elements, which influence the receiver thermal performance, including receiver area, surface emissivity, reflectivity, absorber tube number, and tube diameter, were all taken into account. They found that the receiver surface emissivity has little influence on the receiver efficiency. However, the surface reflectivity has strong influence on the receiver thermal performance. And low surface reflectivity can obtain high thermal performance of the receiver. Zhang et al. [21] proposed a transfer function method for testing the dynamic performance of a cavity receiver. They adopted this method to predict the outlet temperatures and compared the predicted results with the indoor transient experimental data. The result showed that the transfer function method can accurately predict the outlet temperature trends despite the fact that some errors exist between the predicted and the measured outlet temperatures. They also analyzed the fact that the errors may have originated from the changing flow rate. Baker et al. [22] introduced CESA-1 cavity receiver, which is a demonstration power station in Spain. In their report, receiver controls, locations based on analogic measurements, cold and warm receiver start-ups, and transient response to cloud-induced changes were mentioned when CESA-1 was in operation. In order to minimize start-up time, the appropriate operating strategies were implemented during CESA-1 receiver start-up. Fang et al. [23] proposed a combined calculation method for evaluating the thermal performance of the solar cavity receiver. With this method, the thermal performance of a solar cavity receiver, a saturated steam receiver, is simulated under different wind environments. The results indicated that changing the wind angle or velocity can obviously affect

the thermal performance of the receiver. And the heat loss reaches maximum under side-on wind condition. Based on this numerical model, the same authors [24] established a new model for calculating the thermal performance of the solar cavity receiver during start-up processes. The solar energy required by the aperture of the receiver was also obtained during start-up. The results showed that the thermal efficiency appears very low but sharply increases in the early stage of start-up. The convective heat loss is the main heat loss even at the end of start-up processes. Yu et al. [25] presented two models, respectively, for the collector and cavity receiver. The two models were coupled together to simulate and design the solar power system. They [26] also proposed an integrated receiver model for full range operation conditions in order to simulate and evaluate the dynamic characteristics of a solar cavity receiver. Based on this model, the dynamic characteristics of the solar cavity receiver were tested and also they calculated the thermal loss with different wind conditions. Montes et al. [27] analyzed a new optimized heat transfer model in the absorber surface of a thermofluid dynamic design of a solar central receiver. The fluid flow scheme designed can present lower temperature difference between side tubes in the same pass and higher uniform outlet temperature of all circuits. As we know, when sunlight passes through the atmosphere, solar radiation is weakened due to the absorption of the gas. The extinction effect of the ozone on ultraviolet lights is particularly strong, while vapor and CO₂ mainly absorb infrared lights. Therefore, for solar radiation reaching the earth's surface, about 95% of the energy is concentrated in the wavelength range of 0.2–2 μm [28]. However, for infrared energy radiated by the cavity receiver, the energy proportion reaches up to 99% in the wavelength range larger than 2 μm, because the wall temperature of cavity receiver is only about hundreds of degrees. Thus the absorption of the receiver for sunlight (0.2–2 μm) on the earth surface and infrared light (larger than 2 μm) radiated by cavity walls is distinguished in the present study. In Kesselring's [29] book, the absorber tubes inside a cavity receiver would usually be covered with a layer of coating having high absorptivity for sunlight. The purpose of taking this measure is to improve the thermal efficiency of the receiver. However, to the best knowledge of the authors, there are few investigations about the influence of absorber emissivity on thermal efficiency of the receiver. In the present work, some numerical studies were carried out to investigate the performance of cavity receiver with the same absorptivity for sunlight but different absorptivity for infrared light. Obviously, the lights emitted by absorber surfaces are almost infrared lights as the temperature is not too high. Therefore, the emissivity of absorber is almost equivalent to the absorptivity for infrared light. The thermal performances of receiver with different emissivity were obtained, and the reasons for variation tendency of performance curves were carefully analyzed. The technology for varying the emissivity (absorptivity for infrared light) of absorber while keeping its absorptivity for sunlight unchanged can be achieved by plating nanoparticles. When nanoparticles are plated on the surface of absorber, the absorption for sunlight and infrared light can be changed. And different materials and diameters

of nanoparticles can also vary the absorption for different wavelengths of the absorber.

2. Computational Model

A combined computational model was employed for calculating the thermal performance of the solar cavity receiver shown in Figure 1, which was proposed by Fang et al. [23]. This model includes three aspects: the calculation for the radiative heat transfer inside the receiver, the selection of the flow boiling heat transfer correlations inside the absorber tubes, and the calculation for the air flow field around the receiver. The thermal efficiency and the heat loss of the receiver are finally obtained by coupling these three aspects with an iterative scheme.

2.1. Calculation for the Radiative Heat Transfer inside the Receiver. The Monte Carlo ray tracing method (MCRT) is used to calculate the radiative heat transfer inside the receiver, which can well adapt to all kinds of complex geometries. MCRT is a random simulation method based on probability statistics. Its basic thought on radiation is that the radiative heat transfer process falls into a series of subprocesses: emission, reflection, absorption, scattering, and escape. Every subprocess has an occurrence probability and is determined by random numbers. It has been considered that every light ray carries no energy, so the MCRT method is separated into two parts: the Monte Carlo simulation and the thermal simulation. This treatment can calculate large-scale light rays and obtain high precision results. The object is divided into many surface units and volume units. Let every unit emit a certain quantity of light rays and every light ray is traced and judged by considering whether it is absorbed, scattered, or reflected by surface or volume units or it escapes from the system. Therefore, the number of light rays that every unit finally gains is counted and the radiative heat transfer factor can be computed. The Monte Carlo simulation part is just for calculating the radiative heat transfer factor RD_{ij} . It is defined as the ratio of the number of light rays unit j gains from unit i to the number of light rays emitted by unit i . The object studied in the present work is a solar cavity receiver shown in Figure 1. Since there is only air inside the receiver and the air almost exerts no radiation, the scattering can be omitted in the radiative heat transfer process and there are no volume units in the system. Therefore, the computational model of the Monte Carlo simulation only includes the emitting location and direction model and the absorption-reflection model. The emitting location and direction model was introduced in detail in the reference by Fang et al. [23]. When a light ray projects onto a surface unit, it would be reflected or absorbed by this unit. At this time, a random number R_α is used to judge whether it is absorbed or not. The absorption-reflection probability model is as below. For sunlight, if $R_\alpha \leq \alpha_{\text{sun}}$, it is absorbed by the unit which it reaches. Similarly, for infrared light, if $R_\alpha \leq \alpha_{\text{infrared}}$, the light ray is also absorbed. Oppositely, if $R_\alpha > \alpha_{\text{sun}}$ or $R_\alpha > \alpha_{\text{infrared}}$, the light ray is reflected. Here, α_{sun} and α_{infrared} , respectively, represent the absorptivity of the surface unit for sunlight and for infrared light. If the light ray is absorbed by the unit,

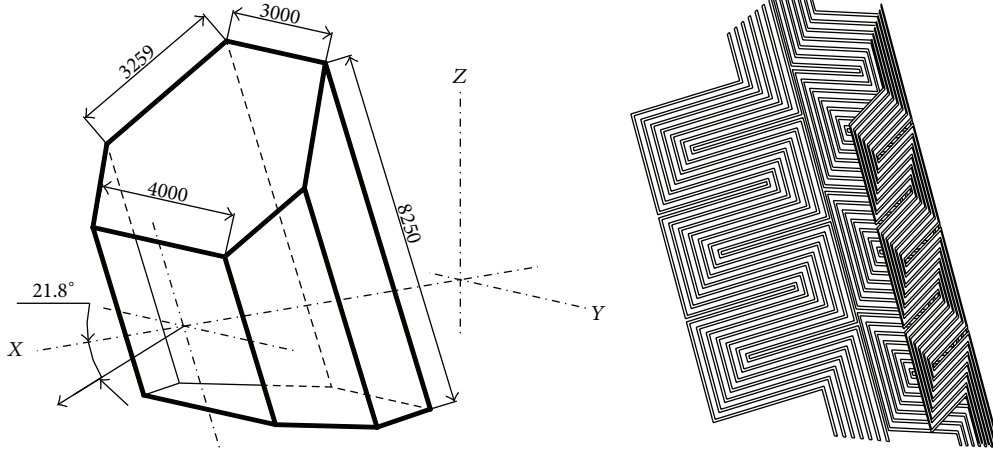


FIGURE 1: Cavity geometry and absorber tubes layout.

the number of light rays absorbed by this unit should increase by one. And if it is reflected, the emitting direction model should be used again to figure out the direction of the reflection. Tracing a number of light rays can obtain the stable statistical results. After the radiative heat transfer factor has been gained, the thermal simulation part can be conducted. It is for calculating the heat flux and the temperature of surface units by solving the energy equations as follows, where $Q_{c,loss}$ represents the convective heat loss and Q_t is the energy transferred inside to the working fluid from the absorber tubes:

$$\varepsilon_i S_i \sigma T_i^4 + Q_{c,loss,i} + Q_{t,i} = \sum_{k=1}^N \varepsilon_k S_k \sigma T_k^4 R D_{ki}, \quad (1)$$

$$(i = 1, N).$$

If the light rays escape from the receiver through the aperture, it is considered as the heat loss. Using the MCRT method can also obtain the reflective heat loss and the radiative heat loss. The reflective heat loss means the solar energy escapes from the receiver after once or several times reflections, while the radiative heat loss means the infrared energy radiated by cavity walls and absorber tubes ultimately projects to the aperture and escapes. If the geometry of the receiver and the computational model of the Monte Carlo simulation keep unchanged, the radiative heat transfer factor will only need to be calculated once before the iterative calculation. But the thermal simulation part should be done every time. In order to study how the emissivity of the absorber tubes affects the thermal performance of the solar cavity receiver, the emissivity is different in every calculation case. Once the emissivity varies, the radiative heat transfer factor needs to be recalculated again.

2.2. Selection of the Flow Boiling Heat Transfer Correlations. Subcooled water delivered by a circulating pump to the absorber tubes is heated into saturated water and steam. The flow during this phase transition process is divided into three regions: single-phase flow region, subcooled boiling

flow region, and saturated boiling flow region. Among them the subcooled boiling flow region should be subdivided according to the mechanism of heat transfer, namely, partial boiling flow region, fully developed boiling flow region, and significant void flow region. Appropriate heat transfer correlations proposed by Kandlikar [30] and identification criteria by Hsu [31] are selected for each region to calculate the convective heat transfer inside the tubes. As long as the inlet conditions of absorber tubes and the heat flux transferred into working fluid are known, the convective heat transfer coefficients and the wall temperature of absorber tubes can be calculated by using selected correlations.

2.3. Calculation for the Air Flow Field around the Receiver. As the solar cavity receiver is usually laid at 60–100 m high on top of the solar tower, the air around it is in a turbulent state. So the convective heat loss between the receiver and the air is another form of heat loss besides the reflective and the radiative heat loss. The commercial software FLUENT is chosen to calculate the convective heat transfer. The standard k - ε turbulent model is selected, because it is widely used for general turbulent flow. And the SIMPLE algorithm is employed. The outer walls of the receiver are considered adiabatic and the no-slip velocity boundary condition is adopted. The side-on wind is chosen as the far field boundary condition, because it is the most rigorous wind condition than other directions, which causes the greatest convective heat loss according to Fang et al. [23]. The wind speed at a height of 10 m is considered to be the reference speed, and the speeds at different heights can be obtained by the following power law expression proposed by Sutton [32]:

$$v = v_{10m} \left(\frac{h}{10} \right)^{1/7}. \quad (2)$$

As long as the conditions of air flow in the far field and the wall temperature of the cavity and the absorber tubes are known, the convective heat loss between the receiver and the air can be calculated.

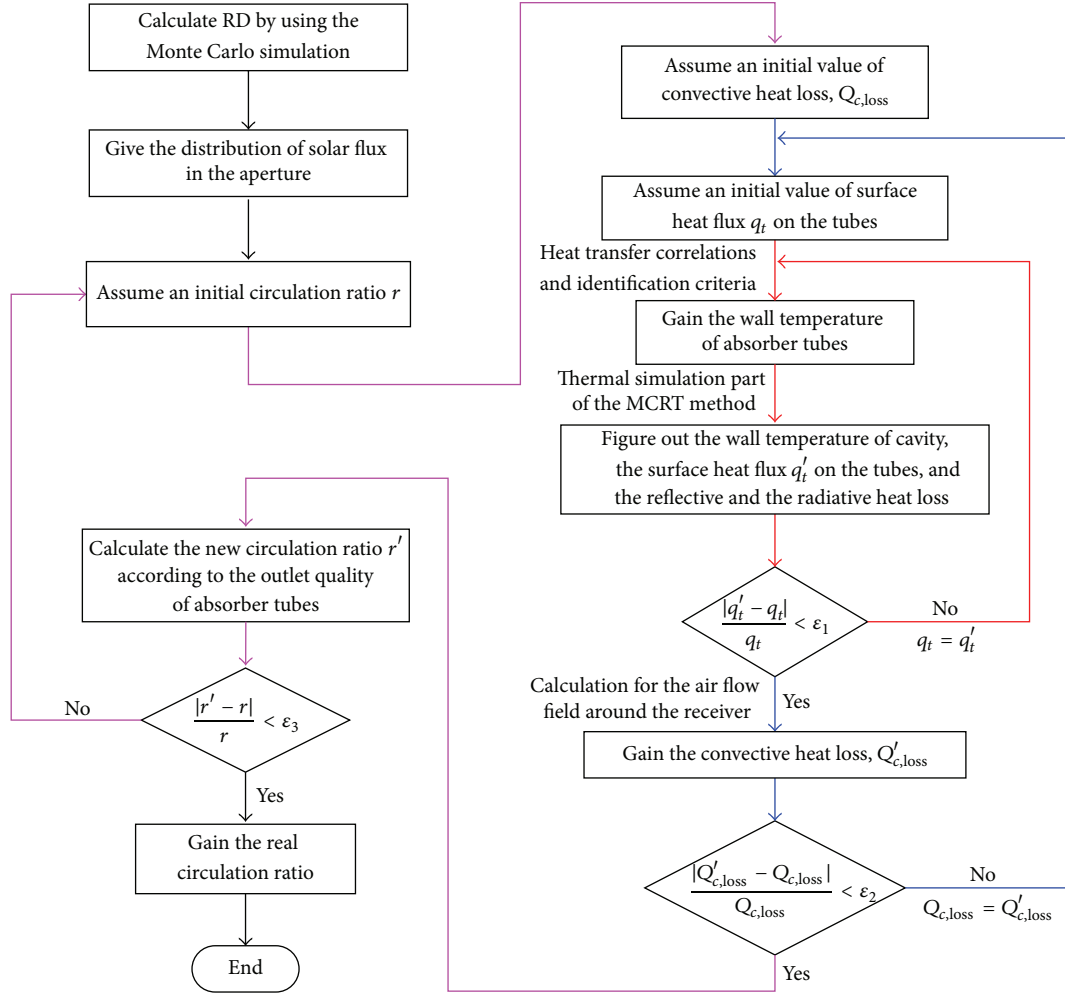


FIGURE 2: Flow chart for calculating the thermal performance of the solar cavity receiver.

2.4. Iterative Solution Procedure. A problem should be noticed that the parameters required for calculating the three aspects above are interrelated and no aspect can be solved alone. When calculating the heat flux on the surface of absorber tubes with the MCRT method, the wall temperature of absorber tubes and the convective heat loss are needed and involved in the energy equations. When calculating the wall temperature of absorber tubes, the heat flux transferred from the tubes into the working fluid must be known. Besides, when calculating the convective heat loss between the receiver and the air, the wall temperature of the cavity and the absorber tubes is needed as the boundary condition. So in order to figure out all the parameters, an iterative scheme is required by coupling these three aspects.

Figure 2 shows the flow chart for calculating the thermal performance of the solar cavity receiver. At first, the radiative heat transfer factor should be calculated with the Monte Carlo simulation before the iteration. Since the radiative heat transfer takes place between any two surface units, the calculation of radiative heat transfer factor is a time-consuming task. Therefore, a proper number of light rays emitted by every unit are vital in order to ensure the least

time of calculation and the accuracy of results. Under the condition that the distribution of solar flux in the aperture is given, the whole iterative procedure consists of three loops for the thermal performance calculation. The inner loop is for calculating the wall temperature of the cavity and the absorber tubes, the heat flux on the surface of tubes, and the reflective and the radiative heat loss. The second loop is for calculating the convective heat loss between the receiver and the air with FLUENT. And the outer loop is used to figure out the circulation ratio. It means the ratio of the total recirculated mass flow rate in the absorber tubes to the mass flow rate of saturated steam generated, which can be calculated according to the outlet quality.

3. Results and Discussion

A solar cavity receiver with the similar geometry to CESA-1 receiver [22] was adopted in the present work for studying the influence of surface emissivity. The cavity is a prism with inclined top and bottom faces, which is shown in Figure 1. The back wall of the cavity is 8.25 m in height and 3 m in width. The width of the two side walls adjacent to

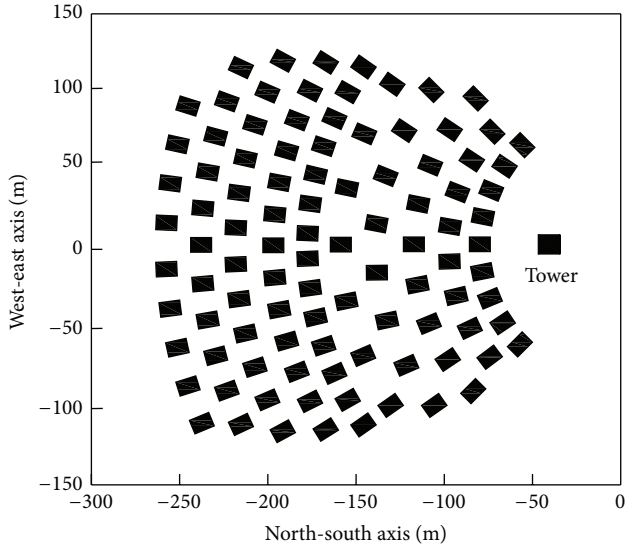


FIGURE 3: Layout of heliostat field.

the back wall is also 3 m, while the other two side walls near the aperture are 2 m in width. There is only one aperture of $4\text{ m} \times 4\text{ m}$ on the front surface of the receiver. There are three panels of absorber tubes, the layout of which can be found in Figure 1, installed inside the cavity. According to Baker's description referring to CESA-1 [22], the three back walls inside the cavity gain much more heat flux than other walls. Therefore, the absorber tubes are arranged in front of these walls and cover the back walls as much as possible. Every panel is formed of a series of stainless steel serpentine tubes, and the gap between every two tubes is filled with flat steel. This kind of design can make the absorber tubes get more energy and protect the back walls against direct irradiation. The central panel has 7 passes and 20 tubes/pass, while the each side one, respectively, has 6 passes. The receiver was assumed to be laid at a height of 100 m. And it has a downward inclination of 21.8° in order to gain the most solar energy from heliostats. Several boundary conditions should be given before calculating the thermal performance of the solar cavity receiver. The layout of the heliostat field designed by Wang and Wei [33] was employed to obtain the irradiation situation in the aperture. Figure 3 shows the layout of heliostat field. There are 100 sets of parabolic mirrors with a square border of $10\text{ m} \times 10\text{ m}$ in the heliostat field. The solar tower in front of the heliostat field is about 120 m in height. Figure 4 shows the distribution of solar flux in the aperture, which was considered as the inlet boundary condition in the thermal simulation part of MCRT method. The distribution appears to be highly nonuniform. The center of the aperture gets the highest solar flux, and at the boundary much lower solar flux is concentrated. These data were obtained from the Institute of Optics and Fine Mechanics and Physics, Chinese Academy of Sciences, which were calculated according to the layout of the heliostat field mentioned above. The reflected sunlight irradiates to the aperture of the cavity within a certain range of angle due to the fan pattern of heliostats. And Figure 5

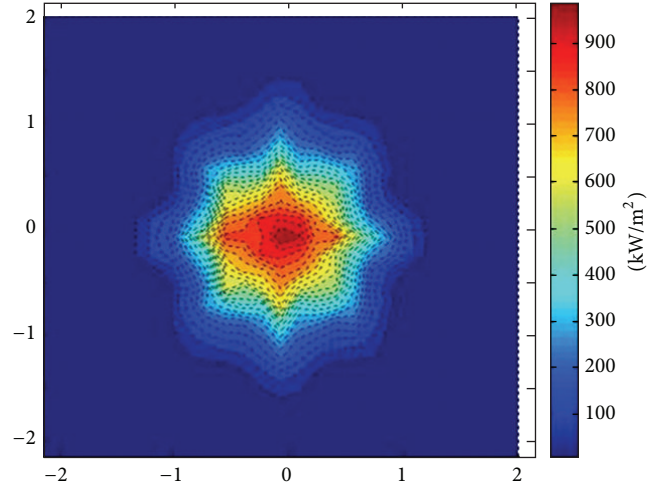


FIGURE 4: Distribution of solar flux in the aperture.

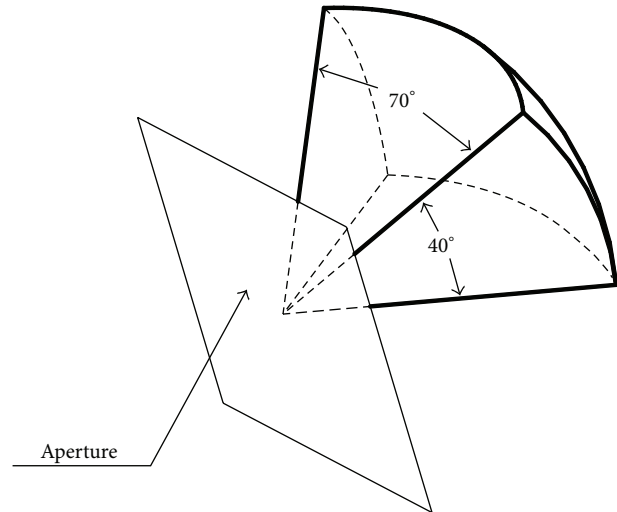


FIGURE 5: Range of solar irradiation angles.

shows the range of irradiation angles. It is 70° in left-to-right direction, with each side 35° , while it is 40° in top-to-bottom direction, with 30° upward and 10° downward. Solar irradiation angles were regarded as the emitting directions of rays in the aperture when the Monte Carlo simulation part was conducted. The wind speed at 10 m high above ground was assumed to be 6 m/s. So the wind speed around the receiver can be calculated by the expression (2). The sketch map of the side-on wind is shown in Figure 6. And the wind flows horizontally from the right side of the receiver. When the aperture of the cavity acquires as much solar flux as shown in Figure 4, the receiver operates under the steady-state, and the rated working pressure is 7 MPa. All the absorber tubes have the same inlet temperature. The circulating mass flow rate is 70 t/h for the central panel, while it is 35 t/h for each side one.

The focus of this paper is to study the effects of emissivity of the absorber tubes on the thermal performance of the solar

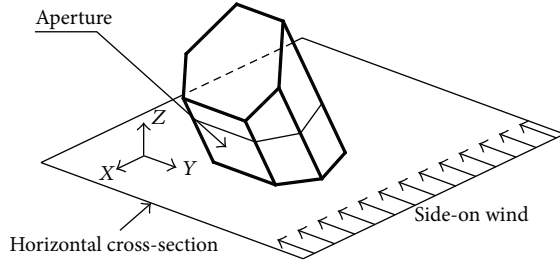


FIGURE 6: Sketch map of side-on wind.

TABLE 1: Emissivity and absorptivity of the materials inside the receiver.

Materials	Emissivity	Absorptivity for sunlight	Absorptivity for infrared light
Firebrick (cavity walls)	0.9	0.9	0.9
Stainless steel tube (absorber tubes)	0.2, 0.4, 0.6, 0.8	0.8	0.2, 0.4, 0.6, 0.8

cavity receiver. Table 1 lists the emissivity and the absorptivity of the materials inside the receiver. Among them, the material of the cavity walls is firebrick, and it is usually dark color. Therefore, the emissivity and the absorptivity of the cavity walls are both quite high, and they were set to be 0.9. Because the absorber tubes should obtain solar energy as much as possible, the absorptivity for sunlight is also high and the value is 0.8. In the present study, the emissivity of the absorber tubes is the key research variable. It, respectively, increases from 0.2 to 0.8. It should be noticed that the absorptivity for infrared light is equal to the emissivity of the materials, which can be observed from Table 1. According to Kirchhoff's law [28], for a diffuse gray body, the absorptivity is equal to the emissivity at the same temperature, which means $\alpha(T) = \epsilon(T)$. When the receiver works in normal conditions, the temperature of cavity walls is 300–500°C and the outer wall of absorber tubes has the temperature of 300–400°C. The absorptivity for infrared light will not change obviously within the temperature difference of 200°C. Besides, the walls and tubes will emit infrared light mostly as the temperature is not very high. Therefore, both for the cavity walls and the absorber tubes, the absorptivity for infrared light was considered to be the same as the emissivity. When calculating the thermal performance of the solar cavity receiver with the increase of the emissivity, the absorptivity for infrared light varies accordingly.

Figures 7 and 8 illustrate the change trends of thermal efficiency and heat loss of the receiver when the emissivity of the absorber tubes varies from 0.2 to 0.8. The results show that the thermal efficiency increases and the total heat loss decreases with increasing emissivity. The infrared radiative heat transfer exists between the absorber tubes and the cavity walls inside the receiver. And the temperature of cavity walls is usually higher than the absorber tubes. When the emissivity (absorptivity for infrared light) of tubes increases, more infrared energy radiated from cavity walls is obtained

by the absorber tubes. That is the reason for the rising thermal efficiency with increasing emissivity. Compared with the external receiver, which is another type of receivers utilized in tower-type solar power system, these results are not applicable. Because the absorber tubes are exposed to the air in the external receiver, the radiative heat loss will rise when the emissivity of tubes increases. However, it can be noticed that, in Figure 7, the increase of thermal efficiency is only about 1.6% although the emissivity increases from 0.2 to 0.8. The absolute value of total heat loss only decreases by about 83.5 kW. It indicates that the change of the emissivity of the absorber tubes has small effects on the thermal efficiency of the receiver. The total heat loss is the sum of reflective heat loss, radiative heat loss, and convective heat loss. The trends of three kinds of heat loss are, respectively, shown in Figure 8. Since the absorptivity for sunlight is unchanged in four different cases, the behaviors of sunlight, which is absorbed or reflected by the units inside the receiver, are all the same. It causes the reflective heat loss unchanged with the increase of the emissivity. The radiative heat loss decreases from 227 kW to 167 kW, reducing by about 26.4%, as can be seen from Figure 8. The radiative heat loss comes from the infrared energy radiated by absorber tubes and cavity walls escaping through the aperture. The average wall temperature of absorber tubes is plotted in Figure 9. It can be found that the wall temperature of three panels varies a little and slightly increases with increasing emissivity. It can be explained as below. The emissivity of tubes increases, which will make heat loss of the receiver and radiation of tubes larger, but the energy obtained by the tubes will not decrease. Because the tubes are inside the cavity, they can obtain the infrared energy from cavity walls, which usually have higher temperature. It should be noticed that the absorptivity of tubes for infrared light is equal to the emissivity. So the higher the emissivity of tubes is, the more energy the tubes will get from cavity walls. Figure 10 shows the distributions of temperature of cavity walls. As the absorptivity of tubes for infrared light increases, the absorber tubes gain more infrared energy from the cavity walls. So the temperature of cavity walls decreases with increasing emissivity. The reduction of wall temperature of the cavity is the major reason for the decrease of the radiative heat loss. The convective heat loss is the main form of heat loss, as can be seen in Figure 8, which is more than twice as much as the reflective heat loss and the radiative heat loss. It also decreases a little when the emissivity increases from 0.2 to 0.8, because the temperature of cavity walls is reduced. It can also be observed from Figure 10 that the top face gets the most heat flux and has the highest temperature than other walls, which is determined by the limit of solar irradiation angles. From Figure 5, it can be deduced that the upper part of the middle panel, which covers the back walls of the cavity, will receive the most sunlight. So the top face, nearest to this part, will obtain the most reflected sunlight. Since the right side-on wind is selected in the present study, the air inside the receiver swirls from the left side wall to the right side wall. Thus, the air temperature near the right side wall would be higher than that near the left side wall due to heat transfer along the air flow path. So the temperature of the left wall is relatively lower than the right one. As the absorber

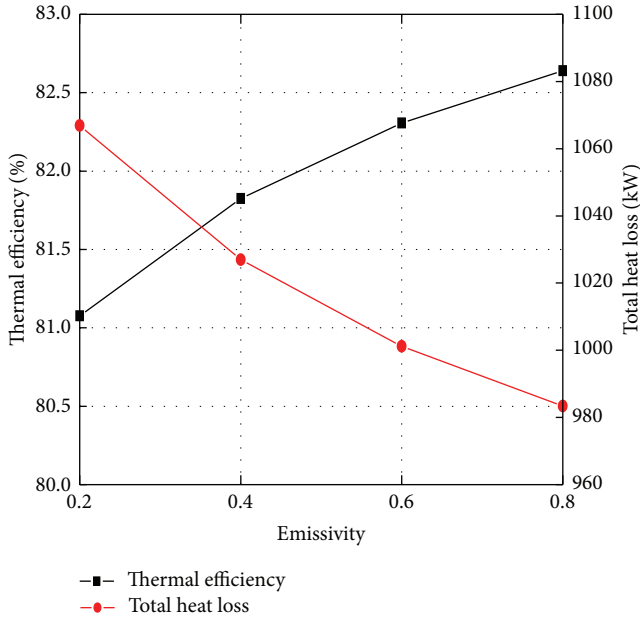


FIGURE 7: Thermal efficiency and total heat loss of the receiver.

tubes are laid in front of the three back walls and they block most of radiative energy, the temperatures of the three back walls are the lowest. But some areas which are not covered by the panels have the higher temperature. The distribution of heat flux on the absorber panels was figured out and shown in Figure 11. When the emissivity of absorber tubes varies from 0.2 to 0.8, the distributions of heat flux are almost the same and increase slightly. The solar cavity receiver usually has only one aperture; thus the sunlight projects onto the surfaces inside the receiver only from one side. And the distribution of input solar flux itself is nonuniform in the aperture. Due to the two reasons mentioned above, the distribution of heat flux on the absorber panels appears highly nonuniform, as can be found from Figure 11. The middle part of each panel gets larger heat fluxes, and the largest value is about 250 kW/m^2 appearing in the middle of the central panel. About 50.5% of the energy is gained by the central panel, 24.9% by the right side one, and 24.6% by the left side one. The data calculated in the present study are in good agreement with the results from Baker et al. [22] and Fang et al. [23], which also showed that about half of the energy is absorbed by the central panel and a quarter by each side one. The heat flux can directly affect the outer wall temperature of the absorber panels. As the emissivity of tubes increases, the distributions of outer wall temperature of three panels also vary a little and are much like that shown in Figure 12. The highest temperature, about 365°C , also appears in the middle of the central panel, which is about 80°C higher than the saturated temperature (285°C at 7 MPa).

4. Conclusions

The numerical study on the thermal performance of a saturated water/steam solar cavity receiver with different

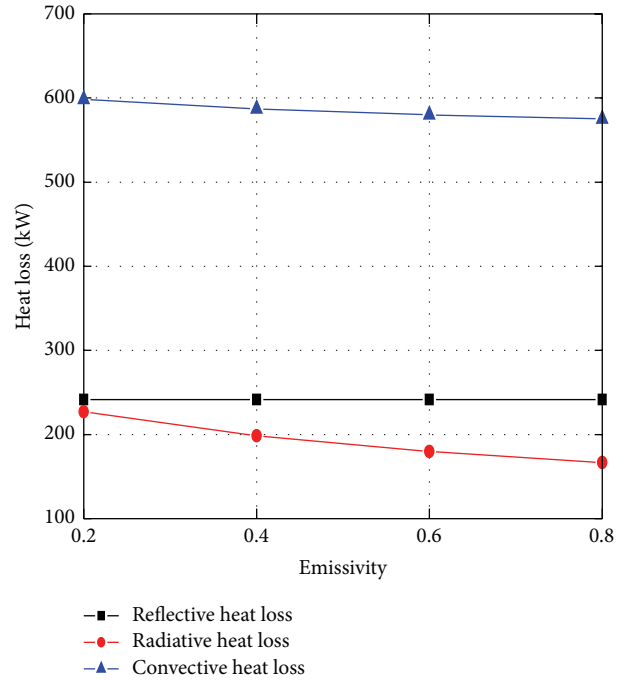


FIGURE 8: Three kinds of heat loss of the receiver.

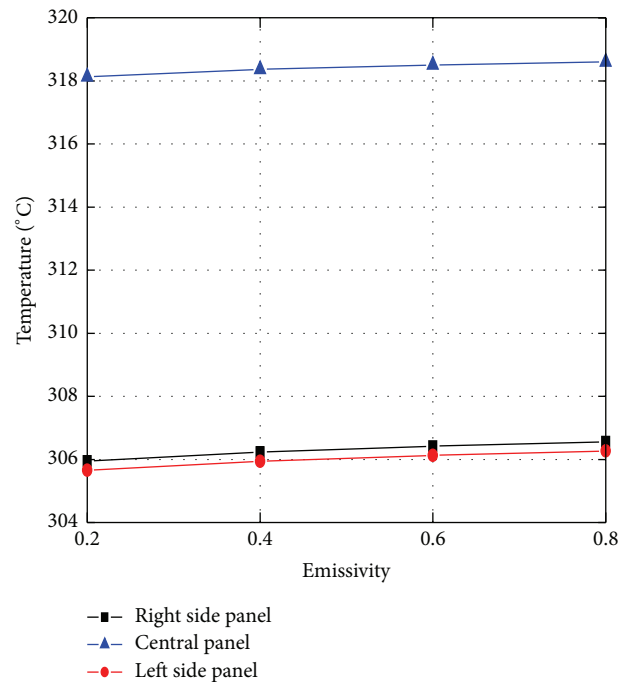


FIGURE 9: Average wall temperature of absorber tubes.

absorber emissivity was simulated in the present work. The results showed that the thermal efficiency increases and the total heat loss decreases with increasing emissivity of the absorber tubes. But the increase of the thermal efficiency is only about 1.6% when the emissivity varies from 0.2 to 0.8. The change of absorber emissivity has slight effect on the thermal performance of the receiver. Therefore, in order to

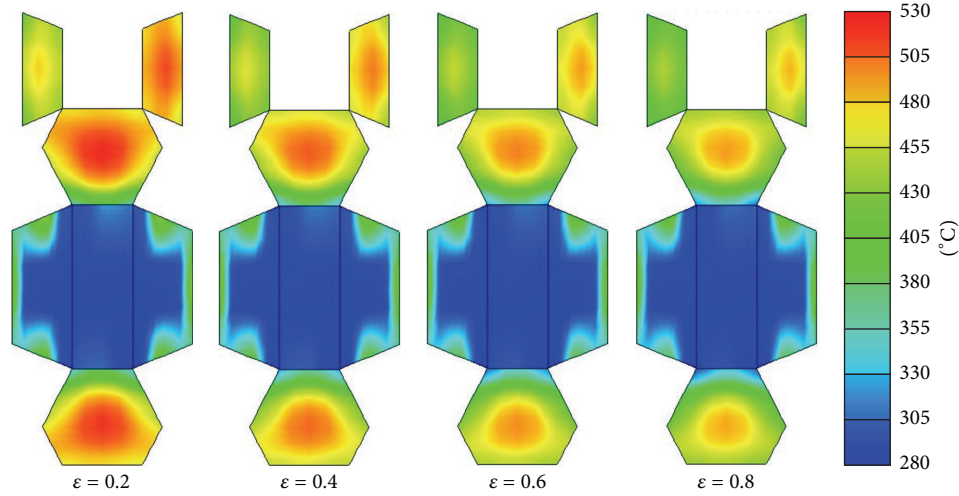


FIGURE 10: Distributions of temperature of cavity walls.

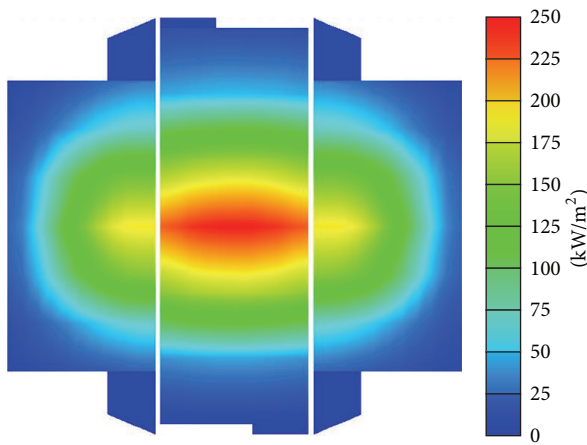


FIGURE 11: Distribution of heat flux on the absorber panels.

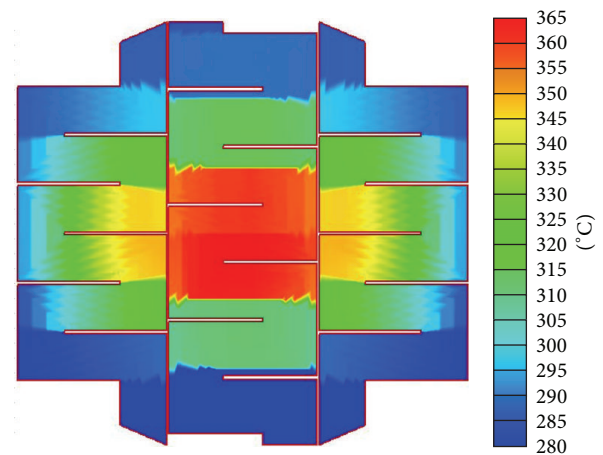


FIGURE 12: Distribution of outer wall temperature of the absorber panels.

absorb more solar energy to achieve high thermal efficiency, the layer of coating covered on the surface of absorber tubes should have absorptivity for sunlight as high as possible, but its emissivity is not an important factor. In addition, the reason for the decrease of total heat loss was also carefully analyzed. It was found that the temperature reduction of the cavity walls causes the decrease of radiative and convective heat losses.

Nomenclature

- RD: Radiative heat transfer factor
- R_α : Random number
- Q: Energy, W
- T: Temperature, K
- S: Area, m^2
- v: Velocity, m/s
- h: Height, m.

Greek Symbols

- α : Absorptivity
- σ : Stefan-Boltzmann constant, $W/m^2 K^4$
- ϵ : Emissivity.

Conflict of Interests

The authors (Jiabin Fang, Nan Tu, and Jinjia Wei) declare that there is no conflict of interests regarding this paper.

Acknowledgments

The present work is supported by the National Basic Research Program of China (no. 2010CB227102) and the Specialized Research Fund for the Doctoral Program of Higher Education of China (no. 20130201110043).

References

- [1] A. L. Ávila-Marín, "Volumetric receivers in solar thermal power plants with central receiver system technology: a review," *Solar Energy*, vol. 85, no. 5, pp. 891–910, 2011.
- [2] A. M. Clausing, "An analysis of convective losses from cavity solar central receivers," *Solar Energy*, vol. 27, no. 4, pp. 295–300, 1981.
- [3] A. M. Clausing, "Convective losses from cavity solar receivers—comparisons between analytical predictions and experimental results," *Journal of Solar Energy Engineering*, vol. 105, no. 1, pp. 29–33, 1983.
- [4] J. O. Juárez, J. F. Hinojosa, J. P. Xamán, and M. P. Tello, "Numerical study of natural convection in an open cavity considering temperature-dependent fluid properties," *International Journal of Thermal Sciences*, vol. 50, no. 11, pp. 2184–2197, 2011.
- [5] M. Prakash, S. B. Kedare, and J. K. Nayak, "Numerical study of natural convection loss from open cavities," *International Journal of Thermal Sciences*, vol. 51, no. 1, pp. 23–30, 2012.
- [6] S. Paitoonsurikarn, K. Lovegrove, G. Hughes, and J. Pye, "Numerical investigation of natural convection loss from cavity receivers in solar dish applications," *Journal of Solar Energy Engineering*, vol. 133, no. 2, Article ID 021004, 10 pages, 2011.
- [7] T. Taumoeolau, S. Paitoonsurikarn, G. Hughes, and K. Lovegrove, "Experimental investigation of natural convection heat loss from a model solar concentrator cavity receiver," *Journal of Solar Energy Engineering*, vol. 126, no. 2, pp. 801–807, 2004.
- [8] P. le Quere, F. Penot, and M. Mirenyat, "Experimental study of heat loss through natural convection from an isothermal cubic open cavity," Sandia Laboratory Report SAND81-8014, 1981.
- [9] D. J. Reynolds, M. J. Jance, M. Behnia, and G. L. Morrison, "An experimental and computational study of the heat loss characteristics of a trapezoidal cavity absorber," *Solar Energy*, vol. 76, no. 1–3, pp. 229–234, 2004.
- [10] J. A. Harris and T. G. Lenz, "Thermal performance of solar concentrator/cavity receiver systems," *Solar Energy*, vol. 34, no. 2, pp. 135–142, 1985.
- [11] K. S. Reddy and N. S. Kumar, "Combined laminar natural convection and surface radiation heat transfer in a modified cavity receiver of solar parabolic dish," *International Journal of Thermal Sciences*, vol. 47, no. 12, pp. 1647–1657, 2008.
- [12] K. S. Reddy and N. S. Kumar, "An improved model for natural convection heat loss from modified cavity receiver of solar dish concentrator," *Solar Energy*, vol. 83, no. 10, pp. 1884–1892, 2009.
- [13] M. M. Gonzalez, J. H. Palafox, and C. A. Estrada, "Numerical study of heat transfer by natural convection and surface thermal radiation in an open cavity receiver," *Solar Energy*, vol. 86, no. 4, pp. 1118–1128, 2012.
- [14] A. K. Sharma, K. Velusamy, C. Balaji, and S. P. Venkateshan, "Conjugate turbulent natural convection with surface radiation in air filled rectangular enclosures," *International Journal of Heat and Mass Transfer*, vol. 50, no. 3–4, pp. 625–639, 2007.
- [15] A. K. Sharma, K. Velusamy, and C. Balaji, "Interaction of turbulent natural convection and surface thermal radiation in inclined square enclosures," *Heat and Mass Transfer*, vol. 44, no. 10, pp. 1153–1170, 2008.
- [16] V. Vivek, A. K. Sharma, and C. Balaji, "Interaction effects between laminar natural convection and surface radiation in tilted square and shallow enclosures," *International Journal of Thermal Sciences*, vol. 60, pp. 70–84, 2012.
- [17] S. G. Martyushev and M. A. Sheremet, "Conjugate natural convection combined with surface thermal radiation in an air filled cavity with internal heat source," *International Journal of Thermal Sciences*, vol. 76, pp. 51–67, 2014.
- [18] S.-Y. Wu, J.-Y. Guan, L. Xiao, Z.-G. Shen, and L.-H. Xu, "Experimental investigation on heat loss of a fully open cylindrical cavity with different boundary conditions," *Experimental Thermal and Fluid Science*, vol. 45, pp. 92–101, 2013.
- [19] R. E. Hogan, R. B. Diver, and W. B. Stine, "Comparison of a cavity solar receiver numerical model and experimental data," *Journal of Solar Energy Engineering*, vol. 112, no. 3, pp. 183–190, 1990.
- [20] X. Li, W. Kong, Z.-F. Wang, C. Chang, and F. Bai, "Thermal model and thermodynamic performance of molten salt cavity receiver," *Renewable Energy*, vol. 35, no. 5, pp. 981–988, 2010.
- [21] Q.-Q. Zhang, X. Li, Z.-F. Wang, C. Chang, and H. Liu, "Experimental and theoretical analysis of a dynamic test method for molten salt cavity receiver," *Renewable Energy*, vol. 50, pp. 214–221, 2013.
- [22] A. F. Baker, S. E. Faas, L. G. Radosovich, and A. C. Skinrood, "U.S.–Spain evaluation of the Solar One and CESA-1 receiver and storage system," Sandia National Laboratories SAND88-8262, 1989.
- [23] J. B. Fang, J. J. Wei, X. W. Dong, and Y. S. Wang, "Thermal performance simulation of a solar cavity receiver under windy conditions," *Solar Energy*, vol. 85, no. 1, pp. 126–138, 2011.
- [24] J. B. Fang, N. Tu, and J. J. Wei, "Numerical investigation of start-up performance of a solar cavity receiver," *Renewable Energy*, vol. 53, pp. 35–42, 2013.
- [25] Q. Yu, Z. Wang, and E. Xu, "Simulation and analysis of the central cavity receiver's performance of solar thermal power tower plant," *Solar Energy*, vol. 86, no. 1, pp. 164–174, 2012.
- [26] Q. Yu, Z. Wang, E. Xu, X. Li, and M. Guo, "Modeling and dynamic simulation of the collector and receiver system of 1MWe DAHAN solar thermal power tower plant," *Renewable Energy*, vol. 43, pp. 18–29, 2012.
- [27] M. J. Montes, A. Rovira, J. M. Martínez-Val, and A. Ramos, "Proposal of a fluid flow layout to improve the heat transfer in the active absorber surface of solar central cavity receivers," *Applied Thermal Engineering*, vol. 35, no. 1, pp. 220–232, 2012.
- [28] S. M. Yang and W. Q. Tao, *Heat Transfer*, Higher Education Press, Beijing, China, 2006.
- [29] P. Kesselring and C. S. Selvage, *The IEA/SSPS Solar Thermal Power Plants: Facts and Figures, Final Report of the International Test and Evaluation Team (ITET)*, Springer, New York, NY, USA, 1986.
- [30] S. G. Kandlikar, "A general correlation for saturated two-phase flow boiling heat transfer inside horizontal and vertical tubes," *Journal of Heat Transfer*, vol. 112, no. 1, pp. 219–228, 1990.
- [31] Y. Y. Hsu, "On the size range of active nucleation cavities on a heating surface," *Journal of Heat Transfer*, vol. 84, no. 3, pp. 207–216, 1962.
- [32] O. G. Sutton, "Note on variation of the wind with height," *Quarterly Journal of the Royal Meteorological Society*, vol. 58, no. 243, pp. 74–76, 1932.
- [33] R.-T. Wang and X.-D. Wei, "Shadow of heliostat field in the solar tower power plant," *Acta Photonica Sinica*, vol. 38, no. 9, pp. 2414–2418, 2009.

Research Article

Fabrication of TiO₂ Nanofilm Photoelectrodes on Ti Foil by Ti Ion Implantation and Subsequent Annealing

Yichao Liu, Feng Ren, Guangxu Cai, Mengqing Hong, Wenqing Li,
Xiangheng Xiao, Wei Wu, and Changzhong Jiang

School of Physics and Technology, Center for Ion Beam Applications, Wuhan University, Wuhan 430072, China

Correspondence should be addressed to Feng Ren; fren@whu.edu.cn

Received 11 March 2014; Accepted 12 April 2014; Published 8 May 2014

Academic Editor: Shaohua Shen

Copyright © 2014 Yichao Liu et al. This is an open access article distributed under the Creative Commons Attribution License, which permits unrestricted use, distribution, and reproduction in any medium, provided the original work is properly cited.

The TiO₂ photoelectrodes fabricated on the substrate of Ti foils by Ti ions implantation and subsequent annealing at different temperatures were applied for water splitting. The size of TiO₂ nanoparticles increased with annealing temperatures, and the GIXRD patterns and Raman spectra demonstrate that the phase of TiO₂ turns to rutile at high temperature. The photoelectrochemical (PEC) and X-ray photoelectron spectroscopy (XPS) spectra of the valence band demonstrate that the samples annealed at 400 and 500°C show the n-type property. The sample annealed at 600°C shows the weak p-type TiO₂ property. For the sample annealed at 700°C, the negative photocurrent is main, which mainly performs the p-type property of TiO₂. The IPCE values indicate that the absorption edges are red shifted with the increase of annealing temperatures.

1. Introduction

The production of clean chemical fuels by solar conversion is an attractive and sustainable solution to the energy shortage. Since the solar water splitting on a TiO₂ photoelectrode was discovered by Fujishima and Honda [1], the hydrogen and electric power from water using solar energy has attracted considerable interest because it promises clean, environmentally friendly energy generation. The photoelectrochemical (PEC) reaction has emerged to convert solar energy into chemical energy [2, 3]. The PEC splitting of water into hydrogen and oxygen by the direct use of sunlight is an ideal method. As we know, a PEC cell is based on a semiconductor/liquid junction, where the minority charges generated on light absorption in the semiconductor are driven into the solution by the electric field at the junction, where they can drive a redox reaction [4–6].

In our previous work, we found that TiO₂ nanofilms can be formed on the surface of silica by the Ti⁺ ions implantation and subsequent annealing [7]. However, the substrate is nonconductive and the formed TiO₂ films cannot be used as photoelectrode. In order to acquire TiO₂ nanofilms on the substrate of Ti foil, we try to fabricate the TiO₂

by Ti ion implantation and subsequent annealing. The n-type properties of the as-prepared TiO₂ photoelectrode are detected at low temperatures of 400 and 500°C, while, for the samples annealed at 600 and 700°C, the current-potential curves show the property of p-type TiO₂. The photocurrent of the sample annealed at 500°C under UV-Visible light illumination with applied potential of 0.8 V (versus SCE) is 139.2 $\mu\text{A}/\text{cm}^2$.

2. Experimental

We used high purity (99.9%) Ti foils in our experiment, and the thickness of the Ti foil is 0.5 mm. High purity Ti foils were cleaned in a mixture of hydrofluoric acid, nitric acid, and purified water for 5 minutes and then implanted with Ti ions at an accelerate voltages of 20 kV, to the fluence of 3×10^{17} ions/cm² using a metal vapor vacuum arc (MEVVA) ion source implanter. The implanted samples were annealed at 400, 500, 600, and 700°C for 6 hours in oxygen atmosphere. The surface morphologies of the annealed samples were examined by scanning electron microscope (SEM, FEI Versa 3D). Raman scattering spectrum measurements were performed by a MicroRaman Microscope (Jobin-Yvon LabRAM

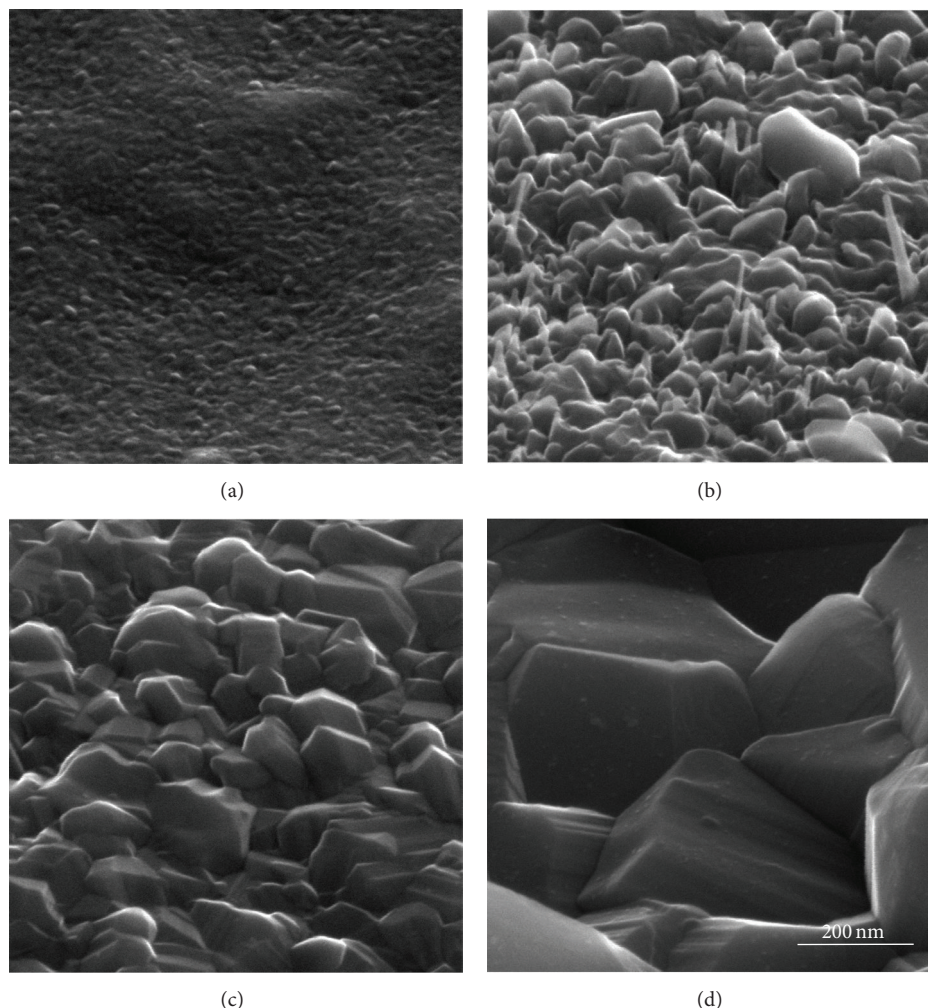


FIGURE 1: SEM image of the TiO_2 formed by Ti implanted into Ti foil and subsequent annealing at 400 (a), 500 (b), 600 (c), and 700°C (d) for 6 hours in oxygen atmosphere, respectively.

HR) using an Ar^+ laser (488 nm) as the excitation source to identify the crystalline phase of TiO_2 . The X-ray diffraction (XRD) patterns were obtained from a PANalytical X'pert MPD Pro diffractometer operated at 40 kV and 40 mA using Ni-filtered $\text{Cu K}\alpha$ irradiation (Wavelength 1.5406 Å). The chemical composition was obtained by X-ray photoelectron spectroscopy (Axis UltraDLD, Kratos) with monoaluminum $\text{K}\alpha$ radiation. The charge calibration was done by correcting Cls line of adventitious carbon setting to 284.8 eV to compensate the charge effect. UV-Vis diffuse reflection spectra (DRS) and monochromatic incident photon-to-electron conversion efficiency (IPCE) were detected to confirm the optical properties.

Photoelectrochemical measurements were carried out in a convenient three-electrode cell. Ti foils implanted by Ti ions onto a special designed electrode holder were used as the working electrodes. The surface areas exposed to electrolyte were fixed at 0.785 cm^2 . The PEC properties of all samples are characterized in 0.5 M Na_2SO_4 aqueous solution using three-electrode configuration with a Pt and an Ag/AgCl

electrode as a counter electrode and a reference electrode. An electrochemical workstation (CHI760D) and a 300 W Xe lamp (100 mW/cm^2) as the solar irradiated simulator with light intensity set at 100 mW/cm^2 through an AM 1.5G filter were used for photocurrent-potential measurement. Incident photon-to-current conversion efficiency (IPCE) measurements were performed using a 300 W Xe lamp integrated with a computer-controlled monochromator, a photo chopper (PARC), and a lock-in amplifier used for photocurrent detection. IPCE measurements were performed in 0.5 M Na_2SO_4 aqueous solution as electrolyte, and the applied potential was controlled at 0.8 V versus Ag/AgCl reference electrode.

3. Results and Discussion

Figure 1 shows the SEM images of nanoparticles formed by Ti ions implanted into Ti foil and subsequent annealing at 400, 500, 600, and 700°C for 6 hours in oxygen atmosphere. In order to observe the nanoparticles clearly and present a three-dimensional image, we set the tilt angle to 52° . When

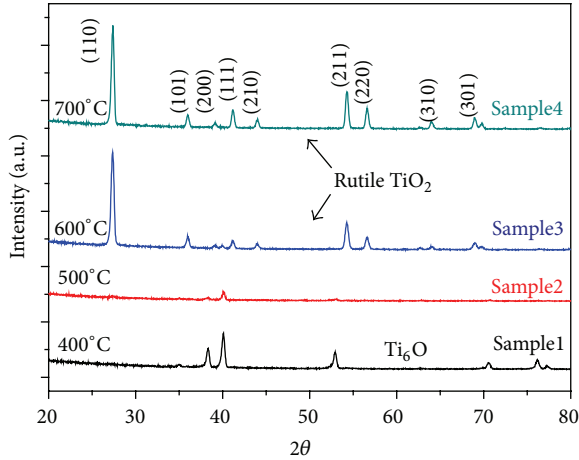


FIGURE 2: XRD patterns of TiO_2 , which are annealed at different temperatures.

the sample was annealed at 400°C , small titanium oxide nanoparticles were formed on the surface of the substrate, the average size of the nanoparticles is 25.8 nm, as shown in Figure 1(a). When the annealing temperature increases, the size of nanoparticles grows quickly. The average size of the nanoparticles grows to 93.3, 151.7, and 675 nm, for the annealing temperatures of 500, 600, and 700°C , respectively.

Figure 2 shows GIXRD patterns of the TiO_2 formed by Ti ions implantation into Ti foils and subsequent annealing at 400, 500, 600, and 700°C for 6 hours in oxygen atmosphere, respectively. It is found that the phase composition strongly depends on the annealing temperatures. With the increase of annealing temperature, the quality of titanium oxide changed from amorphous to rutile phase. The sample annealed at 400°C is Ti_6O . At the annealing temperatures of 600 and 700°C , the titanium oxide transfers mostly to rutile phase.

In order to confirm the ingredients of nanoparticles on the surface of the substrate, we show the Raman spectra of the TiO_2 films formed by Ti implanted into Ti foil and subsequent annealing. As shown in Figure 3, when the annealing temperature is 400°C , the Raman peak located at 140 cm^{-1} is the E_g mode of the TiO_2 in anatase phase [8, 9]. No Raman mode of the Ti_6O is found in the Raman spectra, which may be not in the range of the measurement. The anatase TiO_2 has not been detected in the XRD patterns due to its too fewer amount. With the increase of annealing temperature, two rutile Raman peaks appear at the 442 cm^{-1} (E_g) and 603 cm^{-1} (A_{1g}) [10, 11], which were the first-order Raman spectra of rutile TiO_2 . When the annealing temperature is 700°C , the second-order Raman peak at 234 cm^{-1} becomes stronger [12]. At the same time, the intensity of the E_g and A_{1g} modes became much stronger.

According to the SEM images, the GIXRD patterns, and the Raman spectra, we can conclude that the main content of nanoparticles on the surface of the samples annealed at 400°C is Ti_6O with small amount of TiO_2 nanoparticles. When the annealing temperature is 500°C the content of rutile TiO_2 is increased. As the annealing temperature increases to 600 and

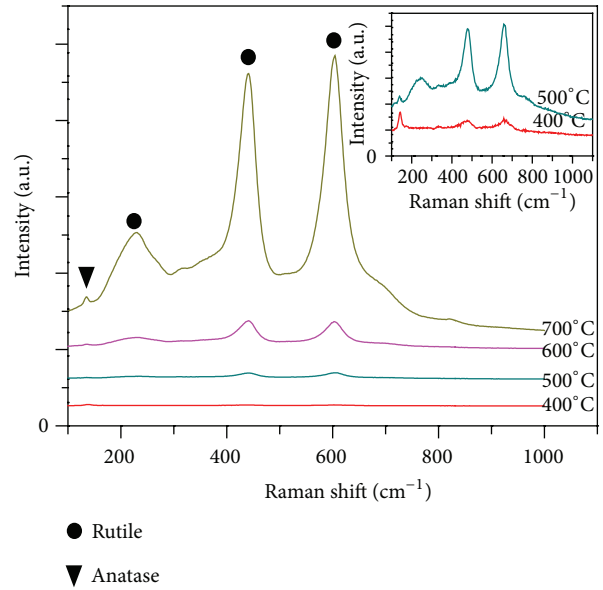


FIGURE 3: The Raman spectra of TiO_2 annealed at different temperatures.

700°C , the main particles are rutile TiO_2 . While annealing at low temperatures, implanted Ti atoms are slowly diffused out of the sample and are oxidized. Therefore, small TiO_2 particles are formed on the sample surface. Meanwhile, the near surface of substrate is also oxidized to Ti_6O . Under higher annealing temperatures, the implanted Ti atoms are easier to diffuse to sample surface and the size of TiO_2 particles grows. In order to confirm the formation of the TiO_2 films, XPS analysis was performed for the Ti-implanted sample to the fluence of 3×10^{17} ions/ cm^2 and annealed at 400, 500, 600, and 700°C for 6 hours. As shown in Figure 4, the binding energy of $\text{Ti}2p_{1/2}$ locates at 464.2 eV, and $\text{Ti}2p_{3/2}$ locates at 458.4 eV belong to the binding energy of Ti^{4+} .

In order to know the optical properties, we test the UV-Visible diffuse reflection spectra (DRS) and monochromatic incident photon-to-electron conversion efficiency (IPCE) of the TiO_2 films. As shown in Figure 5(a), with the increase of annealing temperature, the absorption of light from UV enlarged to visible light region. According to the GIXRD and Raman spectra, the main composition of the sample annealed at 400°C is Ti_6O . The broad absorption is possibly due to the absorption of Ti_6O . The size of TiO_2 nanoparticles increased with the annealing temperatures, and the high temperature easily caused the phase change of TiO_2 nanoparticles to rutile phase, which are the reason that the absorption edges are red shifted.

The IPCE values are shown in Figure 5(b); for the sample annealed at 400°C , the maximum IPCE is 2.9% at the absorption wavelength of 320 nm and is 6.94% for the sample annealed at 500°C . The highest IPCE for the sample annealed at 600°C is 2.8% at the absorption wavelength of 370 nm. The absorption edges are red shifted with the increase of annealing temperatures, indicating the formation of TiO_2 nanoparticles. The further red shift of the absorption

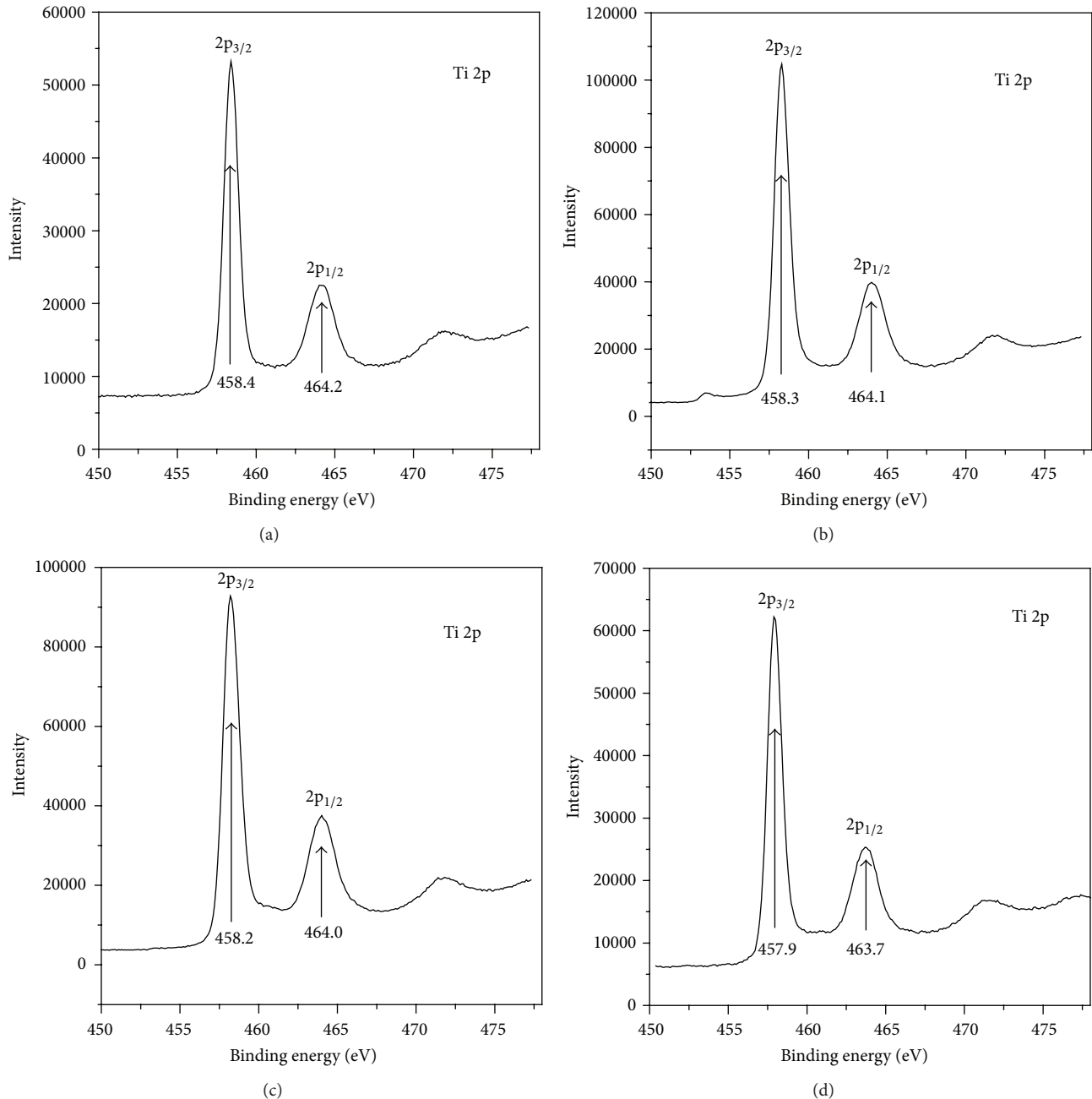


FIGURE 4: XPS spectrum of Ti 2p in the TiO_2 formed by Ti implanted into Ti foil and subsequent annealing at 400 (a), 500 (b), 600 (c), and 700°C (d) for 6 hours in oxygen atmosphere, respectively.

wavelength after annealing at 700°C is due to the increase of the sizes of TiO_2 nanoparticles.

Figure 6(a) shows current-potential curves in 0.5 M Na_2SO_4 aqueous solution under UV-Visible light illumination for TiO_2 formed by Ti ion implantation and subsequent annealing at 400, 500, 600, and 700°C. The samples annealed at 400 and 500°C were n-type Ti_6O . The photocurrent of the sample annealed at 500°C under UV-Visible light illumination with applied potential of 0.8 V (versus SCE) is $139.2 \mu\text{A}/\text{cm}^2$. The samples annealed at 400 or 500°C show positive photocurrent; they present n-type property.

For the samples annealed at 600°C, which have the negative photocurrent at the negative bias and have a positive photocurrent when they are at the positive bias, show the property of both the p-type and n-type TiO_2 . Thus, the sample annealed at 600°C has weak p-type property. For the sample annealed at 700°C, the negative photocurrent is main, which mainly performs the p-type property of TiO_2 . Because the substrate is Ti foils, the Ti ions are abundant and the Ti atoms were diffused to the surface and oxidized during annealing under oxygen atmosphere, and the Ti_6O was also gradually oxidized to TiO_2 with the increase of annealing temperature.

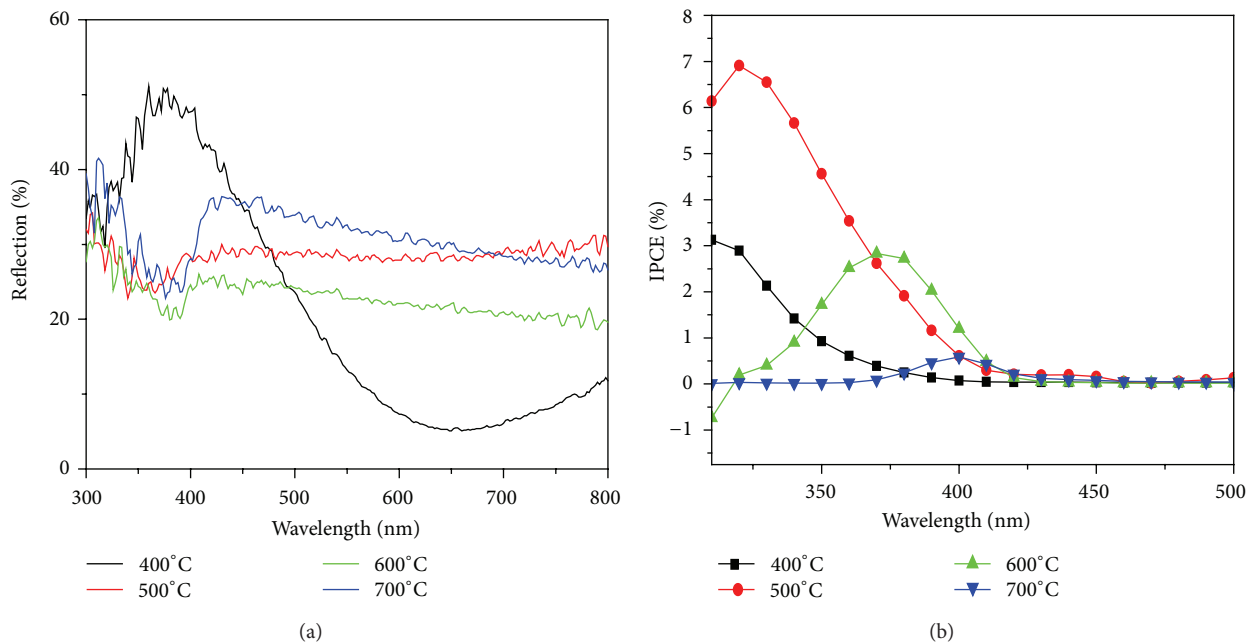


FIGURE 5: The UV-Vis diffuse reflection spectra (DRS) and monochromatic incident photon-to-electron conversion efficiency (IPCE) of the TiO₂ films formed by Ti implanted into Ti foil and subsequent annealing.

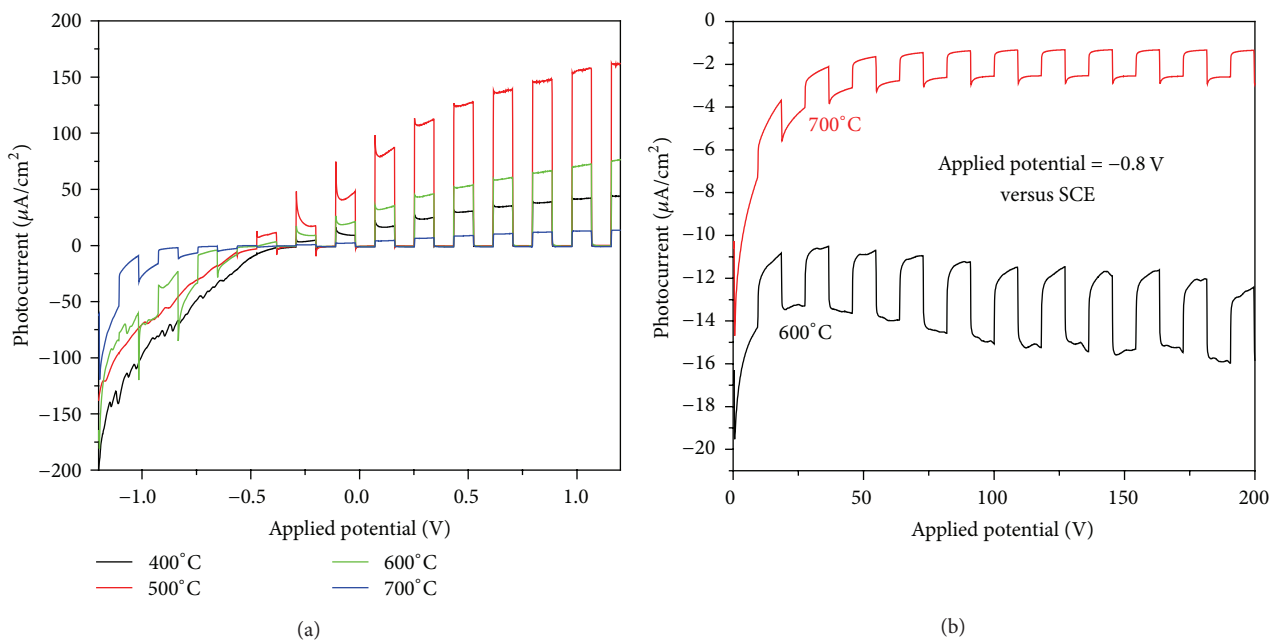


FIGURE 6: (a) The current-potential curves in 0.5 M Na₂SO₄ aqueous solution under simulated solar light for TiO₂ formed by Ti ion implantation and subsequent annealing at 400, 500, 600, and 700°C. (b) The i-t curve annealed at 600 and 700°C.

The samples annealed at 600 and 700°C are rutile TiO₂; some of the Ti ions locate in the interstitial positions, which lead to the property of p-type TiO₂. Figure 6(b) shows the photoelectrochemical measurement of the samples annealed at 600 and 700°C, which were operated by the amperometric i-t curve to evaluate their ability for photocatalytic water splitting under visible light illumination. The photocurrent

was 3.52 μA/cm² at 600°C and 1.60 μA/cm² at 700°C, with applied potential of -0.8 V (versus SCE).

Additional evidence of p-type TiO₂ is from XPS spectra of the valence band region. As shown in Figure 7, the valence band of TiO₂ that was annealed at 400°C (Figure 7(a)) starts from about 2.13 eV. In contrast, the valence band of TiO₂ starts from about 1.66 eV (Figure 7(c)). It means that

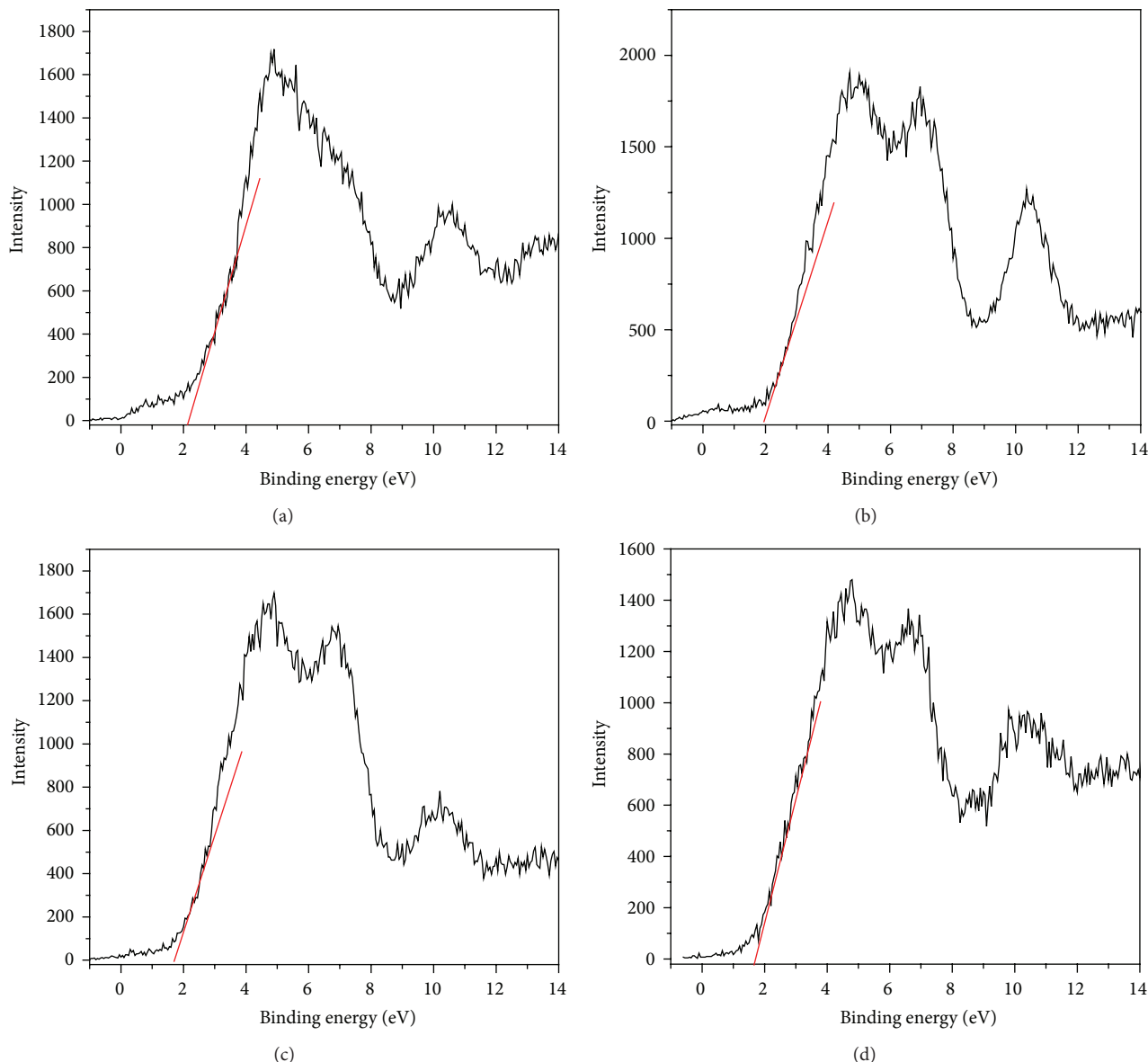


FIGURE 7: XPS spectra of the TiO₂ thin film at the valence band region, annealing at 400 (a), 500 (b), 600 (c), and 700°C (d) for 6 hours in oxygen atmosphere, respectively.

the Fermi level of TiO₂ (0.0 eV) is closer to the valence band of the sample annealing at 600°C; it is reported that the preparation of p-type TiO₂ using the thermal approach needs high temperature [13]. The XPS spectra prove the formation of p-type TiO₂.

4. Conclusion

The TiO₂ nanofilms were formed on the substrate of Ti foils as the photoelectrochemical (PEC) electrode. The size of TiO₂ nanoparticles increased with the increasing of annealing temperatures, and the GIXRD patterns and Raman spectra

demonstrate that the phase of TiO₂ turns to rutile at high temperature. The IPCE values indicate that the absorption edges are red shifted with the increase of annealing temperatures. The n-type properties of the as-prepared TiO₂ photoelectrode are detected at low temperatures of 400 and 500°C. For the samples annealed at 600 and 700°C, the photocurrent shows the property of p-type TiO₂.

Conflict of Interests

The authors declare that there is no conflict of interests regarding the publication of this paper.

Acknowledgments

The authors thank the Natural Science Foundation of China (11175133, 51171132, and 11375134), the Foundations from Chinese Ministry of Education (20110141130004, 311002, and NCET-13-0438), Hubei Provincial Natural Science Foundation (2012FFA042), and the Nano Research Program of Suzhou City (ZXG2013003) for financial support.

References

- [1] A. Fujishima and K. Honda, "Electrochemical photolysis of water at a semiconductor electrode," *Nature*, vol. 238, no. 5358, pp. 37–38, 1972.
- [2] H. Tong, S. Ouyang, Y. Bi, N. Umezawa, M. Oshikiri, and J. Ye, "Nano-photocatalytic materials: possibilities and challenges," *Advanced Materials*, vol. 24, no. 2, pp. 229–251, 2012.
- [3] M. G. Walter, E. L. Warren, J. R. McKone et al., "Solar water splitting cells," *Chemical Reviews*, vol. 110, no. 11, pp. 6446–6473, 2010.
- [4] M. R. Hoffmann, S. T. Martin, W. Choi, and D. W. Bahnemann, "Environmental applications of semiconductor photocatalysis," *Chemical Reviews*, vol. 95, no. 1, pp. 69–96, 1995.
- [5] O. Khaselev and J. A. Turner, "A monolithic photovoltaic-photoelectrochemical device for hydrogen production via water splitting," *Science*, vol. 280, no. 5362, pp. 425–427, 1998.
- [6] E. Aharon-Shalom and A. Heller, "Efficient p-InP (Rh-H alloy) and p-InP (Re-Halloy) hydrogen evolving photocathodes," *Journal of the Electrochemical Society*, vol. 129, pp. 2865–2866, 1982.
- [7] F. Ren, X. D. Zhou, Y. C. Liu et al., "Fabrication and properties of TiO₂ nanofilms on different substrates by a novel and universal method of Ti-ion implantation and subsequent annealing," *Nanotechnology*, vol. 24, no. 25, Article ID 255603, 2013.
- [8] T. Ohsaka, F. Izumi, Y. Fujiki, and J. Raman, "Raman spectrum of anatase, TiO₂," *Journal of Raman Spectroscopy*, vol. 7, pp. 321–324, 1978.
- [9] A. Chaves, R. S. Katiyar, and S. P. S. Porto, "Coupled modes with A1 symmetry in tetragonal BaTiO₃," *Physical Review B*, vol. 10, no. 8, pp. 3522–3533, 1974.
- [10] V. Swamy, B. C. Muddle, and Q. Dai, "Size-dependent modifications of the Raman spectrum of rutile TiO₂," *Applied Physics Letters*, vol. 89, no. 16, Article ID 163118, 2006.
- [11] W. F. Zhang, Y. L. He, M. S. Zhang, Z. Yin, and Q. Chen, "Raman scattering study on anatase TiO₂ nanocrystals," *Journal of Physics D: Applied Physics*, vol. 33, no. 8, pp. 912–916, 2000.
- [12] S. P. S. Porto, P. A. Fleury, and T. C. Damen, "Raman spectra of TiO₂, MgF₂, ZnF₂, FeF₂, and MnF₂," *Physical Review*, vol. 154, no. 2, pp. 522–526, 1967.
- [13] J. Y. Cao, Y. J. Zhang, L. Q. Liu, and J. H. Ye, "A p-type Cr-doped TiO₂ photo-electrode for photo-reduction," *Chemical Communications*, vol. 49, no. 33, pp. 3440–3442, 2013.

Research Article

Equivalent Circuit Analysis of Photovoltaic-Thermoelectric Hybrid Device with Different TE Module Structure

Haijun Chen,¹ Ning Wang,^{1,2} and Hongcai He¹

¹ State Key Laboratory of Electronic Thin Films and Integrated Devices and School of Microelectronics and Solid-State Electronics, University of Electronic Science and Technology of China, Chengdu 610054, China

² Institute of Electronic and Information Engineering, University of Electronic Science and Technology of China, Dongguan 523808, China

Correspondence should be addressed to Ning Wang; ning.wang@uestc.edu.cn

Received 14 March 2014; Accepted 14 April 2014; Published 7 May 2014

Academic Editor: Shaohua Shen

Copyright © 2014 Haijun Chen et al. This is an open access article distributed under the Creative Commons Attribution License, which permits unrestricted use, distribution, and reproduction in any medium, provided the original work is properly cited.

Combining two different types of solar cells with different absorption bands into a hybrid cell is a very useful method to improve the utilization efficiency of solar energy. The experimental data of dye-sensitized solar cells (DSSCs) and thermoelectric generators (TEG) was simulated by equivalent circuit method, and some parameters of DSSCs were obtained. Then, the equivalent circuit model with the obtained parameters was used to optimize the structure design of photovoltaic- (PV-) thermoelectric (TE) hybrid devices. The output power (P_{out}) first increases to a maximum and then decreases by increasing the TE prism size, and a smaller spacing between p-type prism and n-type prism of a TE p-n junction causes a higher output power of TEG and hybrid device. When the spacing between TE prisms is 15 μm and the optimal base side length of TE prism is 40 μm , the maximum theoretical efficiency reaches 24.6% according to the equivalent circuit analysis. This work would give some enlightenment for the development of high-performance PV-TE hybrid devices.

1. Introduction

Dye-sensitized solar cells (DSSCs) have been widely studied since reported by O'Regan and Grätzel in 1991 [1]. They were considered as an alternative to conventional solar cells due to their low cost and high theoretical conversion efficiency [2, 3]. In a DSSC, a mesoporous semiconductor film is sensitized with organic dye molecules which can absorb sunlight and generate excited electrons. However, typical DSSCs only absorb part of visible and near-infrared light [4] and unabsorbed sunlight wastes as heat, which is one of the main causes of the low experimental conversion efficiency of DSSCs.

In order to improve the conversion efficiency, it may be an effective method to combine two different DSSCs with different range of light absorption into a hybrid cell. Nattestad et al. proposed a novel p-DSSC/n-DSSC hybrid cell, which realized a 2.42% conversion efficiency [5]. Yanagida et al. prepared DSSC (N719 dye)/DSSC (black dye) hybrid cells with a power

conversion efficiency of 10.6% [6]. However, the research that two DSSCs were integrated did not achieve a satisfying high conversion efficiency. Even if for the integrated DSSCs, a considerable part of the sunlight was unabsorbed and converted into heat, so the waste heat utilization of the solar cells should be the key to improve the solar energy utilization efficiency. Actually, our previous work [7] reported a novel method to improve the solar energy conversion efficiency, which is to combine a transparent DSSC, a solar selective absorber (SSA), and a thermoelectric generator (TEG) into a hybrid device, and the novel photovoltaic-thermoelectric (PV-TE) hybrid device achieved a high conversion efficiency of 13.8% [7]. However, the problem of matching between the output current or voltage of DSSC and TEG was not taken into account, so the conversion efficiency of PV-TE hybrid device did not reach the best. In this work, the photovoltaic-thermoelectric hybrid device is analyzed with an equivalent circuit method. The equivalent circuit method has often been used to analyze solar cells [8] as well as to evaluate DSSCs

[9–11]. The relation between the conversion efficiency of the hybrid device and the internal structure of TE module is calculated based on equivalent circuit models.

2. Modeling of Equivalent Circuit for DSSCs and TE Modules

2.1. Modeling of Equivalent Circuit for DSSCs. This work analyzed the DSSCs by using an equivalent circuit of a one-diode model shown in Figure 1(a) as described in previous reports [11, 12], and the equation of the equivalent circuit is written as follows [12]:

$$I = I_{\text{ph}} - I_0 \left[\exp \left(q \frac{V + IR_s}{nkT} \right) - 1 \right] - \frac{V + IR_s}{R_{\text{sh}}}, \quad (1)$$

where I_{ph} is the photocurrent, I_0 is the initial current, R_s is the series resistance, R_{sh} is the parallel resistance, n is the diode factor, q is the elementary electric charge, k is the Boltzmann constant, and T is the temperature.

The existing experimental data [7] (AM 1.5 G, 100 mW cm⁻²) as the scattered small circles in Figure 2(a) are fitted by using formula (1) and least square method, to calculate some parameters of DSSC, and the fitting curve is shown as the solid line in Figure 2(a). Through the simulation, the values of I_0 , I_{ph} , R_s , R_{sh} , and n for the DSSC are obtained as 20.16 pA, 1.296 mA, 32.08 Ω, 7500 Ω, and 1.427, respectively, which will be necessary for the subsequent analysis of hybrid devices.

2.2. Modeling of Equivalent Circuit for TE Modules. A thermoelectric generator (TEG) with simple structure can be regarded as a steady voltage source in series with internal resistance [13, 14]. The equivalent circuit of the TEG was shown in Figure 1(b). The output current (I) and the resistance of the TE generator ($R_{s\text{TE}}$) could be calculated using the following [13]:

$$I = \frac{\alpha N (T_h - T_c) - V}{R_{s\text{TE}}}, \quad (2)$$

$$R_{s\text{TE}} = N \times \left(\frac{L_p}{A_p \sigma_p} + \frac{L_n}{A_n \sigma_n} \right), \quad (3)$$

where α is the Seebeck coefficient, T_h is the hot-side temperature, T_c is the cold-side temperature, $R_{s\text{TE}}$ is the thermoelectric material resistance, L_p , A_p , L_n , and A_n , respectively, represent the length and the area of n-type thermoelectric material and the p-type thermoelectric material, σ_p and σ_n are the conductivity of n-type thermoelectric material and p-type thermoelectric material, respectively, and N is the number of p-n junctions in TEG. All the TE p-n junctions are square prisms in the same size as shown in Figure 3; that is, $L_p = L_n = L$ and $A_p = A_n = A = a^2$, where a is the base side length of p-type prism or n-type prism in a p-n junction. Then, (3) can be simplified into (4). Consider

$$R_{s\text{TE}} = N \times \frac{L}{a^2} \left(\frac{1}{\sigma_p} + \frac{1}{\sigma_n} \right). \quad (4)$$

Here, the n-type and the p-type thermoelectric material stay the same; namely, σ_p and σ_n remain unchanged, so (4) can be further simplified to be as follows:

$$R_{s\text{TE}} = \frac{2NL}{a^2 \sigma_e}, \quad (5)$$

where σ_e is defined as effective conductivity according to the following:

$$\frac{1}{\sigma_e} = \frac{1}{\sigma_p} + \frac{1}{\sigma_n}. \quad (6)$$

Equations (2) and (4) are used to fit the existing experimental data by least square method to calculate some parameters of TEG as follows: $\sigma_e = 5.25 * 10^4 \text{ Sm}^{-1}$ and $\alpha = 0.222 \text{ mV K}^{-1}$, which will be necessary for the subsequent analysis of hybrid devices. The J - V curves of both experimental and fitting data are shown in Figure 2(b). The fitting curve is slightly higher than the experimental curve for the reason that the fitting calculation reckons without contact resistance of the TE modules.

2.3. Equivalent Circuit Analysis of PV-TE Hybrid Devices.

In the hybrid device, the DSSC and TEG are connected in series. The equivalent circuit of the hybrid device is shown in Figure 1(c). According to the nature of the series, the current and the voltage in the hybrid device comply with the following formula:

$$\begin{aligned} I &= I_{\text{DSSC}} = I_{\text{TE}}, \\ V &= V_{\text{DSSC}} + V_{\text{TE}}, \end{aligned} \quad (7)$$

where I_{DSSC} and I_{TE} are the output current through the DSSC and TEG, respectively, and V_{DSSC} and V_{TEG} are the output voltage of the DSSC and TEG, respectively.

The I - V relationship of the hybrid device can be expressed as (8), which can be obtained by simultaneous equations (1), (2), (4), (5), and (6). Consider

$$I = I_{\text{ph}} - I_0 \left[\exp \left(q \frac{V - \alpha \Delta T + IR}{nkT} \right) - 1 \right] - \frac{V - \alpha \Delta T + IR}{R_{\text{sh}}}, \quad (8)$$

where $\Delta T = T_h - T_c$ and $R = R_s + R_{s\text{TE}}$.

Figure 2(c) shows the J - V curves of the experimental and the fitting results of the PV-TE hybrid device, where fitting calculation ignores the wire resistance and contact resistance, and thus the fitting short-circuit current is slightly larger than the experimental result.

3. Improvement of PV-TE Hybrid Device with Different TE Module Structure

As for the PV-TE hybrid devices, it is difficult to improve the efficiency of DSSC and the performance of the TE materials. Relatively, changing the structure of TE modules is easy to implement. The effect of the size of the TE modules on the efficiency of the hybrid device is analyzed on the basis of the

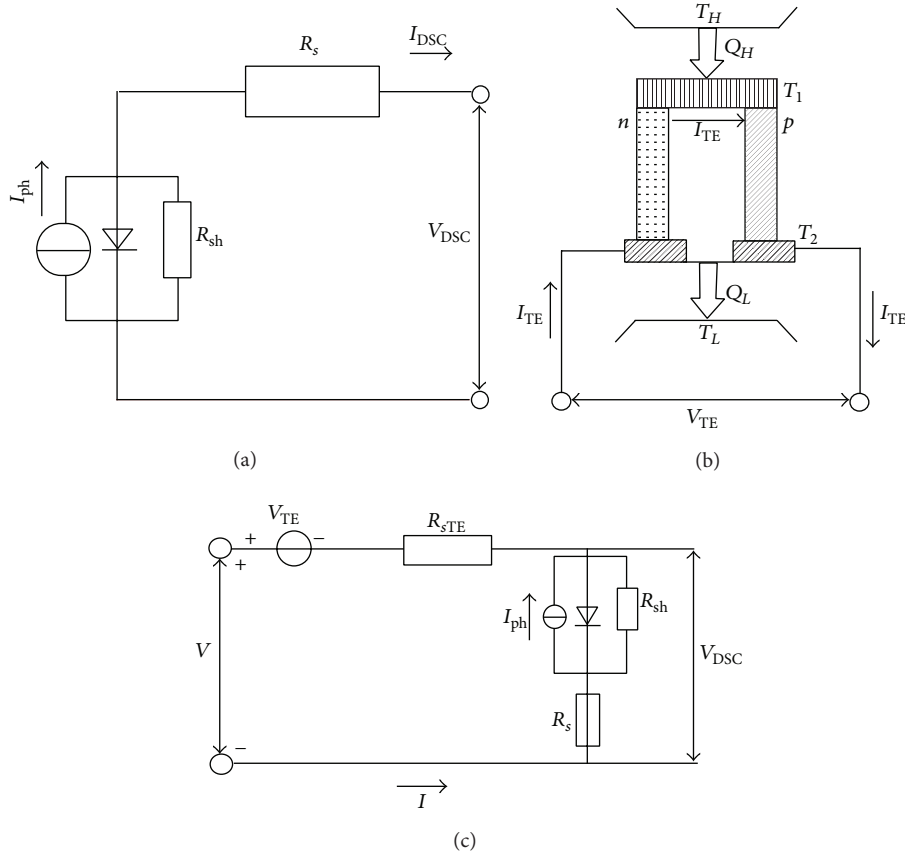


FIGURE 1: Equivalent circuit of (a) single DSSC, (b) single TE, (c) series DSSC, and TE hybrid device.

above calculated results, to determine the best size of the TE modules. The results of calculation can greatly facilitate the experimental procedure.

The above calculation is to fit the experimental data, which verified the feasibility of the calculation method and determined some parameters required in the optimization process. The following optimization calculation assumes that the temperature difference (ΔT) between the two sides of TEG is fixed at 6 K with the same effective gross lighting area. The optimization calculation is to change the output properties of TEG by changing the size of TE modules and to better match the outputs of DSSC. Figure 3 shows the top view of the TE p-n junctions array. The number of p-n junctions changes with the TE p-n junction's sectional area and spacing between p-type prism and n-type prism in a TE p-n junction prism, which can be expressed as follows:

$$N = \left[\text{int} \left(\frac{\sqrt{S} - d}{a + d} \right) \right]^2, \quad (9)$$

where S is the effective area of TEG (here, it is 6.25 mm^2), a is the base side length of TE prism, and d is the spacing between p-type prism and n-type prism of a TE p-n junction, as shown in Figure 3. When a or d of TE p-n junction decreased and the total effective area of TEG remains unchanged, the number of p-n junctions increases. As a result, the output

power of TEG increases, but it is also accompanied with the internal resistance of TEG increasing, which would decrease the TEG's short-circuit current. The structure for the best performance of each component may not be consistent with that for the optimal efficiency of the whole hybrid device, which means that it is infeasible to get an optimal hybrid cell by simply combining an optimal DSSC and an optimal TEG. Comprehensive evaluation of these two factors is necessary to find an optimal solution of the area and space of TE p-n junctions and, consequently, to obtain the optimal properties of the PV-TE hybrid devices. It is possible to further improve the efficiency of the PV-TE hybrid devices in our previous work as reported in [7] by optimizing the design of internal structure parameters in the TE modules to make a good match between the outputs of PV cells and TEG.

A series model of the PV-TE hybrid devices is designed as shown in Figure 1(c), in accordance with our previous experimental structure of hybrid devices [7]. Figure 4 shows the effects of internal structure parameters in the TE modules on the output power (P_{out}) of hybrid cell with a limited total effective area. The output power (P_{out}) first increases to a maximum and then decreases by increasing the TE prism size a . Figure 5 shows the J - V curves of TEG, DSSC, and hybrid cell under simulated AM 1.5 solar spectrum irradiation at 100 mW cm^{-2} . When d is $30 \mu\text{m}$, the optimal TE prism size a is $42 \mu\text{m}$ and the maximum output power is 1.185 mW with

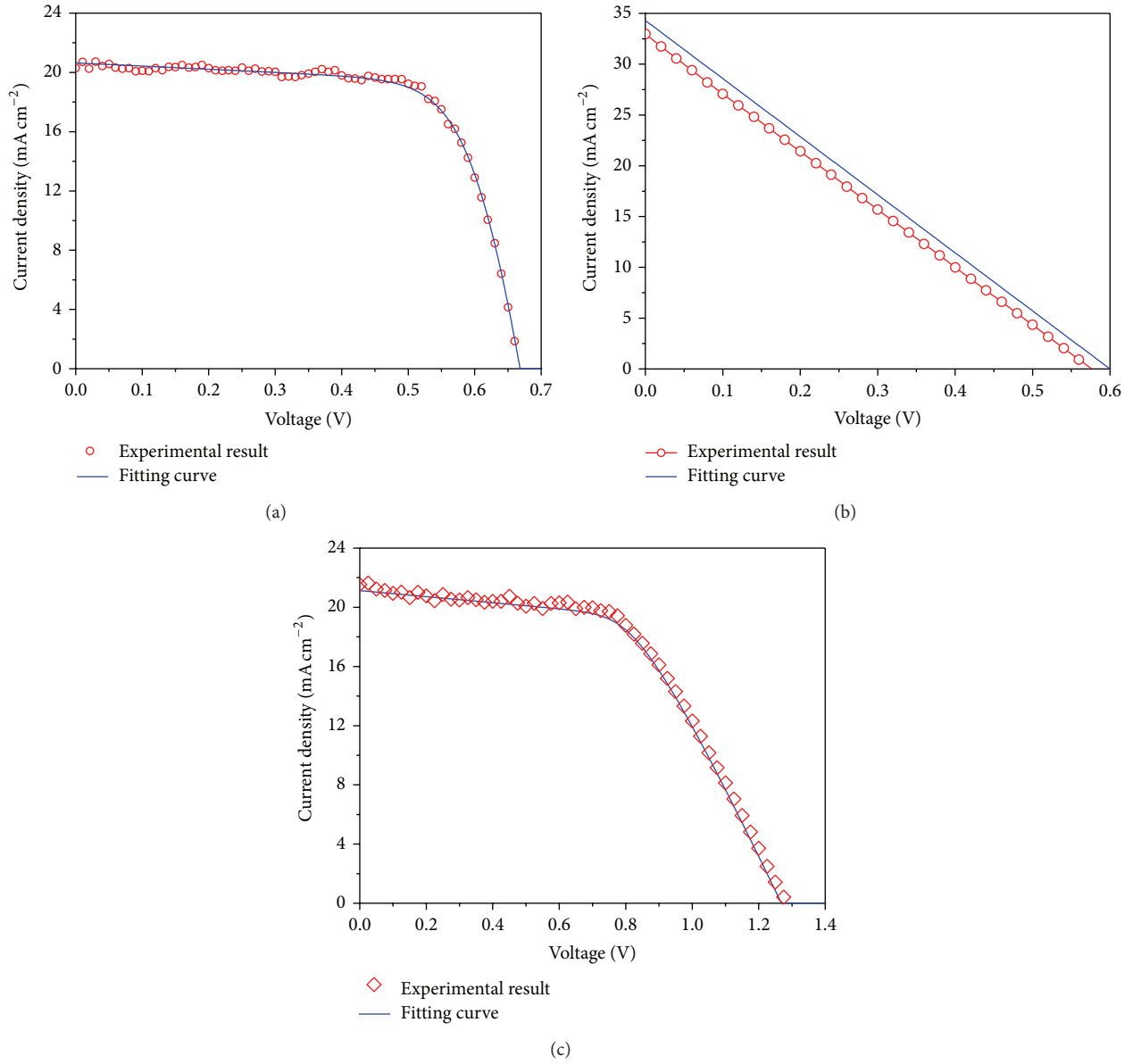


FIGURE 2: The experimental and fitting J - V curves of (a) single DSSC, (b) single TE, (c) series DSSC, and TE hybrid device.

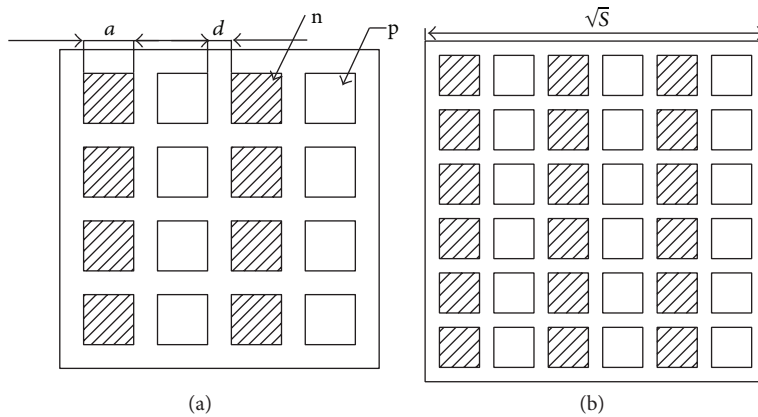


FIGURE 3: The top view of the TE p-n junctions array schematic diagram.

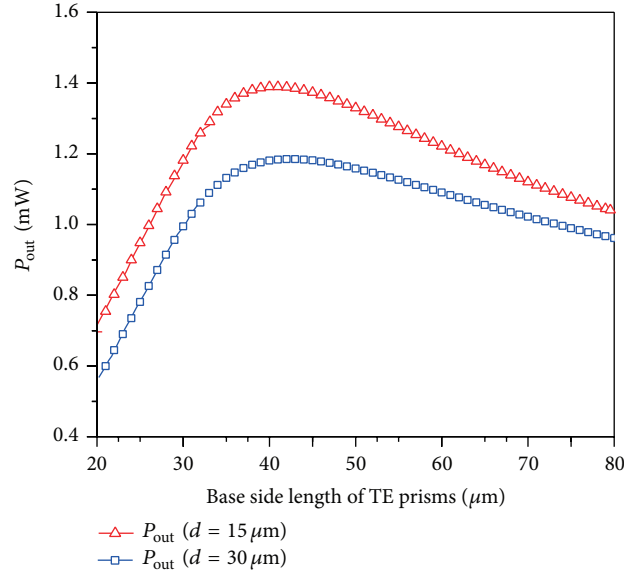


FIGURE 4: The effects of internal structure parameters (a and d) in the TE modules on the output power of hybrid device.

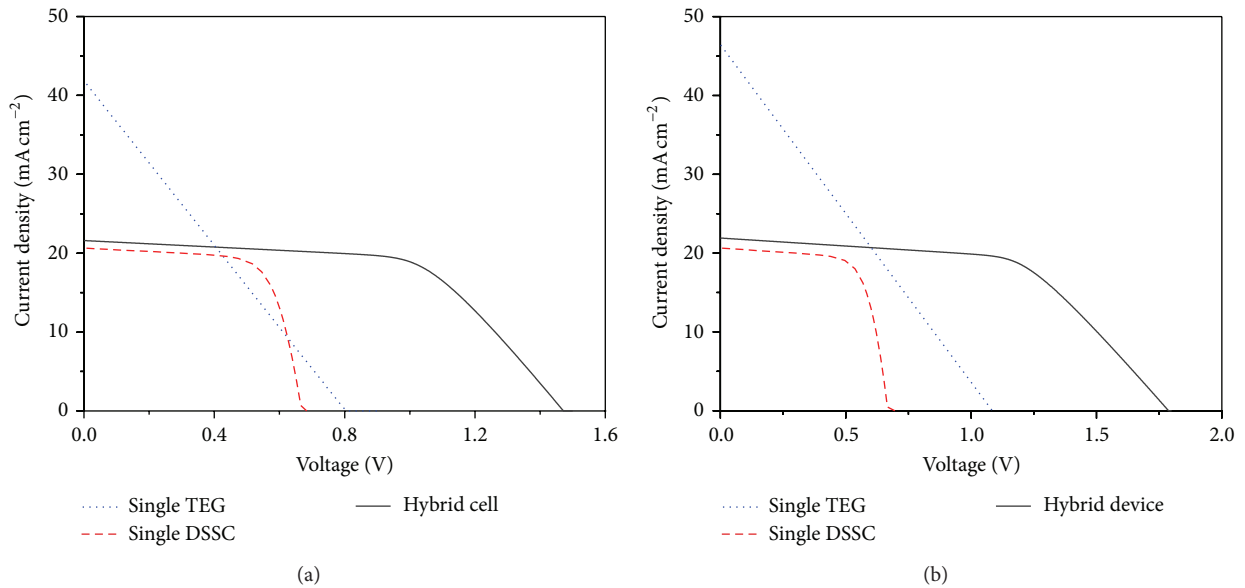


FIGURE 5: The J - V curves of TEG, DSSC, and hybrid device under simulated AM 1.5 solar spectrum irradiation at 100 mW cm^{-2} with (a) $d = 15 \mu\text{m}$ and (b) $d = 30 \mu\text{m}$.

a corresponding photoelectric conversion efficiency of the PV-TE hybrid device 18.96% as shown in Figure 5(a). This result is better than our previous experimental result [7]. If d is reduced to $15 \mu\text{m}$, the optimum a is $40 \mu\text{m}$ and the optimum output power reaches 1.389 mW with the corresponding efficiency 24.6% as shown in Figure 5(b), which is higher than that of the hybrid device with $d = 30 \mu\text{m}$. When d decreases from $30 \mu\text{m}$ to $15 \mu\text{m}$, the TEG can accommodate more TE p-n junctions, which converts more thermal energy into electric energy resulting in a higher efficiency. It can be expected that a smaller d would cause a higher output power of TEG, but it would increase the difficulty of processing.

4. Conclusions

In summary, the photovoltaic-thermoelectric hybrid device is analyzed by the equivalent circuit method, and the internal structure size effect of TE modules on the properties of hybrid devices is investigated. Our preliminary simulation results demonstrate that the PV-TE hybrid device is anticipated for a much higher solar energy utilization efficiency than our previously reported experimental results by optimizing internal structure sizes of TE modules. When the spacing between TE prisms is $15 \mu\text{m}$ and the optimal base side length of TE prism is $40 \mu\text{m}$, the maximum theoretical efficiency reaches

24.6% according to the equivalent circuit analysis. This work gives some good enlightenment for the development of high-performance PV-TE hybrid devices. Meanwhile, this work fixes the temperature difference between the two sides of TEG and reckons without contact resistance of the TE modules in order to simplify the calculation, so there is still considerable room for further improvement of the hybrid devices and more efforts should be made to the simulational and experimental research on the high-performance PV-TE hybrid system.

Conflict of Interests

The authors declare that they have no conflict of interests regarding the publication of this paper.

Acknowledgments

This work was supported by Natural Science Foundation of China (nos. 51272035, 51272037, and 51362026), International Cooperation MOST-JST Program Fund (no. 2010DFA61410), the Project of International Cooperation of the Ministry of Science and Technology of China (no. 2011DFA50530), and Scientific Research Project of Guangdong (no. 2012B091000015).

References

- [1] B. O'Regan and M. Grätzel, "A low-cost, high-efficiency solar cell based on dye-sensitized colloidal TiO₂ films," *Nature*, vol. 353, no. 6346, pp. 737–740, 1991.
- [2] A. Hagfeldt, G. Boschloo, L. Sun, L. Kloo, and H. Pettersson, "Dye-sensitized solar cells," *Chemical Reviews*, vol. 110, no. 11, pp. 6595–6663, 2010.
- [3] H. Lin, X. Li, Y. Liu, and J. Li, "Progresses in dye-sensitized solar cells," *Materials Science and Engineering B: Solid-State Materials for Advanced Technology*, vol. 161, no. 1–3, pp. 2–7, 2009.
- [4] P. Liska, K. R. Thampi, M. Grätzel et al., "Nanocrystalline dye-sensitized solar cell/copper indium gallium selenide thin-film tandem showing greater than 15% conversion efficiency," *Applied Physics Letters*, vol. 88, no. 20, Article ID 203103, 2006.
- [5] A. Nattestad, A. J. Mozer, M. K. R. Fischer et al., "Highly efficient photocathodes for dye-sensitized tandem solar cells," *Nature Materials*, vol. 9, no. 1, pp. 31–35, 2010.
- [6] M. Yanagida, N. Onozawa-Komatsuzaki, M. Kurashige, K. Sayama, and H. Sugihara, "Optimization of tandem-structured dye-sensitized solar cell," *Solar Energy Materials and Solar Cells*, vol. 94, no. 2, pp. 297–302, 2010.
- [7] N. Wang, L. Han, H. He, N.-H. Park, and K. Koumoto, "A novel high-performance photovoltaic-thermoelectric hybrid device," *Energy and Environmental Science*, vol. 4, no. 9, pp. 3676–3679, 2011.
- [8] A. Amine, Y. Mir, and M. Zazoui, "Modelling of dual-junction solar cells including tunnel junction," *Advances in Condensed Matter Physics*, vol. 2013, Article ID 546362, 5 pages, 2013.
- [9] L. Han, N. Koide, Y. Chiba, A. Islam, and T. Mitate, "Modeling of an equivalent circuit for dye-sensitized solar cells: improvement of efficiency of dye-sensitized solar cells by reducing internal resistance," *Comptes Rendus Chimie*, vol. 9, no. 5–6, pp. 645–651, 2006.
- [10] M. R. Mitroi, L. Fara, and M. L. Ciurea, "Numerical procedure for optimizing dye-sensitized solar cells," *Journal of Nanomaterials*, vol. 2014, Article ID 378981, 6 pages, 2014.
- [11] M. Murayama and T. Mori, "Novel tandem cell structure of dye-sensitized solar cell for improvement in photocurrent," *Thin Solid Films*, vol. 516, no. 9, pp. 2716–2722, 2008.
- [12] M. Murayama and T. Mori, "Evaluation of treatment effects for high-performance dye-sensitized solar cells using equivalent circuit analysis," *Thin Solid Films*, vol. 509, no. 1–2, pp. 123–126, 2006.
- [13] B. S. Yilbas and A. Z. Sahin, "Thermoelectric device and optimum external load parameter and slenderness ratio," *Energy*, vol. 35, no. 12, pp. 5380–5384, 2010.
- [14] D. Kraemer, B. Poudel, H.-P. Feng et al., "High-performance flat-panel solar thermoelectric generators with high thermal concentration," *Nature Materials*, vol. 10, no. 7, pp. 532–538, 2011.

Research Article

Improved Composite Gel Electrolyte by Layered Vermiculite for Quasi-Solid-State Dye-Sensitized Solar Cells

Hongcai He,¹ Shuangshuang Ren,¹ Deting Kong,¹ and Ning Wang^{1,2}

¹ State Key Laboratory of Electronic Thin Films and Integrated Devices and School of Microelectronics and Solid-State Electronics, University of Electronic Science and Technology of China, Chengdu 610054, China

² Institute of Electronic and Information Engineering, University of Electronic Science and Technology of China, Dongguan 523808, China

Correspondence should be addressed to Hongcai He; hehc@uestc.edu.cn

Received 12 March 2014; Accepted 30 March 2014; Published 22 April 2014

Academic Editor: Ke Sun

Copyright © 2014 Hongcai He et al. This is an open access article distributed under the Creative Commons Attribution License, which permits unrestricted use, distribution, and reproduction in any medium, provided the original work is properly cited.

A composite quasisolid electrolyte is prepared by adding a layered vermiculite (VMT) into the iodide/triiodide electrolyte including 4-tert-butylpyridine, which obviously improves the photovoltaic properties of quasisolid dye-sensitized solar cells (DSSCs). When adding 6 wt% VMT, the maximum photovoltaic conversion efficiency of 3.89% is obtained, which reaches more than two times greater than that without VMT. This enhancement effect is primarily explained by studying the Nyquist spectra, dark currents, and photovoltaic conversion efficiency.

1. Introduction

Dye-sensitized solar cells (DSSCs) have attracted an ever-increasing attention since reported by O'Regan and Grätzel in 1991 [1] for its low-cost, environmental friendliness, and potential high conversion efficiency, which was considered to be a strong contender of the next-generation solar cells in the near future. Generally, a mainstream DSSC is composed of three main parts: a dye-adsorbed porous nanocrystalline TiO₂ film supported on a transparent conducting glass as the photoanode, an organic liquid electrolyte, essentially containing an iodide/triiodide redox couple, and a platinized transparent glass substrate as the counter electrode. These three layers are sandwiched together. Electrolytes play an important role in the DSSCs as the charge exchange medium. The organic liquid electrolyte was commonly used in traditional DSSCs, which is associated with problems such as hermetic sealing of the cell, solvent volatilization and leakage, bad long-term stability, decomposing dye, and corroding Pt electrode.

Recently, many efforts have been made to overcome the above problems of traditional DSSCs with liquid electrolytes, and solid-state and quasi-solid-state DSSCs have been intensely studied with various approaches. Some novel

technologies and materials including p-type semiconductors [2], organic and inorganic holes conductors [3], and polymer gel electrolytes [4, 5] were used in new electrolytes to improve properties. Among them, polymer based quasi-solid-state electrolytes are a very good choice for its high ionic conductivity, long-term stability, good interfacial filling properties, and inhibiting leakage, which commonly have a polymer and ionic liquid electrolytes containing dispersed nanocomponents. Some ceramic nanoparticles such as SiO₂ [6], TiC [7] and TiN [8] were added into ionic liquid-based electrolytes for DSSCs, and an enhanced conversion efficiency was obtained. In our previous work [9, 10], some layered materials such as α -zirconium phosphate and Mg-Al hydrotalcite were added into the iodide/triiodide ionic liquid to prepare quasi-solid-state electrolytes, which obviously improves the photovoltaic properties of quasisolid DSSCs. Vermiculite (VMT) is not only a layered mica-type silicate but is also with a large surface area and strong absorptive capacity and has often been studied for the preparation of composites [11, 12]. In this paper, a new composite gel polymer electrolyte was prepared by adding vermiculite (VMT) powder into iodide-based liquid electrolyte with the addition of 4-tert-butylpyridine (TBP), propylene carbonate (PC), and poly (ethylene oxide) (PEO-600,000).

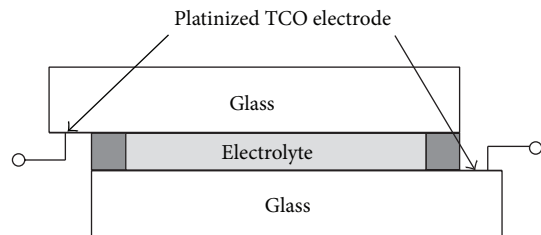


FIGURE 1: Schematic diagram of the experimental thin-layer cell configuration employed for the electrochemical measurements.

The electrochemical properties of the composite electrolyte were analyzed systematically by testing Nyquist diagram, and a typical DSSC was packaged with the new quasi-solid-state composite electrolyte to measure photovoltaic properties.

2. Experimental

2.1. Preparation of VMT and Composite Gel Polymer Electrolyte. The starting VMT was supplied by Bright Mining Co. (Shanghai, China). After VMT was ball-milled for 6 h in the solvent of deionized water, the ultrasonic irradiation method reported by Nguyen et al. [13] was used to prepare the layered vermiculite (VMT) powders.

Then, VMT powders with the contents of 0 wt%, 3 wt%, 6 wt%, 9 wt%, and 12 wt%, relative to the weight of TBP, were added to the iodide-based gel polymer electrolyte prepared according to [14], which contained 0.5 M LiI, 0.05 M I₂, 6 mL PC, 0.5 M TBP, 0.4 g PEO-600,000, and acetonitrile solvent. After stirring strongly for 72 h at 80°C, the composite gel polymer electrolytes including layered VMT were obtained.

2.2. Testing Device and Characterization Method. X-ray diffraction (XRD Rigaku D/max-RB) with CuK α radiation was used for phase analysis of the powders under 40 kV and 30 mA. Scanning electron microscopy (SEM, INSPECTF FEI, Netherlands) was used to observe the micrographs. Simple thin-layer cells were manufactured to measure AC impedance according to [15]. The cell was made up of two identical platinumized TCO-coated glass substrates separated by Surlyn thermal packaging adhesive and filled with the composite electrolyte with VMT additives, as shown in Figure 1. The active area of the electrodes was about 0.16 cm² and the distance between the electrodes was about 25 μ m. Electrochemical impedance spectra (EIS) were obtained by using CHI660c electrochemical analyzer (CH Instrument Co., Ltd. China). Sinusoidal perturbations of 10 mV at frequencies from 0.01 Hz to 100 kHz with zero bias potential were applied on thin-layer cells with a two-electrode mode as shown in Figure 1. In order to study the photovoltaic properties of the DSSCs with the composite electrolytes containing VMT, quasisolid DSSCs were packaged according to the previous published procedures [9, 10] from dye-coated TiO₂ film photoanodes, counterelectrodes (500 nm thick, Pt), and composite gel polymer electrolytes containing VMT. Photovoltaic properties were measured at 100 mW cm⁻² light intensity under AM 1.5 irradiation of xenon lamp, while the

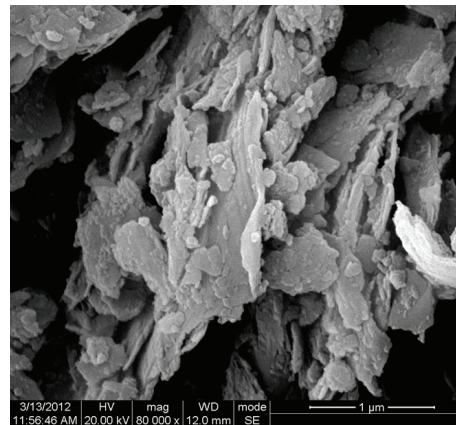


FIGURE 2: SEM micrograph of VMT powder.

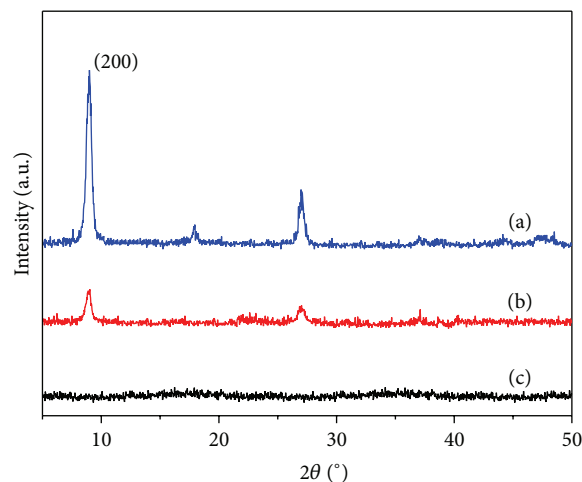


FIGURE 3: X-ray diffraction patterns of (a) VMT powder, (b) the composite electrolyte membrane with 6 wt% VMT, (c) the composite electrolyte membrane with 0 wt% VMT.

dark current density is measured in dark. All measurements were carried out at room temperature.

3. Results and Discussion

3.1. Analysis of VMT Powders. Figure 2 shows a SEM micrograph of VMT powders, and the layered structure with a nanoscale layer thickness can be observed. X-ray diffraction patterns of the prepared VMT powder and composite electrolytes are shown in Figure 3. As shown in Figure 3(a), the prepared VMT powders are well-crystallized with the strongest diffraction peaks at 8.96°, indexed as (200) peak [13]. After 6 wt% VMT additive was mixed into iodine-based PEO electrolyte and coated on the photoanode thin film, the (200) peak was still detected in the obtained electrolyte membrane as shown in Figure 3(b).

3.2. The Influence of VMT on the Conductivity. The Nyquist spectra of thin-layer cells with composite gel iodide-based electrolytes containing different contents of VMT are shown

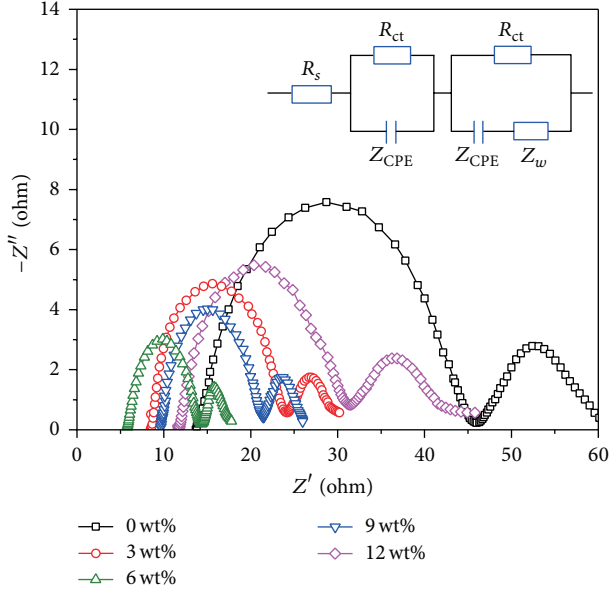


FIGURE 4: Nyquist diagram of thin-layer cells with various contents of VMT and the inset shows the equivalent circuit.

TABLE 1: The results for the R_{ct} and corresponding σ of the iodide-based gel electrolytes with various contents of VMT.

VMT (wt%)	R_{ct} (Ω)	R_s (Ω)	σ (10^{-4} S cm $^{-1}$)
0	32.04	13.69	11.41
3	15.05	9.11	17.15
6	8.35	5.75	27.17
9	13.47	7.85	19.91
12	19.64	11.63	13.44

in Figure 4. The equivalent circuit is shown as the inset of Figure 4. Each curve is composed of two semicircles. The one in the high frequency region represents the charge transfer resistance (R_{ct}) of Pt/electrolyte interface, and the other one in the low frequency region relates to the Warburg impedance (Z_w) [8]. R_s is the ohmic serial resistance and Z_{CPE} is the impedance of electrical double layer. Based on the equivalent circuit, the fitting data of the charge transfer resistance (R_{ct}) and the ohmic serial resistance (R_s) were obtained. Then the ion conductivity of the electrolyte (σ) can be obtained from the equation $\sigma = l/(R_s a)$ [4], where a and l are the active area of the electrodes (here $a = 0.16$ cm 2) and the distance between electrodes (here $l = 0.25$ μ m), respectively. The results for the R_{ct} values and R_s values and corresponding σ values of iodide-based gel electrolytes with various contents of VMT are summarized in Table 1.

As shown in Figure 4 and Table 1, the R_{ct} values and the R_s values of the cells decrease markedly and the corresponding σ values increase with adding VMT up to 6 wt%. Here, VMT as dispersed second phase insulating particles affected drastically the conductivities of composite iodide-based gel electrolytes. Quite a few works [16, 17] reported the effect of dispersed second phase particles on the ionic

TABLE 2: The photovoltaic parameters of the DSSCs with various contents of VMT.

VMT (wt%)	J_{sc} (mA cm $^{-2}$)	V_{oc} (V)	FF	η (%)
0	5.08	0.62	0.54	1.70
3	9.07	0.64	0.53	3.07
6	9.77	0.67	0.59	3.89
9	8.53	0.66	0.55	3.10
12	7.15	0.64	0.53	2.43

conduction. When adding the insulating phase in the ion-conductive phase, ionic conductivity will first increase and then decrease. Nan developed an improved and simple self-consistent effective-medium theory to explain the effect [18]. It has now become widely accepted that the enhancement effect of conductivity is related to creating highly conductive paths along the interfaces between the electrolyte matrix and the second phase grains [18]. The highly conductive paths can be an interfacial layer with high concentrations of defects, a space charge layer, and/or an absorbed water layer. VMT has a layered structure with a large surface area, which means there is enough interface to create conductive paths. When the content of VMT is 6 wt%, the minimum R_{ct} value of 8.35 Ω and the minimum R_s value of 5.75 Ω are obtained, corresponding with the maximum σ value of 27.17×10^{-4} S cm $^{-1}$. While the content of VMT is over 6 wt%, the inert second phase particles directly contact each other to form continuum percolation net clusters, which tends to limit ion movement and decrease the conductivity [17, 18], and, as a result, the R_{ct} values and the R_s value increase and the σ values decrease markedly.

3.3. The Influence of VMT on the Photovoltaic Conversion Efficiency. Figure 5(a) is the J - V curves of thin-layer cells with various VMT contents. The results for short-circuit current density (J_{sc}), open circuit potential (V_{oc}), fill factor (FF), and conversion efficiency (η) of the DSSCs with different additions of VMT are summarized in Table 2. The DSSCs with the electrolytes adding VMT show a higher open circuit potential (V_{oc}) and significantly higher short current density (J_{sc}) than that without adding VMT. V_{oc} and J_{sc} increase first and then decrease with the increase of VMT contents. In order to study the influence of electrolytes with adding various contents of VMT on the above photoelectric properties, the dark current density-voltage curves of the DSSCs with various contents of VMT are shown in Figure 5(b). It can be easily found that the dark current density decreases when adding the VMT. As the content of VMT increases to 6 wt%, the dark current density of the DSSC is suppressed to a minimum and increases quickly as the content of VMT further increases over 6 wt% to 12 wt%.

The change in both V_{oc} and J_{sc} of the DSSCs is related to the dark current density. The enhanced V_{oc} is due to the suppression of the dark current in the TiO $_2$ /electrolyte interface. The fact that the onset of the dark current of DSSCs occurs at the higher forward bias indicates the lower I_3^- reduction rate (k_{et}) [9, 19]. The decrease of I_3^- reduction rate

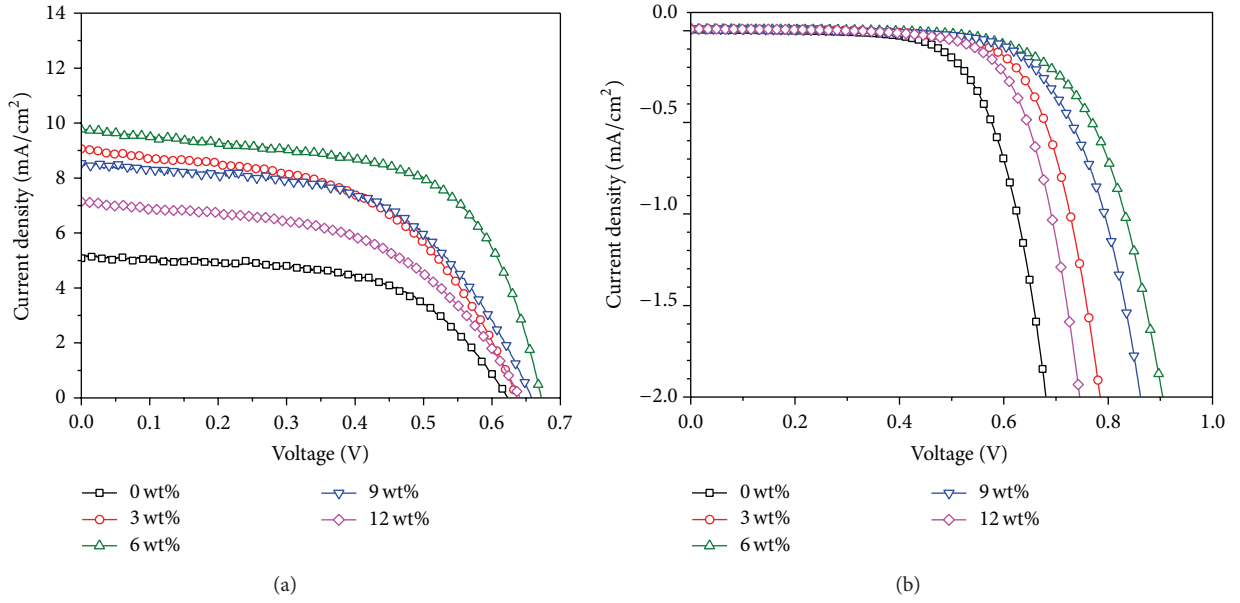


FIGURE 5: The J - V curves of DSSCs with composite electrolytes containing various contents of VMT (a) under simulated AM 1.5 solar spectrum irradiation at 100 mW cm^{-2} ; (b) in the dark.

will lead to an increase of V_{oc} according to the following equation [19]:

$$V_{oc} = \frac{kT}{e} \ln \left(\frac{I_{inj}}{n_{cb} k_{et} [I_3^-]} \right), \quad (1)$$

where I_{inj} , n_{cb} , and k_{et} are the flux of charge originating from sensitized injection related to the electron back transfer rate, the concentration of electrons at the TiO_2 surface, and the rate constants for I_3^- reduction, respectively. As shown in Figure 5(b), the onset of the dark current of DSSCs occurs at 227, 335, 378, 325, and 319 mV with various electrolytes adding 0 wt%, 3 wt%, 6 wt%, 9 wt%, and 12 wt% of VMT, respectively. The higher onset voltage value of the dark current of DSSCs with adding VMT than that without adding VMT reveals that VMT can efficiently suppress the dark reaction to obtain higher V_{oc} . On the other hand, the J_{sc} of DSSCs is also associated with the dark current, which can be given by the equation $J_{sc} = J_{inj} - J_{rec}$, where J_{inj} and J_{rec} are the electron injection current density and the recombination current density, respectively [20]. The electron injection current density should be constant since all the DSSCs have the same electrodes and experimental conditions. The recombination current mainly manifests as the dark current, so the recombination current density has similar variation trend with the dark current density [21]. Consequently J_{sc} increases with the decrease of the dark current density. As a consequence, proper addition of VMT can improve both J_{sc} and V_{oc} of the DSSC, and the best ratio is about 6 wt% of VMT. When the content of VMT is 6 wt%, the conversion efficiency (η) is up to the maximum of 3.89%, which is more than two times greater than that without

adding VMT. While the content of VMT is over 6 wt%, the conversion efficiency (η) decreases quickly.

4. Conclusions

In summary, we prepared a quasi-solid-state composite electrolyte by adding layered vermiculite (VMT) powder into the iodide-based electrolyte including PC, TBP, and PEO-600,000. Electrochemical analysis was done on the DSSCs with various electrolytes adding different contents of VMT. The results showed that VMT as a dispersed second phase insulating particles affected drastically the conductivities of composite electrolytes. The reduction of the dark current density with adding VMT indicated that the J_{sc} and V_{oc} increased with the addition of appropriate amount of VMT, compared to DSSCs without VMT. When the content of VMT reached 6 wt%, the conversion efficiency (η) was maximized to 3.89%, which was more than two times greater than that without addition of the VMT.

Conflict of Interests

The authors declare that there is no conflict of interests regarding the publication of this paper.

Acknowledgments

This work was supported by Natural Science Foundation of China (51272035, 51272037, and 51362026), International Cooperation MOST-JST Program Fund (no. 2010DFA61410), The Project of International Cooperation of the Ministry of Science and Technology of China (no. 2011DFA50530),

and Scientific Research Project of Guangdong (no. 2012B091000015).

References

- [1] B. O'Regan and M. Grätzel, "A low-cost, high-efficiency solar cell based on dye-sensitized colloidal TiO₂ films," *Nature*, vol. 353, no. 6346, pp. 737–740, 1991.
- [2] K. Tennakone, G. K. R. Senadeera, D. B. R. A. De Silva, and I. R. M. Kottegoda, "Highly stable dye-sensitized solid-state solar cell with the semiconductor 4CuBr 3S(C₄H₉)₂ as the hole collector," *Applied Physics Letters*, vol. 77, no. 15, pp. 2367–2369, 2000.
- [3] C. S. Karthikeyan, H. Wietasch, and M. Thelakkat, "Highly efficient solid-state dye-sensitized TiO₂ solar cells using donor-antenna dyes capable of multistep charge-transfer cascades," *Advanced Materials*, vol. 19, no. 8, pp. 1091–1095, 2007.
- [4] X. Chen, Q. Li, J. Zhao et al., "Ionic liquid-tethered nanoparticle/poly(ionic liquid) electrolytes for quasi-solid-state dye-sensitized solar cells," *Journal of Power Sources*, vol. 207, pp. 216–221, 2012.
- [5] P. Wang, S. M. Zakeeruddin, J. E. Moser, M. K. Nazeeruddin, T. Sekiguchi, and M. Grätzel, "A stable quasi-solid-state dye-sensitized solar cell with an amphiphilic ruthenium sensitizer and polymer gel electrolyte," *Nature Materials*, vol. 2, no. 6, pp. 402–407, 2003.
- [6] K.-M. Lee, P.-Y. Chen, C.-P. Lee, and K.-C. Ho, "Binary room-temperature ionic liquids based electrolytes solidified with SiO₂ nanoparticles for dye-sensitized solar cells," *Journal of Power Sources*, vol. 190, no. 2, pp. 573–577, 2009.
- [7] C.-P. Lee, K.-M. Lee, P.-Y. Chen, and K.-C. Ho, "On the addition of conducting ceramic nanoparticles in solvent-free ionic liquid electrolyte for dye-sensitized solar cells," *Solar Energy Materials and Solar Cells*, vol. 93, no. 8, pp. 1411–1416, 2009.
- [8] C.-P. Lee, L.-Y. Lin, R. Vittal, and K.-C. Ho, "Favorable effects of titanium nitride or its thermally treated version in a gel electrolyte for a quasi-solid-state dye-sensitized solar cell," *Journal of Power Sources*, vol. 196, no. 3, pp. 1665–1670, 2011.
- [9] N. Wang, H. Lin, J. Li, and X. Li, "Improved quasi-solid dye-sensitized solar cells by composite ionic liquid electrolyte including layered α -zirconium phosphate," *Applied Physics Letters*, vol. 89, no. 19, Article ID 194104, 2006.
- [10] H. He, J. Zhu, N. Wang, F. Luo, and K. Yang, "Composite gel polymer electrolytes containing layered Mg-Al hydrotalcite for quasi-solid dye-sensitized solar cells," *Journal of the Electrochemical Society*, vol. 161, pp. H17–H20, 2014.
- [11] M. V. Smalley, H. L. M. Hatharasinghe, I. Osborne, J. Swenson, and S. M. King, "Bridging flocculation in vermiculite–PEO mixtures," *Langmuir*, vol. 17, no. 13, pp. 3800–3812, 2001.
- [12] L. Zang, J. Luo, J. Guo, H. Liu, and J. Ru, "Preparation and characterization of poly(ethylene glycol)/organo-vermiculite nanocomposite polymer electrolytes," *Polymer Bulletin*, vol. 65, no. 7, pp. 669–680, 2010.
- [13] A. N. Nguyen, L. Reinert, J. M. Lévêque et al., "Preparation and characterization of micron and submicron-sized vermiculite powders by ultrasonic irradiation," *Applied Clay Science*, vol. 72, pp. 9–17, 2013.
- [14] Y. Ren, Z. Zhang, S. Fang, M. Yang, and S. Cai, "Application of PEO based gel network polymer electrolytes in dye-sensitized photoelectrochemical cells," *Solar Energy Materials and Solar Cells*, vol. 71, no. 2, pp. 253–259, 2002.
- [15] N. Papageorgiou, W. F. Maier, and M. Grätzel, "An iodine/triiodide reduction electrocatalyst for aqueous and organic media," *Journal of the Electrochemical Society*, vol. 144, no. 3, pp. 876–884, 1997.
- [16] C. C. Liang, "Conduction characteristics of the lithium iodide–aluminum oxide solid electrolytes," *Journal of the Electrochemical Society*, vol. 120, no. 10, pp. 1289–1292, 1973.
- [17] C.-W. Nan, L. Fan, Y. Lin, and Q. Cai, "Enhanced ionic conductivity of polymer electrolytes containing nanocomposite SiO₂ particles," *Physical Review Letters*, vol. 91, no. 26, pp. 2661041–2661044, 2003.
- [18] C.-W. Nan, "Physics of inhomogeneous inorganic materials," *Progress in Materials Science*, vol. 37, no. 1, pp. 1–116, 1993.
- [19] M. K. Nazeeruddin, A. Kay, I. Rodicio et al., "Conversion of light to electricity by cis-X₂bis(2,2'-bipyridyl-4,4'-dicarboxylate)ruthenium(II) charge-transfer sensitizers (X = Cl-, Br-, I-, CN-, and SCN-) on nanocrystalline TiO₂ electrodes," *Journal of the American Chemical Society*, vol. 115, no. 14, pp. 6382–6390, 1993.
- [20] L. Y. Chen and Y. T. Yin, "The influence of length of one-dimensional photoanode on the performance of dye-sensitized solar cells," *Journal of Materials Chemistry*, vol. 22, no. 47, pp. 24591–24596, 2012.
- [21] K. Guo, M. Li, X. Fang et al., "Preparation and enhanced properties of dye-sensitized solar cells by surface plasmon resonance of Ag nanoparticles in nanocomposite photoanode," *Journal of Power Sources*, vol. 230, pp. 155–160, 2013.

Research Article

Photocatalytic Reduction of CO₂ to Methane on Pt/TiO₂ Nanosheet Porous Film

Li Qiu-ye, Zong Lan-lan, Li Chen, Cao Yu-hui, Wang Xiao-dong, and Yang Jian-jun

Key Laboratory for Special Functional Materials, Henan University, Kaifeng 475004, China

Correspondence should be addressed to Li Qiu-ye; qiuyeli@henu.edu.cn

Received 13 March 2014; Accepted 24 March 2014; Published 13 April 2014

Academic Editor: Haimin Zhang

Copyright © 2014 Li Qiu-ye et al. This is an open access article distributed under the Creative Commons Attribution License, which permits unrestricted use, distribution, and reproduction in any medium, provided the original work is properly cited.

Anatase TiO₂ nanosheet porous films were prepared by calcination of the orthorhombic titanic acid films at 400°C. They showed an excellent photocatalytic activity for CO₂ photoreduction to methane, which should be related to their special porous structure and large Brunauer-Emmett-Teller (BET) surface area. In order to further improve the photocatalytic activity, Pt nanoparticles were loaded uniformly with the average size of 3–4 nm on TiO₂ porous films by the photoreduction method. It was found that the loading of Pt expanded the light absorption ability of the porous film and improved the transformation efficiency of CO₂ to methane. The conversion yield of CO₂ to methane on Pt/TiO₂ film reached 20.51 ppm/h·cm². The Pt/TiO₂ nanosheet porous film was characterized by means of X-ray diffraction (XRD), scanning electron microscopy (SEM), transmission electron microscope (TEM), and ultraviolet-visible light diffuse reflectance spectra (UV-vis DRS). Moreover, the transient photocurrent-time curves showed that the Pt/TiO₂ nanosheet porous film exhibited higher photocurrent, indicating that the higher separation efficiency of the photogenerated charge carriers was achieved.

1. Introduction

Fossil fuels are our primary source of energy. Unfortunately, CO₂ emissions generated in using these fuels have drastically increased in atmosphere in recent years, and the fast-growing CO₂ leads to climate change, which has become one of the greatest threats of environmental problems. It is very urgent to reduce the accumulation of CO₂ in the atmosphere. In general, the photocatalytic reduction of CO₂ is a possible avenue to convert CO₂ into hydrocarbon fuels, because reducing the amount of CO₂ will not only meet the purpose of environmental protection but also provide raw materials for chemical industry. This process utilizes ultraviolet (UV) and/or visible light as the excitation source for semiconductor catalysts, and the photoexcited electrons reduce CO₂ with H₂O on the catalyst surface and form energy-bearing products such as carbon monoxide (CO), methane (CH₄), methanol (CH₃OH), formaldehyde (HCHO), and formic acid (HCOOH) [1].

Many researchers [2] have shown that CO₂ could be reduced by water vapor or solvent with photocatalysts. Among these photocatalysts, TiO₂ or TiO₂-based materials

may promote the photoreduction of CO₂ to useful organic compounds [3–9]. Moreover, TiO₂ is one of the most intensively studied and widely used photocatalysts as a result of a number of advantageous features such as low cost, relatively high catalytic activity, low toxicity, and high chemical stability [10–12]. Especially modification of TiO₂ through noble metal supporting is increasingly being considered for maximising its photocatalytic efficiency. These metals may facilitate electron-hole separation and promote interfacial electron transfer or they may decrease the TiO₂ band gap, which benefits electrons transfer from the valence band to the conduction band, facilitating the formation of oxidative species. The TiO₂-based nanomaterials, especially the titanate network films, obtained by the hydrothermal method often have large BET surface area and strong adsorption ability [13]. It is noticeable that the surface network structure of the film can enhance the adsorption of the reactive species and absorption efficiency of the incident light and further improve the photocatalytic activity [14–16].

Herein, anatase TiO₂ nanosheet porous films were obtained by calcination of the orthorhombic titanic acid films at 400°C. Because the surface of titanic acid consists of

the porous network structure [17], the obtained anatase TiO_2 has stronger absorption ability and higher photocatalytic performance compared with the film prepared by sol-gel method in the same condition. Moreover, it is noticeable that the porous structure of the film also can enhance the adsorption of the reactive species and absorption efficiency of the incident light [14–16]. In order to further improve the photocatalytic activity, Pt nanoparticles were loaded on the surface of it as an electron trapper to capture the photogenerated electrons by the photoreduction method. The relationship between the morphology, structure, and their photocatalytic activity was investigated in detail.

2. Experimental

2.1. Preparation of TiO_2 and Pt- TiO_2 Nanosheet Porous Films.

The precursor for preparing TiO_2 porous film was titanate nanotube (TAN) porous film, and the typical preparing process of TAN film was as follows: a Ti thin foil with a size of $2 \times 4 \text{ cm}^2$ was put into 100 mL of 10 M NaOH aqueous solution, followed by the hydrothermal treatment in a 120 mL Teflon-lined autoclave at 120°C for 24 h. After cooling down, the obtained titanate network film was washed with distilled water several times and then immersed in a 0.1 M HCl aqueous solution overnight. After that, the product was washed several times with water and then dried in the N_2 stream.

TiO_2 nanosheet porous films were prepared by calcination of TAN films at 400°C for 4 h in air. Then, Pt nanoparticles were loaded by the photoreduction method in H_2PtCl_6 ethanol solution. The solution was illuminated under UV light for 1 h. After that, the sample was washed with deionized water and dried. For a comparison, a TiO_2 film prepared by a sol-gel method was used as a reference [18]; the sample was denoted by R- TiO_2 .

2.2. Characterization. UV-vis diffuse reflectance spectra (DRS) were obtained on a Shimadzu U-3010 spectrometer, using BaSO_4 as a reference. X-ray diffraction (XRD) patterns were measured on an X'Pert Philips diffractometer (Cu $K\alpha$ radiation; 2θ range $5\text{--}90^\circ$, step size 0.08° , accelerating voltage 40 kV, and applied current 40 mA). The particle size and surface morphology of the samples were observed using a scanning electron microscope (SEM) (JSM-7100F, JEOL Co., Japan) and transmission electron microscope (TEM) (JEM-2010, JEOL Co., Japan).

2.3. Photoelectrochemical Measurements. The transient photocurrent-time (I - t) experiments were conducted using a conventional three-electrode system on the electrochemical analyzer (IM6ex, Germany). The photocatalyst film served as the working electrode, and a Pt meshwork and an Ag/AgCl electrode (SCE) acted as the counter electrode and reference electrode, respectively. The electrolyte was Na_2SO_4 with a concentration of $0.5 \text{ mol}\cdot\text{L}^{-1}$.

2.4. Photocatalytic Activity Evaluation. The photocatalytic reduction of CO_2 was conducted in a flat closed reactor

with the inner capacity of 358 mL containing 20 mL 0.1 mol/L KHCO_3 solution. The prepared TiO_2 nanosheet porous film was located in the center of the reactor and then the ultrapure gaseous CO_2 and water vapor was flowed through the reactor for 2 h to achieve the adsorption-desorption equilibrium. Before illumination, the reactor was sealed. The light source was the high pressure Hg lamp with 300 W, and the intensity of the incident light was measured to be $10.4 \text{ mW}/\text{cm}^2$. The photocatalytic reaction was typically performed at room temperature for 6 h. The products were measured by gas chromatography (GC). The comparison tests consisted of a reaction under light without the catalysts and a reaction in dark with the catalysts. The results indicated that there was almost no methane production in the comparison experiments.

3. Results and Discussions

3.1. Phase Structure, Morphology, and Optical Absorption of Pt-Loaded TiO_2 Nanosheet Porous Film. The phase structure of the titania films was analyzed by the XRD technique. As shown in Figure 1(a), the TiO_2 film belongs to the typical anatase phase. In our previous work, we knew that TAN precursor belonged to the orthorhombic system [19]. This indicated that the orthorhombic TAN has been transformed to anatase TiO_2 completely after being calcined at 400°C for 4 h. There still existed some characteristic peaks of metallic Ti at 40.2° , 63.1° , and 70.7° , indicating that only the surface of the Ti foil reacted with NaOH, and the interior still remained as Ti metal. When Pt nanoparticles were loaded on the surface of TiO_2 nanosheet porous films, the anatase phase did not change. And no apparent Pt diffraction signals appeared; this may be due to the ultrafine dispersion of Pt nanoparticles on TiO_2 nanosheet porous films and its low loading amount. However, the EDS results verified that Pt nanoparticles were successfully modified on the TiO_2 nanosheet porous films (as shown in Figure 1(b)); the mole ratio of Pt to TiO_2 was estimated to be ca. 0.14%.

Figure 2 shows the surface morphology of the Pt-loaded TiO_2 nanosheet porous films. As can be seen from Figure 2(a), anatase TiO_2 film consisted of many thin nanosheets, and the surface of the film looks like porous structure. Figure 2(b) showed that some Pt nanoparticles were successfully deposited on the surface of TiO_2 nanosheet porous film and were homogeneous both in size and in shape. To further observe the morphology of TiO_2 film, some powders were peeled off from the substrate, and their TEM images are shown in Figures 2(c) and 2(d); we can clearly see that Pt nanoparticles are very uniform, and their particle sizes are only 3–4 nm. On one hand, the porous nanosheet structure of this kind of TiO_2 film occupied larger BET surface area than the common TiO_2 film obtained by the sol-gel method, so it can increase the adsorption amount of the reactive species and then accelerate the photocatalytic reaction rate. On the other hand, more irradiated light can be utilized for the porous TiO_2 film because of the multiple scattering and reflection of the incident light in the channels of the porous film [17, 20, 21], so the utilization efficiency

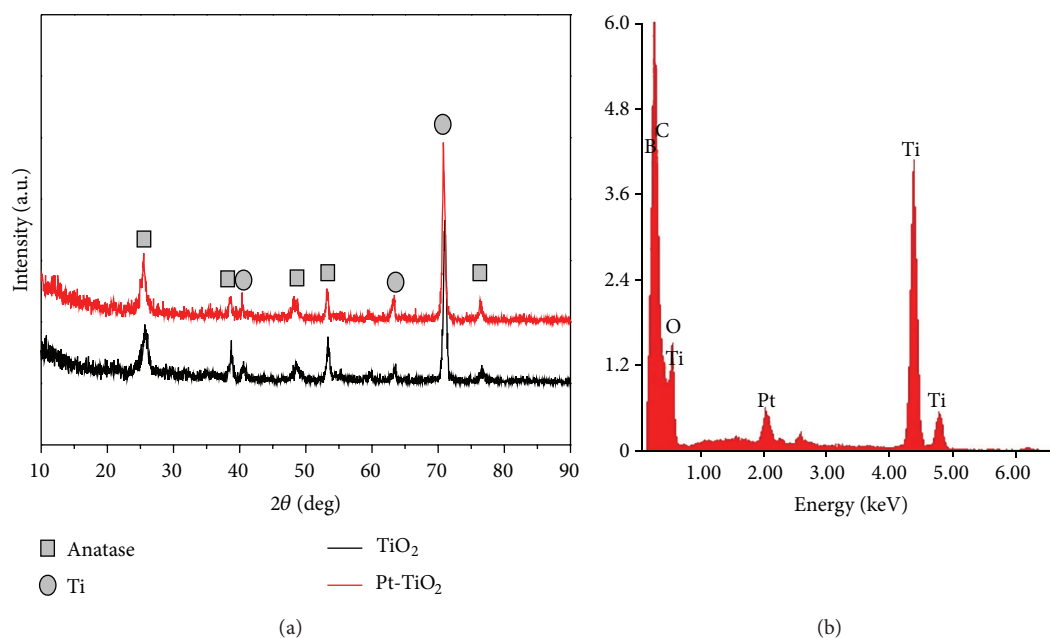


FIGURE 1: XRD patterns of TiO_2 and Pt- TiO_2 nanosheet films.

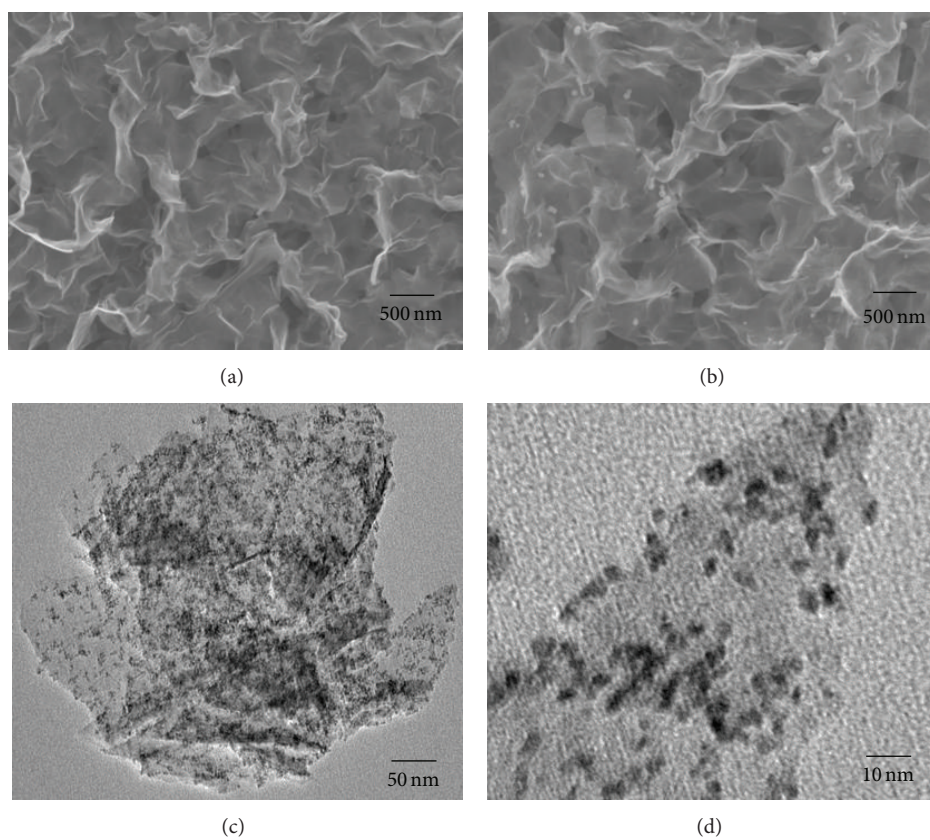


FIGURE 2: SEM images of TiO_2 and Pt- TiO_2 nanosheet films.

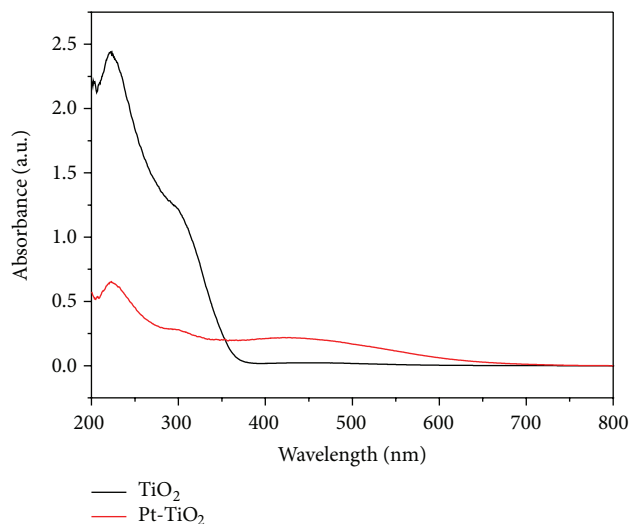


FIGURE 3: UV-vis DRS spectra of TiO_2 and Pt- TiO_2 nanosheet films.

of the incident light was increased and thereby did favor for improving the photocatalytic activity.

The optical absorption of the nanosheet porous films was shown in Figure 3. The absorption band edge of TiO_2 porous film was 380 nm. In our previous work [13, 22], we found that the onset absorption of the titanate acid was about 350–360 nm. So from the change of the absorption band, we can conclude that the titanate acid had transformed to anatase TiO_2 successfully by the calcination of 400°C. While Pt nanoparticles were loaded on the surface of the TiO_2 porous film, a broad peak at around 350–550 nm was observed, which should be due to the plasma resonance absorption of the Pt nanoparticles [23]. Moreover, the absorbance intensity of the film in the UV light region reduced, which should be because the loaded Pt nanoparticles shield some absorption of TiO_2 nanosheets.

3.2. Photoreduction of CO_2 on Pt-Loaded TiO_2 Nanosheet Porous Film. The photoreduction of CO_2 to methane was tested as a probe reaction to evaluate the photocatalytic activity of the catalyst films. As shown in Figure 4(a), the production rate of CH_4 on Pt-loaded TiO_2 nanosheet porous film reached 20.51 ppm/h·cm². To confirm the photocatalytic reduction process of CO_2 to CH_4 , the related reference experiments were carried out. When the system was kept in dark, there was no CH_4 produced, indicating that the photoexcited process of Pt-loaded TiO_2 was essential in the photoreduction of CO_2 . When the experiment was carried out in the absence of H_2O , almost no CH_4 was detected. That implying that water is also one of the key roles for CO_2 photoreduction. When a blank Ti foil with the same area of Pt-loaded TiO_2 film was put into the system, the production rate of CH_4 was only 1.01 ppm/h·cm². This slow production rate of CH_4 should be due to the thin oxide layer on Ti foil surface.

In addition, some comparative experiments about Pt-loaded TiO_2 , TiO_2 porous film, and ordinary R- TiO_2 obtained by the sol-gel method proceeded. As can be seen, under the same experiment conditions, the production rate of CH_4 on Pt-loaded TiO_2 , TiO_2 , and R- TiO_2 was 20.51, 3.71, and 1.45 ppm/h·cm², respectively. Obviously, the photocatalytic activity of the Pt- TiO_2 nanosheet porous film was much higher than that of TiO_2 and R- TiO_2 film; the possible reasons were listed as follows. Firstly, it is commonly known that Pt could promote the interparticle charge migration and facilitate the photogenerated electrons transfer from conduction band of the TiO_2 to Pt particles, so as to provide adequate electrons for the reduction of carbon dioxide to methane [24]. The charge carrier separation ability of Pt nanoparticles was verified by the transient photocurrent-time curve. As shown in Figure 4(b), the photocurrent density of TiO_2 and Pt- TiO_2 nanosheet film was 0.006 and 0.017 mA·cm⁻², respectively. The photocurrent density of Pt- TiO_2 was apparently larger than that of TiO_2 , indicating that its separation efficiency of the photogenerated charge carriers was higher. Secondly, the large BET surface area and strong adsorption ability of the TiO_2 nanosheet porous structure can provide more adsorption sites for CO_2 molecules, so the localized concentration of CO_2 on the surface of TiO_2 porous film would be higher, which would accelerate the photoreduction reaction of CO_2 to methane. Thirdly, the porous and incompact structure of the TiO_2 nanosheet porous film would facilitate the use of more irradiated light, because more light can be scattered and reflected in the channels and pores of TiO_2 film [25].

3.3. Proposal of the Photoreduction Mechanism of CO_2 to Methane on Pt-Loaded TiO_2 Nanosheet Porous Film. The photoreduction mechanism of CO_2 to methane on Pt-loaded TiO_2 nanosheet porous film was proposed in Figure 5. Most researchers agree that this process is based on proton-assisted multielectron transfer instead of single electron transfer, as the electrochemical potential of -2.14 V versus SCE for a single electron process is highly unfavorable [26]. When Pt-loaded TiO_2 nanosheet porous film was illuminated by UV light, photon-generated electrons (e^-) and holes (h^+) are created on the surface of the TiO_2 nanosheets. The excited holes reacted with adsorbed water molecules on the catalyst surface to produce hydroxyl radicals ($\cdot\text{OH}$) and hydrogen ions (H^+) and further oxidized by $\cdot\text{OH}$ radicals to produce O_2 and H^+ [27]. And H^+ would interact with the excited electrons to form $\cdot\text{H}$ radicals. At the same time, the photo-generated electrons on the conduction band of TiO_2 can be easily trapped by Pt nanoparticles because of the lower Fermi energy level of the noble metal [28], and then they would transfer rapidly to the absorbed CO_2 for photoreduction reaction. CO_2 molecules would interact with the excited electrons to form to $\cdot\text{CO}_2^-$ radicals, and then reacted with $\cdot\text{H}$ on the catalyst surface to produce CH_4 [1, 28, 29]. It is known that the formation of CH_4 requires eight electrons, and the enriched electron density on Pt nanoparticles would favor the formation of CH_4 , which is thermodynamically

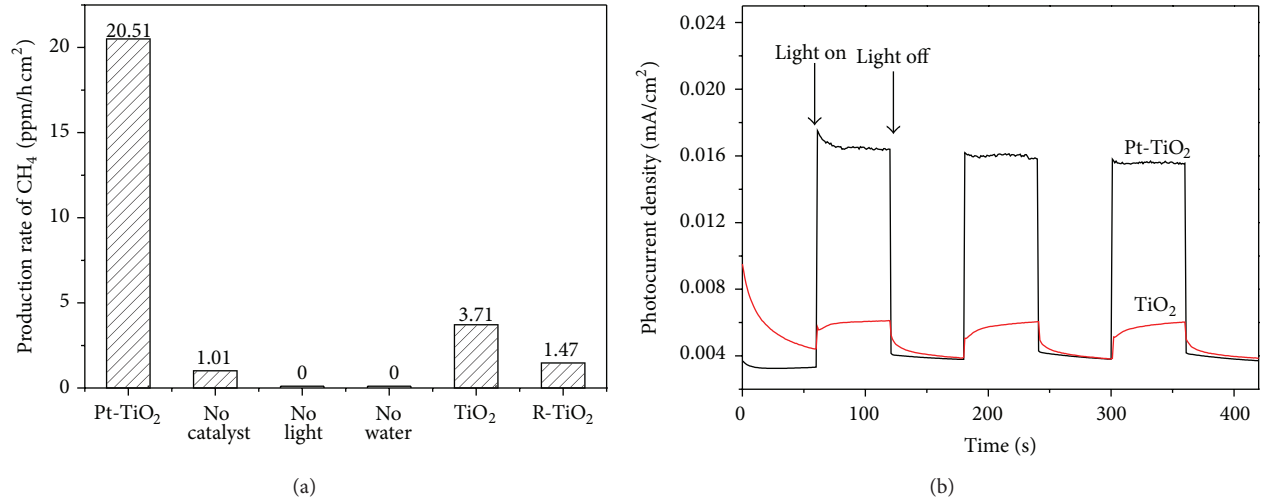


FIGURE 4: Evolution yield of CH_4 and photocurrent-time curve of TiO_2 and Pt- TiO_2 network film under UV irradiation in same conditions.

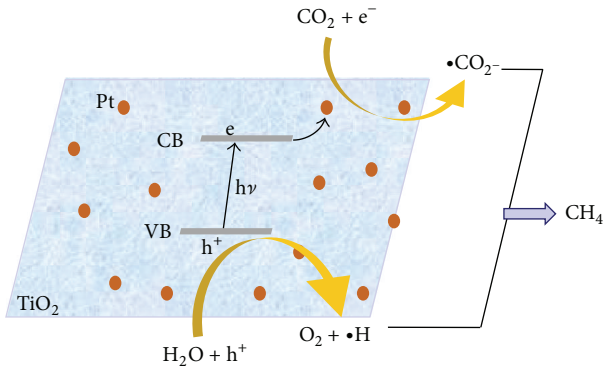
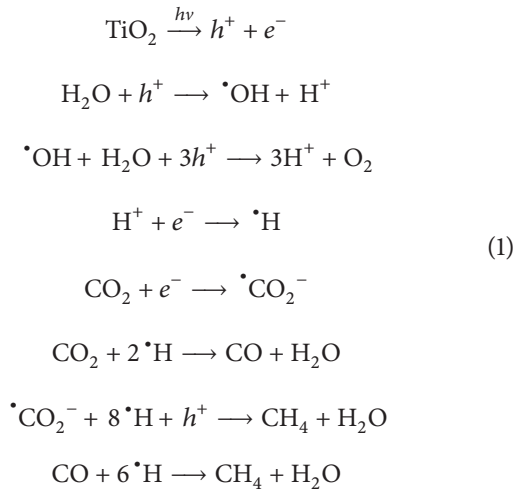


FIGURE 5: Photoreduction mechanism of CO_2 to methane on Pt-loaded TiO_2 nanosheet porous film.

more feasible. The possible process would have undergone the following pathway:



4. Conclusions

Anatase TiO_2 nanosheet porous films obtained by calcination of the orthorhombic titanic acid films exhibited better performance for the photoreduction of CO_2 to methane. In order to further improve the photoactivity, Pt nanoparticles with the particle size of 3-4 nm were loaded on the TiO_2 porous films uniformly. The EDS results confirmed the mole ratio of Pt to TiO_2 was ca. 0.14%. The conversion yield of CO_2 to methane on Pt/ TiO_2 film reached 20.51 ppm/h- cm^2 . The transient photocurrent-time curves showed that the Pt/ TiO_2 nanosheet porous film exhibited higher photocurrent, so the higher separation efficiency of the photogenerated charge carriers should be the main reason for the high photoreduction activity of CO_2 .

Conflict of Interests

The authors declare that there is no conflict of interests regarding the publication of this paper.

Authors' Contribution

Li Qiu-ye and Zong Lan-lan contributed equally to this work.

Acknowledgments

The authors gratefully acknowledge the support of the National Natural Science Foundation of China (no. 21103042), the Specialized Research Fund for the Doctoral Program of Higher Education (no. 20114103120001), and the Scientific Research Foundation of Henan University (no. 2010YBZR013).

References

- [1] K. Kočí, L. Obalová, and Z. Lacný, "Photocatalytic reduction of CO₂ over TiO₂ based catalysts," *Chemical Papers*, vol. 62, pp. 1–9, 2008.
- [2] H. Yamashita, Y. Fujii, Y. Ichihashi et al., "Selective formation of CH₃OH in the photocatalytic reduction of CO₂ with H₂O on titanium oxides highly dispersed within zeolites and mesoporous molecular sieves," *Catalysis Today*, vol. 45, no. 1–4, pp. 221–227, 1998.
- [3] S. G. Zhang, Y. Fujii, H. Yamashita, K. Koyano, T. Tatsumi, and M. Anpo, "Photocatalytic reduction of CO₂ with H₂O on Ti-MCM-41 and Ti-MCM-48 mesoporous zeolites at 328 K," *Chemistry Letters*, no. 7, pp. 659–660, 1997.
- [4] J. Rasko and F. Solymosi, "Infrared spectroscopic study of the photoinduced activation of CO₂ on TiO₂ and Rh/TiO₂ catalysts," *The Journal of Physical Chemistry*, vol. 98, pp. 7147–7152, 1994.
- [5] W. Lin, H. Han, and H. Frei, "CO₂ splitting by H₂O to CO and O₂ under UV light in TiMCM-41 silicate sieve," *Journal of Physical Chemistry B*, vol. 108, no. 47, pp. 18269–18273, 2004.
- [6] M. Anpo, H. Yamashita, K. Ikeue et al., "Photocatalytic reduction of CO₂ with H₂O on Ti-MCM-41 and Ti-MCM-48 mesoporous zeolite catalysts," *Catalysis Today*, vol. 44, no. 1–4, pp. 327–332, 1998.
- [7] M. Anpo, H. Yamashita, Y. Ichihashi, Y. Fujii, and M. Honda, "Photocatalytic reduction of CO₂ with H₂O on titanium oxides anchored within micropores of zeolites: effects of the structure of the active sites and the addition of Pt," *Journal of Physical Chemistry B*, vol. 101, no. 14, pp. 2632–2636, 1997.
- [8] M. Anpo, H. Yamashita, Y. Ichihashi, and S. Ehara, "Photocatalytic reduction of CO₂ with H₂O on various titanium oxide catalysts," *Journal of Electroanalytical Chemistry*, vol. 396, no. 1–2, pp. 21–26, 1995.
- [9] Y. J. Xu, F. M. Chen, L. Jiang, and L. D. Zhou, "Photoreduction of CO₂ in the suspension system of semiconductor catalyst TiO₂ modified by palladium," *Photochemical & Photobiological Sciences*, vol. 17, p. 61, 1999.
- [10] A. Kudo and Y. Miseki, "Heterogeneous photocatalyst materials for water splitting," *Chemical Society Reviews*, vol. 38, no. 1, pp. 253–278, 2009.
- [11] H. J. Yun, H. Lee, J. B. Joo, N. D. Kim, M. Y. Kang, and J. Yi, "Facile preparation of high performance visible light sensitive photo-catalysts," *Applied Catalysis B: Environmental*, vol. 94, pp. 241–247, 2010.
- [12] Q. Zhang, J.-B. Joo, Z. Lu et al., "Self-assembly and photocatalysis of mesoporous TiO₂ nanocrystal clusters," *Nano Research*, vol. 4, no. 1, pp. 103–114, 2011.
- [13] Q. Y. Li, T. Kako, and J. H. Ye, "Strong adsorption and effective photocatalytic activities of one-dimensional nano-structured silver titanates," *Applied Catalysis A: General*, vol. 375, pp. 85–91, 2010.
- [14] Q. Y. Li, T. Kako, and J. H. Ye, "PbS/CdS nanocrystal-sensitized titanate network films: enhanced photocatalytic activities and super-amphiphilicity," *Journal of Materials Chemistry*, vol. 20, pp. 10187–10192, 2010.
- [15] S. Berger, H. Tsuchiya, A. Ghicov, and P. Schmuki, "High photocurrent conversion efficiency in self-organized porous WO₃," *Applied Physics Letters*, vol. 88, no. 20, Article ID 203119, 2006.
- [16] T. Kimura, N. Miyamoto, X. Meng, T. Ohji, and K. Kato, "Rapid fabrication of mesoporous titania films with controlled macroporosity to improve photocatalytic property," *Chemistry*, vol. 4, no. 9, pp. 1486–1493, 2009.
- [17] Q. Y. Li, T. Kako, and J. H. Ye, "WO₃ modified titanate network film: highly efficient photo-mineralization of 2-propanol under visible light irradiation," *Chemical Communications*, vol. 46, pp. 5352–5354, 2010.
- [18] X. D. Wang, X. Xue, Q. Y. Li, M. Zhang, and J. J. Yang, "Twice heat-treating to synthesize TiO₂/carbon composites with visible-light photocatalytic activity," *Materials Letters*, vol. 88, pp. 79–81, 2012.
- [19] J. Yang, Z. Jin, X. Wang et al., "Study on composition, structure and formation process of nanotube Na₂Ti₂O₄(OH)₂," *Journal of the Chemical Society. Dalton Transactions*, no. 20, pp. 3898–3901, 2003.
- [20] X. Chen, J. Ye, S. Ouyang, T. Kako, Z. Li, and Z. Zou, "Enhanced incident photon-to-electron conversion efficiency of tungsten trioxide photoanodes based on 3d-photon crystal design," *ACS Nano*, vol. 5, no. 6, pp. 4310–4318, 2011.
- [21] H. Xu, X. Q. Chen, S. X. Ouyang, T. Kako, and J. H. Ye, "Size-dependent Mie's scattering effect on TiO₂ spheres for the superior photoactivity of H₂ evolution," *Journal of Physical Chemistry C*, vol. 116, pp. 3833–3839, 2012.
- [22] Q. Y. Li, X. D. Wang, Z. S. Jin et al., "n/p-Type changeable semiconductor TiO₂ prepared from NTA," *Journal of Nanoparticle Research*, vol. 9, pp. 951–957, 2007.
- [23] A. Gallo, M. Marelli, R. Psaro et al., "Bimetallic Au-Pt/TiO₂ photocatalysts active under UV-A and simulated sunlight for H₂ production from ethanol," *Green Chemistry*, vol. 14, no. 2, pp. 330–333, 2012.
- [24] S. J. Xie, Y. Wang, Q. H. Zhang, W. Q. Fan, W. P. Deng, and Y. Wang, "Photocatalytic reduction of CO₂ with H₂O: significant enhancement of the activity of Pt-TiO₂ in CH₄ formation by addition of MgO," *Chemical Communications*, vol. 49, pp. 2451–2453, 2013.
- [25] Q. Y. Li, Y. Y. Xing, R. Li, L. L. Zong, X. D. Wang, and J. J. Yang, "AgBr modified TiO₂ nanotube films: highly efficient photodegradation of methyl orange under visible light irradiation," *RSC Advances*, vol. 2, pp. 9781–9785, 2012.
- [26] A. J. Morris, G. J. Meyer, and E. Fujita, "Development of molecular electrocatalysts for CO₂ reduction and H₂ production/oxidation," *Accounts of Chemical Research*, vol. 42, pp. 1983–1982, 2009.
- [27] S. S. Tan, L. Zou, and E. Hu, "Photocatalytic reduction of carbon dioxide into gaseous hydrocarbon using TiO₂ pellets," *Catalysis Today*, vol. 115, pp. 269–273, 2006.
- [28] W. N. Wang, W. J. An, B. Ramalingam et al., "Size and structure matter: enhanced CO₂ photoreduction efficiency by size-resolved ultrafine Pt nanoparticles on TiO₂ single crystals," *Journal of the American Chemical Society*, vol. 134, pp. 11276–11281, 2012.
- [29] Q. H. Zhang, W. D. Han, Y. J. Hong, and J. G. Yu, "Photocatalytic reduction of CO₂ with H₂O on Pt-loaded TiO₂ catalyst," *Catalysis Today*, vol. 148, pp. 335–340, 2009.

Research Article

Preparation and Photocatalytic Activity of Ag Modified Ti-Doped-Bi₂O₃ Photocatalyst

Lilan Zhang, Junfeng Niu, Duo Li, Ding Gao, and Jianghong Shi

State Key Laboratory of Water Environment Simulation, School of Environment, Beijing Normal University, Beijing 100875, China

Correspondence should be addressed to Junfeng Niu; junfengn@bnu.edu.cn and Jianghong Shi; shijianghong@bnu.edu.cn

Received 15 December 2013; Accepted 8 January 2014; Published 17 February 2014

Academic Editor: Shaohua Shen

Copyright © 2014 Lilan Zhang et al. This is an open access article distributed under the Creative Commons Attribution License, which permits unrestricted use, distribution, and reproduction in any medium, provided the original work is properly cited.

Ti doped Bi₂O₃ (TDB) and Ag ion modified Ti doped Bi₂O₃ (Ag@TDB) photocatalysts were prepared by framework replacement synthesis method with different Ag loadings (0.05, 0.3, 0.75, and 1.0 mol/L AgNO₃). The structural properties of the prepared catalysts were studied by scanning electron microscope (SEM), X-ray diffraction (XRD), BET surface area, and UV/Vis diffuse reflectance (DRS). The XRD spectra of the Ti doped Bi₂O₃ calcined at 650°C showed the diffraction peaks of a mixture of Bi₁₂TiO₂₀ and Bi₄Ti₃O₁₂, with bits of mixed crystallite consisting of TiO₂ and Bi₂O₃. A high blue shift in the range 650–550 nm was detected in the DRS band. This blue shift increased with the decreasing Ag content. The photocatalytic activities of the catalysts were evaluated for the degradation of crystal violet (CV) under UV light irradiation. The results indicated that the degradation rate of CV by using 1.0 mol/L AgNO₃ doped bismuth titanate composite photocatalyst (1.0 Ag@TDB) was 1.9 times higher than that by using the bare Ti doped Bi₂O₃ photocatalyst. The higher activity of Ag@TDB is due to the enhancement of electron-hole pair separation by the electron trapping of silver particles.

1. Introduction

Photocatalytic degradation of organic pollutants is an alternative and harmless technology for the removal of organic impurities [1]. The crucial step for its application is to develop new, efficient, and clean catalysts. Recently, bismuth-based oxides photocatalysts such as Bi₂O₃, BiVO₄, and Bi₂WO₆ have attracted much attention due to their attractive photocatalytic properties under visible light irradiation [2–4]. Bi₂O₃ has been widely used in gas sensors, solid oxide fuel cells, optical coatings, and ceramic glass manufacturing due to its high refractive index, dielectric permittivity, marked photoluminescence properties, and thermal stability [5]. Furthermore, Bi₂O₃ has also shown higher photocatalytic activities in splitting water and decomposing pollutant. Despite the positive attributes of Bi₂O₃, low quantum yields hinder its practical application.

To improve the photocatalytic properties of catalysts, transition-metal ions with 3D electron structure, such as Fe(III), Sm(III), and Zn(II), have been widely used to modify the photocatalysts because they can act as shallow

charge traps [6–9]. In our previous research, transition-metal ion Ti(IV) doped bismuth-based oxides photocatalysts have been confirmed to show higher photocatalytic activity. The decolorization rates of crystal violet (CV) in aqueous solution with Ti(IV) doped Bi₂O₃ (TDB) have been proved to be double compared with that with bare Bi₂O₃ [10]. Pentachlorophenol could be also removed efficiently by using TDB, and its reductive dechlorination route under visible light irradiation was firstly revealed [11]. The removal ratios of pentachlorophenol and 2,4-dichlorophenol were 99.7% and 99.2%, respectively, by using TDB photocatalysis combined with laccase catalysis [12]. The results showed that Ti (IV)-doping improved the light absorption capacity and enhanced the photogenerated electron yield of Bi₂O₃, which was mainly attributed to the narrowed band gap (E_g) and red shift of light absorption edge [10].

The photocatalytic efficiency of catalysts is closely related to the rates of recombination of photoexcited electrons and holes [13]. Insertion of noble metal (e.g., Pt, Au, and Ag) could reduce the rate of charge carrier recombination and then improve the photocatalytic activity of catalysts. For example,

Sobana et al. [14] reported that the photocatalytic activity of silver doped TiO_2 was far much higher than that of the bare TiO_2 for the degradation of azo dyes. Additionally, the photonic efficiency of all metal-doped TiO_2 (i.e., Pt, Au, and Pd) was found to be higher than bare TiO_2 due to the acceleration of hydroxyl radical formation and decreasing recombination [15]. Rayalu et al. [16] used Au/TiO_2 as a catalyst in hydrogen generation under visible light illumination for their high photocatalytic activity. Evidence indicated that the photocatalytic activity could be enhanced by the impregnation of the semiconductor surfaces with optimal loading.

The aim of this study was to assess the photocatalytic activity of TDB by additional doping with Ag ion. A series of Ag ion modified Ti doped Bi_2O_3 (Ag@TDB) photocatalysts were prepared by the framework replacement synthesis method. The influences of the Ag ion contents on the surficial properties, optical absorption, and crystal shape of the photocatalysts were studied. The photocatalytic degradation of CV was explored by using Ag@TDB , and the optimal Ag ion loading content was obtained. Finally, the promotion mechanisms of Ag@TDB were proposed.

2. Materials and Methods

2.1. Catalyst Preparation. The bare TDB was prepared by a hydrothermal synthesis technique as described in detail elsewhere [11]. The TDB photocatalysts were then dipped in an aqueous solution of silver nitrate (AgNO_3) with proper concentration after 2 h of illumination under UV light (at 254 nm) from a G15W/T8 Sylvania tube lamp (in the presence of atmospheric oxygen). After dipping, the catalysts were thoroughly washed with ultrapure water and dried at 150°C for 24 h. The concentrations of AgNO_3 were 0.05, 0.3, 0.75, and 1.0 mol/L. The prepared photocatalysts were labeled as 0.05 Ag@TDB , 0.3 Ag@TDB , 0.75 Ag@TDB , and 1.0 Ag@TDB , respectively.

2.2. Catalyst Characterization. Detailed surface images of the photocatalysts were obtained by means of a scanning electron microscope (SEM, JSM-6360LV, Hitachi). The structures of the photocatalysts were characterized by X-ray diffraction (XRD, D/MAX-rb, Rigaku). UV-visible absorbance spectrophotometry (DRS, Varian-CARY 1E UV-visible spectrophotometer, Varian) was used to measure the absorption spectrometry. The surface area and pore sizes were measured using a gas sorption analyzer (ASAP-2010 M, Micromeritics).

2.3. Photocatalytic Degradation of Crystal Violet. The photocatalytic efficiencies of catalysts were evaluated by the degradation of CV in aqueous solution. In all cases, a volume of 100 mL CV solution was used to conduct the photocatalytic experiments with regard to the effects of catalyst dosages (0.2 g/L, 1.0 g/L, 1.6 g/L, and 2.0 g/L), catalyst types (TDB, 0.05 Ag@TDB , 0.3 Ag@TDB , 0.75 Ag@TDB , and 1.0 Ag@TD), and initial CV concentrations (5, 10, 20 mg/L). The dye solution containing the appropriate quantity of the photocatalyst powder was magnetically stirred before and during

illumination. Prior to irradiation, the suspension solution was firstly ultrasonicated for 15 min and then transferred to the photocatalytic reactor. The reactor was covered by aluminium foil to prevent UV light leakage. The suspension was irradiated under an 8 W UV lamp (UV354L, 354 nm, Beony S.T.). A suspension solution of 5 mL was withdrawn after periodic interval of irradiation and analyzed after filtration. The photocatalytic degradation ratio of CV was monitored by measuring the absorbance in a UV-Vis spectrophotometer.

3. Results and Discussion

3.1. Characterization. The phase and composition of TDB photocatalysts were characterized by XRD. Figure 1(a) shows the XRD pattern of the bare TDB photocatalyst. The diffraction peaks can be indexed to a mixture of $\text{Bi}_{12}\text{TiO}_{20}$ and $\text{Bi}_4\text{Ti}_3\text{O}_{12}$, with bits of mixed crystallite consisting of TiO_2 and B_2O_3 . The monoclinic phase was mixed with three-phase (α , β , γ). Bismuth-based oxides exist in four stable crystalline phases under atmospheric pressure: α , β , γ , and δ [17]. The crystalline phase significantly affects the structural, textural, and catalytic properties of photocatalyst [10].

The prepared TDB catalysts show light yellow colors. Dipping the TDB catalysts in AgNO_3 aqueous could darken the particles, revealing the presence of silver compounds [18, 19]. In order to explore the influence of Ag ion doping on the optic absorption of photocatalysts, a UV-Vis spectrophotometer was used to measure their absorption spectra with the wavelength from 240 to 800 nm. As shown in Figure 1(b), all the catalysts have good properties of visible light absorption. The absorption peak of TDB even extends to >500 nm. Comparably, the absorption peaks of all the Ag@TDB catalysts have blue shift phenomenon. In particular, the photocatalyst 1.0 Ag@TDB exhibits an absorption peak at 450 nm. The degree of blue shifting of catalysts decreased with the increase of the Ag ion content in the catalysts. The blue shift in the UV absorption spectra has been also reported in ceria-containing nanomaterials in recent years, and the quantum size effect has been proposed to explain this phenomenon for the pure ceria nanocrystals [20, 21]. Considering the blue shift in the UV spectra for the Ag@TDB system, the energy level lied beneath the valence band formed by the hybrid track of Bi 6s and O 2p for the bare TDB. The impurity levels of Ag@TDB were located between valence band and conduction band of TDB due to Ag ion doping, which potentially led to the blue shift. This phenomenon was not convenient for visible light absorption but for photocatalytic reactions under UV light illumination.

The morphology of the photocatalysts was characterized by SEM. Figure 2 reveals that particle diameters ranging from 80 to 200 nm varied in size and shape. These particles were easy to cluster into aggregates ranging from 5 to 200 μm , and their shapes were mostly spherical and ellipsoidal in the low-resolution image. Compared with the TDB, the shape of the Ag@TDB changed from duct-like to scale-like and then into slice with the increasing Ag ion content from 0.05 to 1.0 mol/L. The morphology of the photocatalyst is closely related to their activities [2]. The Brunauer Emmett Teller

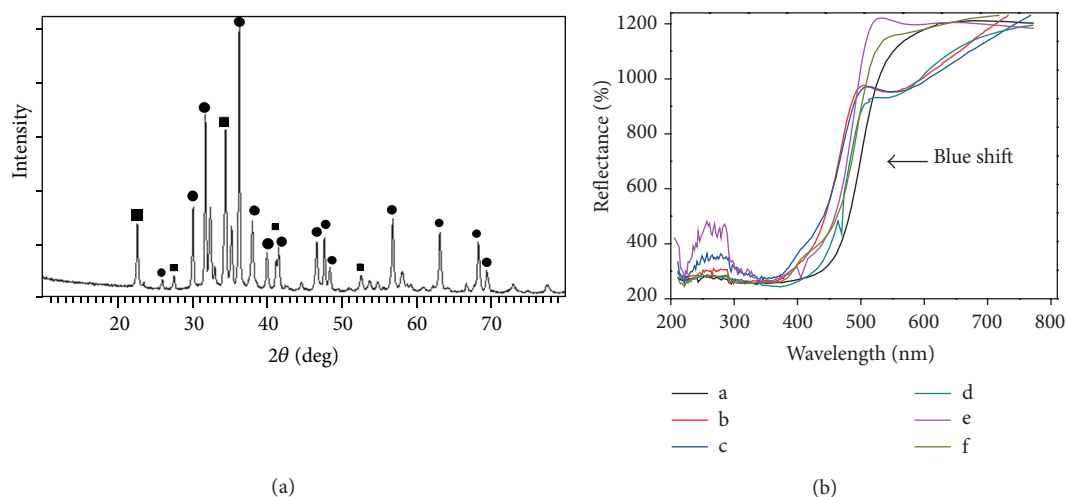


FIGURE 1: (a) Powder X-ray diffraction (XRD) patterns of bismuth titanate composite; ● represents the XRD peak of $\text{Bi}_{12}\text{Ti}_{20}$; ■ represents the XRD peak of $\text{Bi}_4\text{Ti}_3\text{O}_{12}$. (b) UV-Vis diffuse reflectance spectra of TDB—a; 0.05 Ag@TDB—b; 0.1 Ag@TDB—c; 0.3 Ag@TDB—d; 0.75 Ag@TDB—e; and 1.0 Ag@TDB—f.

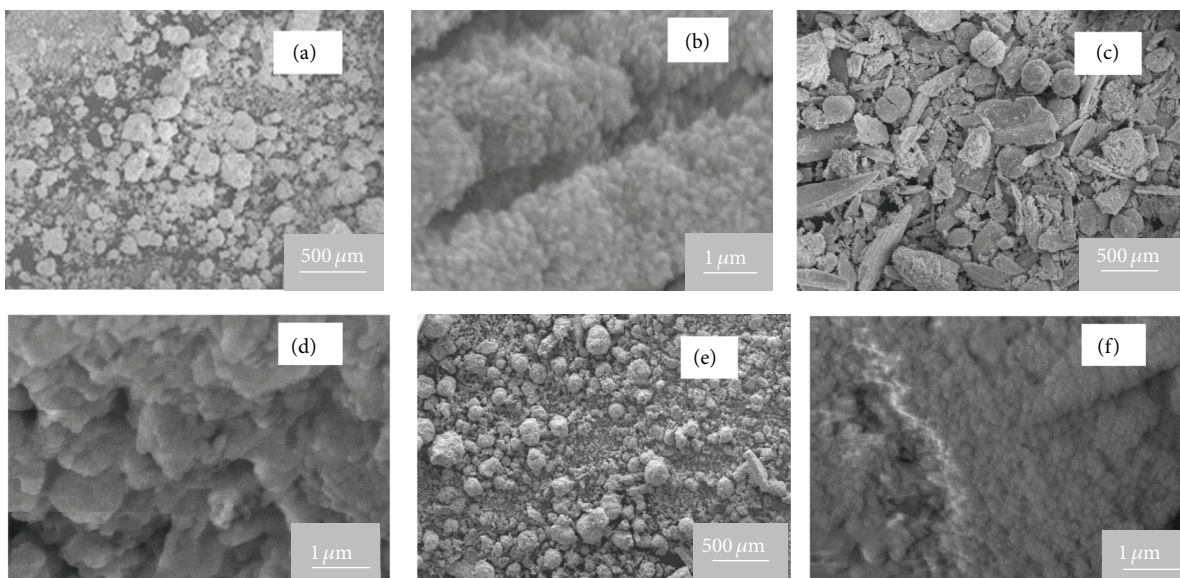


FIGURE 2: Scanning electron microscopy images of photocatalyst with bismuth titanate composite (TDB) without Ag-dope (a), (b); 0.05 Ag@TDB (c), (d); and 1.0 Ag@TDB (e), (f) with image resolution at 500 μm and 1 μm .

(BET) surface areas of the photocatalysts were 20~60 m^2/g . There was no significant change in the surface area after metallisation of TDB particles. The average pore size estimated by the Barrett Joyner Halenda (BJH) method was 1.7 nm, indicating that these catalysts have mesoporous structure and good photocatalytic performances.

3.2. Evaluation of the Photocatalytic Activity

3.2.1. Effect of Catalyst Concentration. To remove pollutants economically and efficiently, it is important to find the optimal amount of catalyst. The effect of photocatalyst TDB concentration from 0.2 to 2.0 g/L on the photodegradation of

CV solution of 5 mg/L was explored under UV irradiation under room temperature. As shown in Figure 3, the degradation rates increased from 0.335 to 0.47 with the increase of the catalyst dosage from 0.2 to 1.0 g/L. The degradation rate was almost constant when the dosage of the catalyst was beyond 1.0 g/L. At the low catalyst concentration, the increase of TDB particle concentrations led to the increase of the number of absorbed photons and the number of the adsorbed dye molecules, enhancing the photocatalytic efficiency. As the concentration of catalyst was higher than the optimal value, the degradation rates decreased due to the increasing turbidity of the suspension and light scattering. Hence, 1.0 g/L was used as the catalyst dosage for the following photocatalytic reactions.

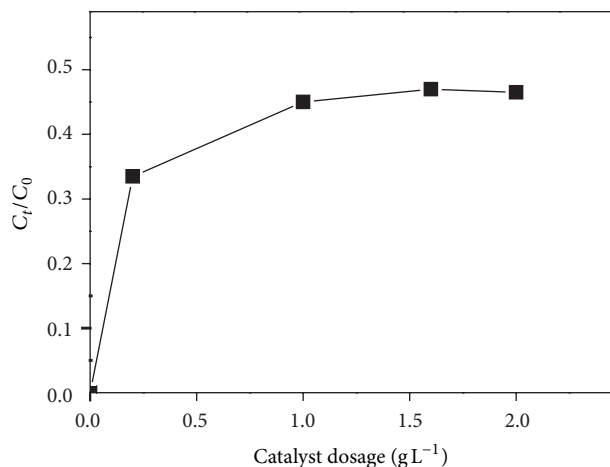


FIGURE 3: Effect of the TDB catalyst amount on degradation rate of crystal violet.

3.2.2. Effect of Initial Crystal Violet Concentration. The effect of initial CV concentration on the degradation efficiency was investigated by changing the initial concentration from 5.0 to 20.0 mg/L at constant catalyst loading (1.0 Ag@TDB, 1.0 g/L). The results are shown in Figure 4. The degradation rate of CV at low concentration was high. The degradation ratio decreased from 92.1% to 45.0% with the increase of initial CV concentration from 5 mg/L to 20 mg/L, suggesting that the increase of the dye concentration decreased the removal ratio. Similar results have been reported for the photocatalytic degradation of other dyes in aqueous solution (e.g., quinolone yellow, acid red, and reactive dyes 4) [22–24]. An explanation to this phenomenon was that the increase of dye concentration led to the increase of the amount of dye adsorbed on the catalyst surface, reducing the active sites for adsorption of hydroxyl ions and the generation of hydroxyl radicals. The increase of dye concentration could also intercept the path of photons reaching the catalyst surface and decrease the adsorption of photons on catalyst particles. Additionally, at high concentration, the dye molecules would compete for UV light absorption with the catalyst, which may also reduce the degradation efficiency [25].

3.2.3. Effect of Catalysts Type. The photocatalytic activities of TDB and Ag@TDB were evaluated and compared by degradation of CV at 5 mg/L in aqueous solution under UV light irradiation. As shown in Figure 5, the removal rate of CV is below 5% in the dark, indicating that the adsorption of catalysts could be negligible. The removal ratio of CV was 33.5% by using TDB photocatalyst in 80 min. Under the same reaction conditions, the removal ratios of CV were 36.1%, 62.5%, 86.64%, and 91.5% by using 0.05 Ag@TDB, 0.3 Ag@TDB, 0.75 Ag@TDB, and 1.0 Ag@TDB photocatalysts, respectively. The results indicated that all the Ag modified particles exhibited higher activities than the bare TDB particles. The degradation rate of CV increased with the increase of the Ag ion doping content. The main reason might be that Ag ions on Ag@TDB surface acted as sites where electrons

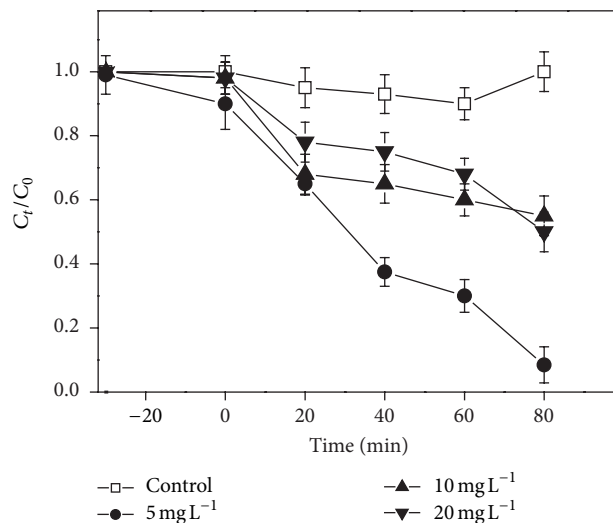


FIGURE 4: Crystal violet concentration change as a function of photocatalysis time at initial concentration of 5, 10, and 20 mg/L with 1.0 g/L 1.0 Ag@TDB catalyst.

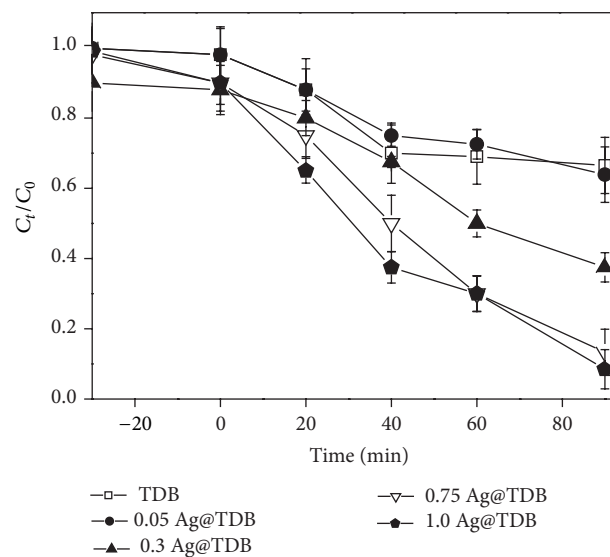


FIGURE 5: Degradation of crystal violet at 5.0 mg L⁻¹ with different Ag ion doping TDB under UV light irradiation.

accumulated. Better separation of electrons and holes on Ag@TDB catalyst surface allowed more efficient channeling of the charge carriers into useful reduction and oxidation reactions rather than recombination reactions [26, 27]. The degradation rate with 0.75 Ag@TDB was 1.4 times that with 0.05 Ag@TDB. The degradation rate with 1.0 Ag@TDB was only 0.05 times that with 0.75 Ag@TDB. This change can be due to the fact that Ag particles can act as recombination centers as the Ag content is beyond its optimal value [27, 28]. Furthermore, the active sites of catalyst were fully occupied by Ag ions. The rest of Ag ions played slight role on CV degradation, leading to slight rise of CV degradation rate with higher Ag ion doping. Additionally, it was observed that

the color of catalyst became darker during the irradiation. The main reason was that the reduction potential of silver ion is prone to photocatalytic reduction $\text{Ag}^+ + \text{e}^- \rightarrow \text{Ag}^0$, producing metallic silver on catalyst surface.

4. Conclusions

The doping of silver alters the structure of TDB catalyst and leads to the blue shift. The degradation ratios of CV were obtained by using TDB and Ag@TDB photocatalysts in aqueous solution under UV light irradiation. The results indicated that the degradation efficiency of CV was significantly impacted by its initial concentrations, photocatalyst amounts, and photocatalyst types. The optimal amount of photocatalyst was 1.0 g/L at the CV concentration of 5 mg/L. For photocatalyst type, the photocatalytic activities of Ag@TDB were significantly higher those that of bare TDB. There are two main reasons: (1) Ag ion doped improved the photocatalyst activities due to trapping photoelectrons of Ag ion and (2) the photocatalyst has mesoporous structure. CV could be effectively degraded by Ag@TDB under UV light irradiation, indicating that Ag@TDB is expected to exhibit high practicability and good performance for the degradation of dyes.

Conflict of Interests

The authors declare that there is no conflict of interests regarding the publication of this paper.

Acknowledgments

This study was financially supported by the National Natural Science Foundation of China (no. 21077010), the Fok Ying-Tong Education Foundation of China (Grant no. 121077), and the Specialized Research Fund for the Doctoral Program of Higher Education of China (no. 20110003110023).

References

- [1] D. S. Bhatkhande, V. G. Pangarkar, and A. A. Beenackers, "Photocatalytic degradation for environmental applications—a review," *Journal of Chemical Technology and Biotechnology*, vol. 77, no. 1, pp. 102–116, 2002.
- [2] M. Shang, W. Wang, L. Zhang, S. Sun, L. Wang, and L. Zhou, "3D $\text{Bi}_2\text{WO}_6/\text{TiO}_2$ hierarchical heterostructure: controllable synthesis and enhanced visible photocatalytic degradation performances," *Journal of Physical Chemistry C*, vol. 113, no. 33, pp. 14727–14731, 2009.
- [3] T. Saison, N. Chemin, C. Chaneéac et al., " Bi_2O_3 , BiVO_4 , and Bi_2WO_6 : impact of surface properties on photocatalytic activity under visible light," *Journal of Physical Chemistry C*, vol. 115, no. 13, pp. 5657–5666, 2011.
- [4] S. Anandan, G.-J. Lee, P.-K. Chen, C. Fan, and J. J. Wu, "Removal of Orange II dye in water by visible light assisted photocatalytic ozonation using Bi_2O_3 and $\text{Au}/\text{Bi}_2\text{O}_3$ nanorods," *Industrial and Engineering Chemistry Research*, vol. 49, no. 20, pp. 9729–9737, 2010.
- [5] M.-S. Gui, W.-D. Zhang, Q.-X. Su, and C.-H. Chen, "Preparation and visible light photocatalytic activity of $\text{Bi}_2\text{O}_3/\text{Bi}_2\text{WO}_6$ heterojunction photocatalysts," *Journal of Solid State Chemistry*, vol. 184, no. 8, pp. 1977–1982, 2011.
- [6] X. H. Wu, W. Qin, L. Li, Y. Guo, and Z. Y. Xie, "Photocatalytic property of nanostructured Fe^{3+} -doped Bi_2O_3 films," *Catalysis Communications*, vol. 10, no. 5, pp. 600–604, 2009.
- [7] J. K. Reddy, B. Srinivas, V. D. Kumari, and M. Subrahmanyam, " Sm^{3+} -doped Bi_2O_3 photocatalyst prepared by hydrothermal synthesis," *ChemCatChem*, vol. 1, no. 4, pp. 492–496, 2009.
- [8] A. Hameed, V. Gombac, T. Montini, L. Felisari, and P. Fornasiero, "Photocatalytic activity of zinc modified Bi_2O_3 ," *Chemical Physics Letters*, vol. 483, no. 4–6, pp. 254–261, 2009.
- [9] R. J. Tayade, R. G. Kulkarni, and R. V. Jasra, "Transition metal ion impregnated mesoporous TiO_2 for photocatalytic degradation of organic contaminants in water," *Industrial and Engineering Chemistry Research*, vol. 45, no. 15, pp. 5231–5238, 2006.
- [10] L. Yin, J. Niu, Z. Shen, and Y. Sun, "The electron structure and photocatalytic activity of Ti(IV) doped Bi_2O_3 ," *Science China Chemistry*, vol. 54, no. 1, pp. 180–185, 2011.
- [11] L. Yin, J. Niu, Z. Shen, and J. Chen, "Mechanism of reductive decomposition of pentachlorophenol by Ti-doped $\beta\text{-Bi}_2\text{O}_3$ under visible light irradiation," *Environmental Science and Technology*, vol. 44, no. 14, pp. 5581–5586, 2010.
- [12] L. Yin, Z. Shen, J. Niu, J. Chen, and Y. Duan, "Degradation of pentachlorophenol and 2,4-dichlorophenol by sequential visible-light driven photocatalysis and laccase catalysis," *Environmental Science and Technology*, vol. 44, no. 23, pp. 9117–9122, 2010.
- [13] U. I. Gaya and A. H. Abdullah, "Heterogeneous photocatalytic degradation of organic contaminants over titanium dioxide: a review of fundamentals, progress and problems," *Journal of Photochemistry and Photobiology C*, vol. 9, no. 1, pp. 1–12, 2008.
- [14] N. Sobana, M. Muruganadham, and M. Swaminathan, "Nano-Ag particles doped TiO_2 for efficient photodegradation of Direct azo dyes," *Journal of Molecular Catalysis A*, vol. 258, no. 1–2, pp. 124–132, 2006.
- [15] S. Sakthivel, M. V. Shankar, M. Palanichamy, B. Arabindoo, D. W. Bahnemann, and V. Murugesan, "Enhancement of photocatalytic activity by metal deposition: characterisation and photonic efficiency of Pt, Au and Pd deposited on TiO_2 catalyst," *Water Research*, vol. 38, no. 13, pp. 3001–3008, 2004.
- [16] S. S. Rayalu, D. Jose, M. V. Joshi, P. A. Mangrulkar, K. Shrestha, and K. Klabunde, "Photocatalytic water splitting on Au/TiO_2 nanocomposites synthesized through various routes: enhancement in photocatalytic activity due to SPR effect," *Applied Catalysis B*, vol. 142–143, pp. 684–693, 2013.
- [17] N. M. Sammes, G. A. Tompsett, H. Näfe, and F. Aldinger, "Bismuth based oxide electrolytes—structure and ionic conductivity," *Journal of the European Ceramic Society*, vol. 19, no. 10, pp. 1801–1826, 1999.
- [18] I. M. Arabatzis, T. Stergiopoulos, M. C. Bernard, D. Labou, S. G. Neophytides, and P. Falaras, "Silver-modified titanium dioxide thin films for efficient photodegradation of methyl orange," *Applied Catalysis B*, vol. 42, no. 2, pp. 187–201, 2003.
- [19] T. Sano, N. Negishi, D. Mas, and K. Takeuchi, "Photocatalytic Decomposition of N_2O on Highly Dispersed Ag+ Ions on TiO_2 Prepared by Photodeposition," *Journal of Catalysis*, vol. 194, no. 1, pp. 71–79, 2000.
- [20] L. Yin, Y. Wang, G. Pang, Y. Koltypin, and A. Gedanken, "Sonochemical synthesis of cerium oxide nanoparticles—effect

- of additives and quantum size effect,” *Journal of Colloid and Interface Science*, vol. 246, no. 1, pp. 78–84, 2002.
- [21] R. Si, Y.-W. Zhang, C.-X. Xiao et al., “Non-template hydrothermal route derived mesoporous $Ce_{0.2}Zr_{0.8}O_2$ nanosized powders with blue-shifted UV absorption and high CO conversion activity,” *Physical Chemistry Chemical Physics*, vol. 6, no. 5, pp. 1056–1063, 2004.
- [22] Y. Peng, J. Ji, X. Zhao, H. Wan, and D. Chen, “Preparation of ZnO nanopowder by a novel ultrasound assisted non-hydrolytic sol–gel process and its application in photocatalytic degradation of C.I. Acid Red 249,” *Powder Technology*, vol. 233, pp. 325–330, 2013.
- [23] S. K. Sharma, H. Bhunia, and P. K. Bajpai, “Photocatalytic decolorization kinetics and adsorption isotherms of a mixture of two anionic azo dyes: Reactive Red 120 and Reactive Black 5,” *Desalination and Water Treatment*, vol. 44, no. 1–3, pp. 261–268, 2012.
- [24] V. K. Gupta, R. Jain, S. Agarwal, A. Nayak, and M. Shrivastava, “Photodegradation of hazardous dye quinoline yellow catalyzed by TiO_2 ,” *Journal of Colloid and Interface Science*, vol. 366, no. 1, pp. 135–140, 2012.
- [25] A. Mills, R. H. Davies, and D. Worsley, “Water purification by semiconductor photocatalysis,” *Chemical Society Reviews*, vol. 22, no. 6, pp. 417–425, 1993.
- [26] S. Kohtani, J. Hiro, N. Yamamoto, A. Kudo, K. Tokumura, and R. Nakagaki, “Adsorptive and photocatalytic properties of Ag-loaded $BiVO_4$ on the degradation of 4-*n*-alkylphenols under visible light irradiation,” *Catalysis Communications*, vol. 6, no. 3, pp. 185–189, 2005.
- [27] S. Rengaraj and X. Z. Li, “Enhanced photocatalytic activity of TiO_2 by doping with Ag for degradation of 2,4,6-trichlorophenol in aqueous suspension,” *Journal of Molecular Catalysis A*, vol. 243, no. 1, pp. 60–67, 2006.
- [28] V. Vamathevan, R. Amal, D. Beydoun, G. Low, and S. McEvoy, “Photocatalytic oxidation of organics in water using pure and silver-modified titanium dioxide particles,” *Journal of Photochemistry and Photobiology A*, vol. 148, no. 1–3, pp. 233–245, 2002.

Research Article

Visible-Light-Driven Photocatalytic Degradation of Aniline over NaBiO₃

Guo Liu,^{1,2} Zhen Wang,^{2,3} Wenjie Zheng,² Shaogui Yang,¹ and Cheng Sun¹

¹ School of the Environment, Nanjing University, Nanjing 210093, China

² State Key Laboratory of Geohazard Prevention and Geoenvironment Protection, Chengdu University of Technology, Chengdu 610059, China

³ Faculty of Geosciences and Environmental Engineering, Southwest Jiaotong University, Chengdu 610059, China

Correspondence should be addressed to Shaogui Yang; yangdlut@126.com and Cheng Sun; envidean@nju.edu.cn

Received 6 December 2013; Accepted 1 January 2014; Published 13 February 2014

Academic Editor: Haimin Zhang

Copyright © 2014 Guo Liu et al. This is an open access article distributed under the Creative Commons Attribution License, which permits unrestricted use, distribution, and reproduction in any medium, provided the original work is properly cited.

Aniline was almost completely degraded in 30 min in given conditions. It was found that pH and NaBiO₃ dosage had played important role in the photocatalytic degradation. To scrutinize the mechanistic details of the aniline photodegradation, several critical analytical methods including spectroscopy and GC/MS were utilized to detect the temporal course of the reaction. Intermediates and several small molecular products were separated and identified, such as C₂H₅O₃N, C₁₀H₁₃O₂N, and C₁₂H₁₀N₂. Then two possible photodegradation pathways of aniline over NaBiO₃ were proposed: ring opening and mineralization.

1. Introduction

Aniline is widely used in the chemical industry, mainly as a raw material for obtaining isocyanate. Aniline is also applied to the manufacture of accelerators, antioxidants, pesticides, dyes, and pigments [1]. The negative effects of aniline on human health and the environment are depending on the amount and exposure time. Aniline can enter the aqueous environment via dyes and nitro aromatic compounds and has been identified as a potential carcinogen [2]. Nowadays, more attention is focused to remove it from environment.

Among chemical methods, photocatalysis technology can play an important role in removing harmful organic compounds, which enables human to have comfortable and safe lives [3]. Being the most common photocatalyst among semiconductors, TiO₂ possesses various merits such as low cost, high photocatalytic activity, chemical activity, and nontoxicity [4]. As its photoresponse is only limited in the UV region, which accounts for less than 5% of the earth-reaching solar irradiation [5, 6], it requires a high power UV excitation source [7]. Therefore, it is meaningful to explore a new photocatalyst which can utilize visible light.

Lots of studies have been devoted to developing visible-light-driven photocatalysis. Apart from TiO₂ doped with metallic elements, for instance, Cr³⁺ and V⁵⁺ [8], new materials such as AgNbO₃ and InNbO₄ are previously reported to absorb visible light [9, 10]. However, the activity of the photocatalyst was hardly enhanced, and the low reaction rate severely blocked the development of photocatalysis technology.

Seeking for new materials with higher photocatalytic activity has become a key solution to this problem. Particularly, Bi(V)-containing oxides are potential materials as the candidates of visible light sensitive oxides [11]. In fact, some Bi(V)-containing oxides have indicated the ability of absorption of visible light. Among them, NaBiO₃ is studied as it displayed the visible light absorption because of its hybridized valence band. The large dispersion of the hybridized orbitals in the conduction band increases the mobility of the photoexcited electrons, thus suppressing the recombination of photoexcited electron-hole pairs and enhancing activities [11]. Kou and coworkers [12] utilized NaBiO₃ in photooxidation of PAHS. Yu and coworkers [13] utilized NaBiO₃ in photooxidation of rhodamine B under visible light irradiation and found that heating temperature

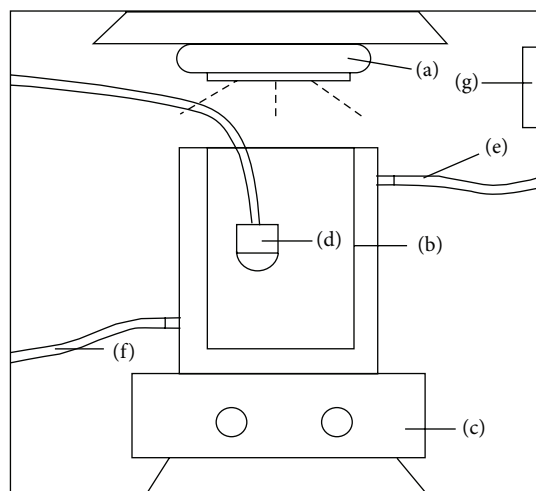


FIGURE 1: Photoreaction chamber. (a) Xenon lamp, (b) double-deck beaker, (c) magnetic stirrer, (d) oxygen pump, (e) outlet, (f) inlet, and (g) fan.

significantly influenced the photocatalytic activity of the catalyst. As NaBiO_3 has the properties of strong oxidation, electromagnetism, and electrochemical activity, it has been applied to industries such as organic synthesis, superconductor, and electrochemistry [14]. It is meaningful to explore the feasibility of the photodegradation of aniline over NaBiO_3 .

In this study, aniline was chosen as the target organic pollutant to investigate its degradation behavior over NaBiO_3 under visible light irradiation. The goal was aimed at the investigation of aniline degradation and the presentation of mechanistic details of the photochemical process.

2. Experimental Section

2.1. Materials and Reagents. Aniline was bought from Ke Long Chemical Company, and $\text{NaBiO}_3 \cdot 2\text{H}_2\text{O}$ (NBH) was purchased from Guang Fu Chemical Products Institute. All other chemicals were of analytical grade and used without further purification.

2.2. Photoreaction Chamber. Photodegradation experiments were performed in a chamber which was displayed in Figure 1. A 500 W xenon lamp (Chengdu Na Pu Photoelectricity Company, China) was positioned to ensure visible light. The reactor was a double-deck beaker equipped with an inlet and an outlet which can draw into water circulation to make sure experiments performed in adequate temperature. A 50 W fan was used to keep the chamber at ambient temperature. A stir was used to ensure that photocatalyst distributes well in the suspension. Oxygen pump was used to provide enough oxygen to ensure that oxidation performed sufficiently.

2.3. Experimental Procedures and Analysis Methods. In the experiments, the dispersions containing aniline and NaBiO_3 photocatalyst were prepared by adding NBH to an aqueous solution of aniline in a beaker.

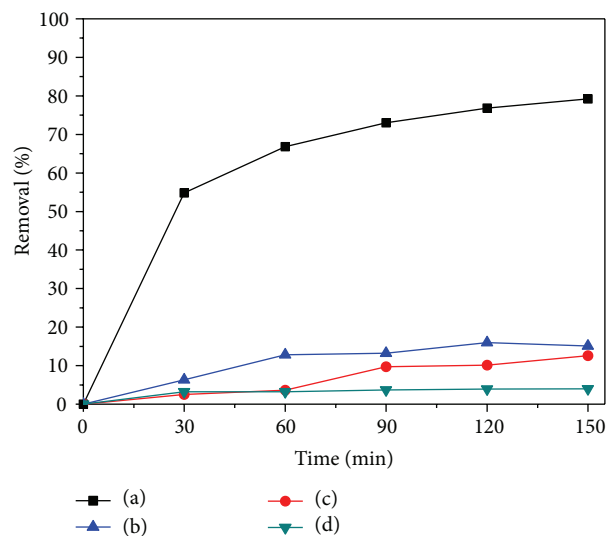


FIGURE 2: Control experiment. (a) Light+ NBH, (b) NBH alone, (c) light alone, and (d) none.

A 500 mL double-deck beaker was used as a reactor. The NBH was added to 200 mL aniline solution, which was magnetically stirred at a constant speed to ensure continuous contact between the solution and NaBiO_3 when they were under visible light irradiation emitted from xenon lamp. At given time intervals, samples (10 mL) were centrifuged immediately. The samples were analyzed by a V-1100D spectrophotometer. The intermediates were detected by GC/MS (GCMS-QP2010 Plus).

3. Results and Discussions

3.1. Control Experiment. The decreases of aniline concentration as a function of reaction time were shown in Figure 2. In the control experiment, when utilizing NBH (1 g/L) alone, a slight decrease of aniline concentration was observed; this could be attributed to surface adsorption. Aniline was relatively stable in aqueous solution under visible light irradiation as expected. Therefore, aniline was not significantly decomposed by either under ambient conditions used in the experiment. Aniline can be degraded rapidly only in the circumstance of both NBH and visible light irradiation.

3.2. Nitrogen Transformation. As there is an amidogen in the aniline structure, it will be harmful to environment if it transforms into nitrite nitrogen. It is important to study the transformation of nitrogen in the photodegradation process of aniline.

As it was shown in Figure 3, the removal rose in the first 30 min of the degradation aniline; the concentration of ammonia nitrogen and nitrate were increasing and tended towards stability in 120 min. Nitrites were produced as the intermediates of nitrate, and the concentration was low on the whole.

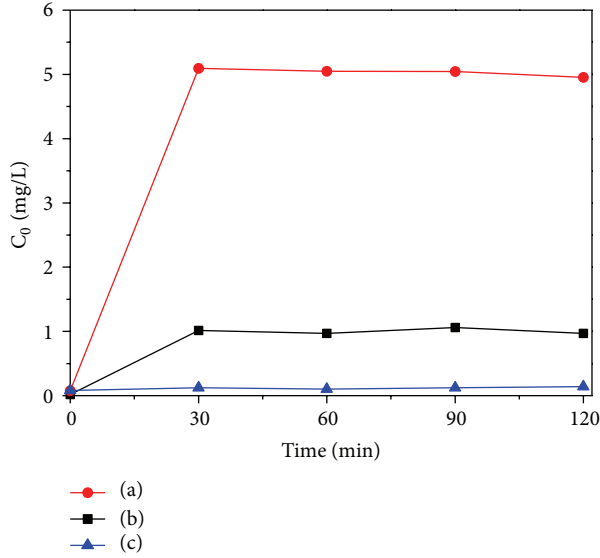


FIGURE 3: Temporal change in the concentration of nitrogen during the photodegradation. (a) Nitrate, (b) ammonia nitrogen, and (c) nitrite.

3.3. Kinetic Model. The reaction mechanism of photocatalytic degradation was the process of absorption-surface-reaction-desorption whose kinetic model was in coincidence with the Langmuir-Hinshelwood model [15, 16]. The kinetic model was as below [17]:

$$-\frac{dc}{dt} = Kc, \quad (1)$$

where t is time and c is instantaneous concentration of aniline. The equation below is the integration of it when t is from 0 to t :

$$\ln c = -Kt + \ln c_0. \quad (2)$$

When initial aniline concentration was 30 mg/L, the pseudo first order rate constant for photocatalytic degradation, light reaction, and dark reaction was 0.0402 min^{-1} , 0.00182 min^{-1} , and $0.000987 \text{ min}^{-1}$, respectively. The kinetic study proved that the effect of NBH on aniline degradation is great.

3.4. Influence Factors

3.4.1. pH Value Effect. In the photocatalytic oxidation, the solution pH had an instant influence on the agglomeration of particles, electric charge, and absorption of organic on the surface [18]. In Figure 4, the remainder aniline in the acidity was less than that in the neutral and alkaline condition. When pH was 2, the aniline concentration was reduced to 0.98 mg/L in the 120 min with a removal of 97%. The main reason was that the oxidation was in the dominant position. It was found that the NBH effect was better in the acidity condition. The removal rate can reach 75% in the 5 minutes, whereas the removal rate in the neutral and alkaline condition was 20% and 16%, respectively. In the acidity condition, $[\text{BiO}_3]$

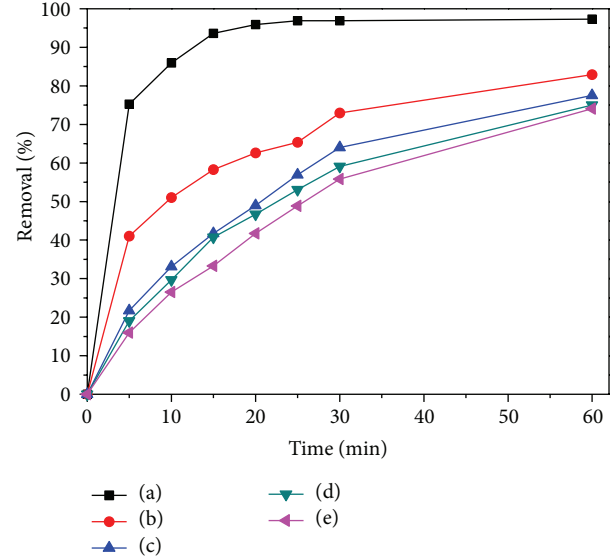
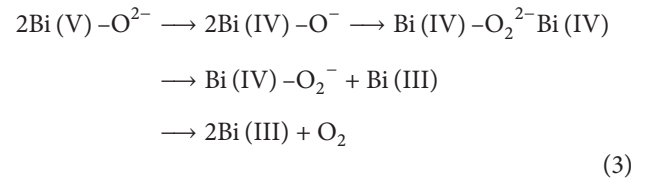


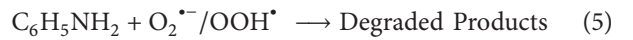
FIGURE 4: Effect of initial pH value. (a) pH = 2, (b) pH = 4, (c) pH = 8, (d) pH = 6, and (e) pH = 10.

can turn into $[\text{BiO}_6]$ more easily, while the latter's crystal structure was relatively weak. During reduction of Bi(V), oxygen which had higher activity was released [13]. The equation was as below:



In this case, aniline was oxidized mainly by O_2^{\bullet} . The reaction progress was not part of photocatalytic oxidation.

The photocatalytic oxidation of aniline was as below:



H^+ has played an important role in the photocatalytic oxidation. In the weak acidity condition, H^+ can combine with active oxygen to produce more OH^{\bullet} which increases the reaction rate. In the neutral and alkaline condition, the oxidation electric potential decreased as the pH increases. As a result, the removal had a decline [19].

3.4.2. NBH Dosage Effect. The result of aniline degradation over NBH dosage was given in Figure 5. The result showed that the oxidation efficiency was increasing with NBH dosage increasing correspondingly in the first 30 min. When NBH dosage was 0.5 g, there was a significant rise in the removal, as the aniline concentration was decreased to 12.7 mg/L in the 10 min. However, the removal in the 120 min was 84%, lower when compared with 0.2 g and 0.1 g, which were both around 87%. Referring to the fact that over NBH dosage could hinder the suspension transparency, which would be an obstacle

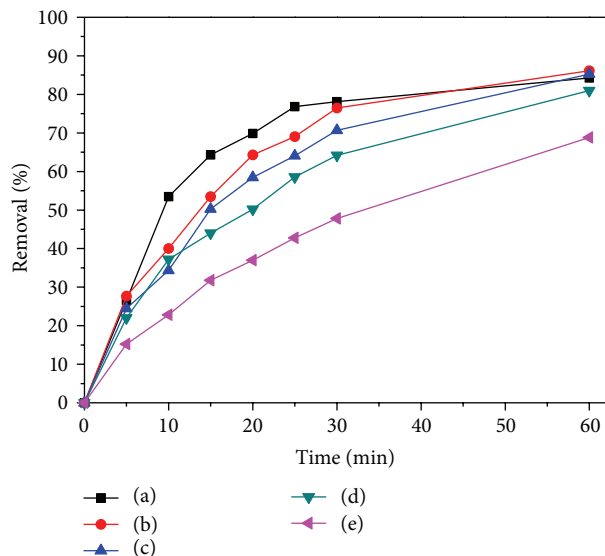


FIGURE 5: Effect amount of NBH. (a) 0.5 g, (b) 0.2 g, (c) 0.1 g, (d) 0.05 g, and (e) 0.025 g.

to absorb light and decrease photocatalytic degradation efficiency eventually, as a result, excessive NBH dosage could lead to a downward trend shown in the oxidation effect.

3.4.3. GC/MS Analysis. In the given condition, aniline could be degraded completely in the 30 min. Analysis on the intermediates and final products can help to clarify the details of the reaction. They were identified by GC/MS (GCMS-QP2010 Plus) and shown in Table 1 and Figure 6.

In the chromatograph of initial sample, there was a peak representing aniline, which disappeared in the 30 min. The chromatogram of 60 min resembled that of 30 min, as the peak of $C_{10}H_{13}O_2N$ and azobenzene existed, while their top area was decreasing. It proved that the above intermediates of aniline have been degraded to other products. There was a peak at about 7 min in the picture of 60 min, which was $C_2H_5O_3N$, the product of $C_{10}H_{13}O_2N$ and azobenzene. In the chromatogram of 90 min, $C_2H_5O_3N$ was not detected, which meant it had been mineralized into CO_2 . The peak of $C_{10}H_{13}O_2N$ had disappeared in the chromatogram of 120 min. The organics containing nitrogen only was azobenzene, and its peak area had decreased to a small part.

The photocatalytic reaction, generated by $NaBiO_3$ under visible light, could make reaction with aniline and produce azobenzene. Azobenzene produces $C_{10}H_{13}O_2N$ by $\cdot OH$ and h^+ . As the reaction goes on, azobenzene could still react with $\cdot OH$ or h^+ until its loop opens. $C_{10}H_{13}O_2N$ would go into two parts by the effect of $\cdot OH$ and h^+ . One could produce $C_2H_5O_3N$ and then be mineralized, while the other one is mineralized after ring opening.

4. Conclusion

Aniline could be easily degraded by $NaBiO_3$ under visible light irradiation. In the experiment, aniline was decomposed

TABLE 1: Identification of the small molecular intermediates of aniline during the photoreaction by GC/MS.

Product	Rt (min)	Mw	Formula	Name
1	7	91	$C_2H_5NO_3$	2-Nitroethanol
2	18	179	$C_{10}H_{13}NO_2$	3-Hydroxy-N-phenylbutanamide
3	18.5	93	C_6H_7N	Aniline
4	21	182	$C_{12}H_{10}N_2$	Azobenzene

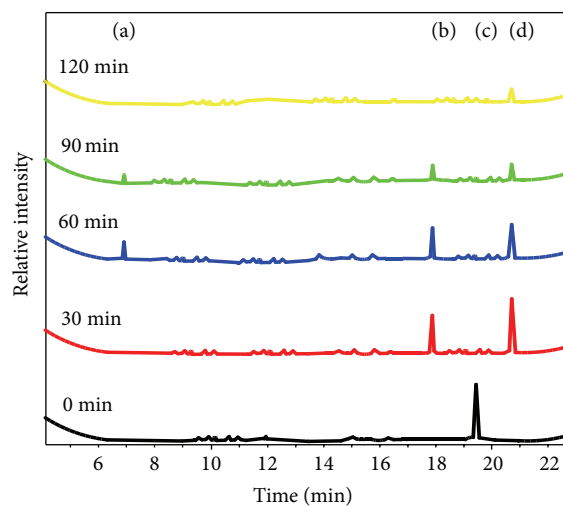


FIGURE 6: GC chromatograph of intermediates. (a) $C_2H_5O_3N$, (b) $C_{10}H_{13}O_2N$, (c) C_6H_7N , and (d) $C_{12}H_{10}N_2$.

largely under visible light over $NaBiO_3$ in 120 min, which could reach 95% in some conditions. Moreover, three small molecular products were also identified by GC/MS. On the basis of the data collected, the mechanism of aniline photodegradation on $NaBiO_3$ had been elucidated. Aniline could react with $\cdot OH$ or h^+ . Its products would go into two parts. One part would be mineralized directly, while the other part opened ring and produced $C_2H_5O_3N$ then was mineralized; meanwhile, N-ionogen turned into mineral nitrogen.

Conflict of Interests

The authors declare that there is no conflict of interests regarding the publication of this paper.

Acknowledgments

This research was supported by the National Natural Science Foundation of China (41272266), Natural Science Foundation of Jiangsu Province (BK2012732), and the Natural Science Key Program for Si Chuan Province Education Department of China (10ZA113).

References

- [1] M. Mitadera, N. Spataru, and A. Fujishima, "Electrochemical oxidation of aniline at boron-doped diamond electrodes," *Journal of Applied Electrochemistry*, vol. 34, no. 3, pp. 249–254, 2004.
- [2] M. Fukushima, K. Tatsumi, and K. T. Morimoto, "The fate of aniline after a photo-fenton reaction in an aqueous system containing iron(III), humic acid, and hydrogen peroxide," *Environmental Science & Technology*, vol. 34, no. 10, pp. 2006–2013, 2000.
- [3] T. Kako and J. Ye, "Photocatalytic decomposition of acetaldehyde over rubidium bismuth niobates under visible light irradiation," *Materials Transactions*, vol. 46, no. 12, pp. 2694–2698, 2005.
- [4] V. Mirkhani, S. Tangestaninejad, M. Moghadam, M. H. Habibi, and A. Rostami Vartooni, "Photodegradation of aromatic amines by Ag-TiO₂ photocatalyst," *Journal of the Iranian Chemical Society*, vol. 6, no. 4, pp. 800–807, 2009.
- [5] D. Chatterjee and S. Dasgupta, "Visible light induced photocatalytic degradation of organic pollutants," *Journal of Photochemistry and Photobiology C*, vol. 6, no. 2-3, pp. 186–205, 2005.
- [6] D. Zhao, C. Chen, Y. Wang et al., "Enhanced photocatalytic degradation of dye pollutants under visible irradiation on Al(III)-modified TiO₂: structure, interaction, and interfacial electron transfer," *Environmental Science & Technology*, vol. 42, no. 1, pp. 308–314, 2008.
- [7] E. Borgarello, J. Kiwi, M. Gratzel et al., "Visible light induced water cleavage in colloidal solutions of chromium-doped titanium dioxide particles," *Journal of the American Chemical Society*, vol. 104, no. 11, pp. 2996–3002, 1982.
- [8] N. Serpone, D. Lawless, J. Disdier, and J.-M. Herrmann, "Spectroscopic, photoconductivity, and photocatalytic studies of TiO₂ colloids: Naked and with the lattice doped with Cr³⁺, Fe³⁺, and V⁵⁺ cations," *Langmuir*, vol. 10, no. 3, pp. 643–652, 1994.
- [9] H. Kato, H. Kobayashi, and A. Kudo, "Role of Ag⁺ in the band structures and photocatalytic properties of AgMO₃ (M: Ta and Nb) with the perovskite structure," *Journal of Physical Chemistry B*, vol. 106, no. 48, pp. 12441–12447, 2002.
- [10] Z. Zou, J. Ye, and H. Arakawa, "Structural properties of InNbO₄ and InTaO₄: correlation with photocatalytic and photophysical properties," *Chemical Physics Letters*, vol. 332, no. 3-4, pp. 271–277, 2000.
- [11] Z. Li, N. Xu, Y. Chen, and Z. Zou, "Photocatalytic behavior of a new series of photocatalysts, Ba₂Bi^(V)Bi^(III)O₆ and Ba₂Sb^(V)Bi^(III)O₆," *Research on Chemical Intermediates*, vol. 31, no. 4–6, pp. 529–534, 2005.
- [12] J. Kou, H. Zhang, Z. Li, S. Ouyang, J. Ye, and Z. Zou, "Photooxidation of polycyclic aromatic hydrocarbons over NaBiO₃ under visible light irradiation," *Catalysis Letters*, vol. 122, no. 1-2, pp. 131–137, 2008.
- [13] K. Yu, S. Yang, S. A. Boyd, H. Chen, and C. Sun, "Efficient degradation of organic dyes by BiAgxOy," *Journal of Hazardous Materials*, vol. 197, pp. 88–96, 2011.
- [14] J.-Q. Pan, P.-Y. Wan, Y.-Z. Sun, Z.-H. Wang, and X.-G. Liu, "Synthesis and structural characterization of nano-NaBiO₃," *Gaodeng Xuexiao Huaxue Xuebao/Chemical Journal of Chinese Universities*, vol. 25, no. 12, p. 2204, 2004.
- [15] T. Hiroaki, A. Manabu, K. Yasuyuki, and I. Seishiro, "Enhancing effect of SiO_x monolayer coverage of TiO₂ on the photoinduced oxidation of rhodamine 6G in aqueous media," *The Journal of Physical Chemistry B*, vol. 102, no. 33, pp. 6360–6366, 1998.
- [16] D. D. Dionysiou, A. P. Khodadoust, A. M. Kern et al., "Continuous-mode photocatalytic degradation of chlorinated phenols and pesticides in water using a bench-scale TiO₂ rotating disk reactor," *Applied Catalysis B*, vol. 24, no. 3-4, pp. 139–155, 2000.
- [17] I. K. Konstantinou, T. M. Sakellarides, V. A. Sakkas et al., "Photocatalytic Degradation of Selected s-Triazine Herbicides and Organophosphorus Insecticides over Aqueous TiO₂ Suspensions," *Environmental Science and Technology*, vol. 35, no. 2, pp. 398–405, 2001.
- [18] H. Wu, M. Wu, M. Xie et al., "The enhanced electro-assisted photocatalytic degradation of organic water contaminants," *Chinese Journal of Catalysis*, vol. 21, no. 5, pp. 399–403, 2000.
- [19] P. K. Malik, "Oxidation of safranin T in aqueous solution using Fenton's reagent: involvement of an Fe(III) chelate in the catalytic hydrogen peroxide oxidation of safranin T," *The Journal of Physical Chemistry A*, vol. 108, no. 14, pp. 2675–2681, 2004.